

Vortex-Induced Vibration of Circular Cylinders Using Multi-Block Immersed Boundary-Lattice Boltzmann Method

Han Jiao

A thesis submitted for the degree of

Doctor of Philosophy

Department of Mechanical Engineering

University College London

June 2021

I, Han Jiao, confirm that the work presented in this thesis is my own under the supervision of Professor Guoxiong Wu. Where information has been derived from other sources, I confirm that this has been indicated in the thesis.

Abstract

Despite decades of research, vortex-induced vibration (VIV) of circular cylinders is still a topic of strong interest in fluid mechanics, as it is of great importance in many engineering disciplines, such as bridges, nuclear reactors and high-rise buildings. In order to provide an in-depth understanding of complex fluid-structure interaction during VIV, this thesis considers the following physical scenarios using an in-house code developed based on immersed boundary-lattice Boltzmann method (IB-LBM). First, a system with two fixed cylinders with an intermediate centre-to-centre spacing is considered. It is found that the frequency component of the force on each individual cylinder changes from a single value to multiple ones, then to a large number of discrete ones and eventually to a broadband continuous spectrum, as the alignment angle increases. Second, the vibration of a cylinder may occur due to fluid-structure interaction, and thus the free motion is investigated using the results from the corresponding forced oscillation. It is shown that when a cylinder is in periodic free motion, its motion will remain the same if the combined mass-damping parameter remains unchanged and the variations of body mass and stiffness follow a particular pattern. Here, the damping ratio is redefined using the motion frequency of the body instead of the commonly adopted natural frequency of the body. Third, large-eddy simulation as turbulence model is implemented in the computer code and multi grids are adopted in IB-LBM to improve computation efficiency and accuracy. Turbulent flow is then studied. The results show that the effect of the Reynolds number on the well-known three response branches at different reduced velocities, or initial, upper and lower branches, is significant. When Reynolds number is fixed, at its lower range calculated, there are only initial and upper branches, and at higher range, there are only upper and lower branches.

Impact statements

This thesis has contributed to a better understanding of the physical mechanism behind vortex-induced vibration. It is of physical and engineering interest, because VIV may lead to the extensive oscillation of structures and the long-term cyclic loads on structures. The present research focuses on two aspects of VIV using lattice Boltzmann method coupled with immersed boundary method and aims to provide practical solutions to help engineering design.

On the one hand, a system with multiple bluff bodies is common in practical applications. The complex interaction between the wake and body always make the flow physics significantly different from that past a single bluff body. The interaction between the wakes from multiple bluff bodies have serious effects on the safety of the system, such as the adverse loads induced on the nearby bodies and the severe oscillatory motion of the downstream body due to the vortex shed from the upstream body. The flow past two identical circular cylinders is one of prototypical configurations. Thus, the fluctuating force acting on two stationary cylinders in tandem, staggered and side-by-side arrangements is considered systematically.

On the other hand, in real engineering problems, such as tension leg platforms for offshore wind turbines and offshore production of oil and gas, the tensioned cables are often so long that their free motions are easy to be excited due to the fluid-structure interaction, which leads to cyclic loads first and then may result in fatigue damage of the system. Thus, the motion characters of a free cylinder are investigated. An approach to predicting the free motion of a cylinder in a fluid stream is to use the results from the corresponding forced oscillation. In this thesis, the equivalence between transverse free and forced motions is provided based on the mathematical analysis and verified through the numerical results. In such as case, when the structural damping is fixed, if the cylinder mass and stiffness vary together following a particular relationship, the free motion will remain the same. Also, the free vibration of a cylinder in the turbulent flow is studied based on a refined numerical

method. Large-eddy simulation is chosen as the turbulence model and multi-block model is adopted to improve the accuracy and the computational efficiency.

Nomenclature

b, b^*	structural damping (* refers to the non-dimensional one)
c	lattice speed
c_s	artificial sound speed
C	Smagorinsky constant
C_D	drag coefficient
$\overline{C_D}$	mean drag coefficient
C_L	lift coefficient
C_{Lrms}	root-mean-square lift coefficient
C_{L0}	amplitude of lift coefficient
d	number of spatial dimensions
D	cylinder diameter
\mathbf{e}_i	particle velocity
E	internal energy
E_{fc}, E_{fc}^*	energy transfer from the flow to the cylinder over a period
f	particle density distribution function
f^{eq}	equilibrium distribution function
f^*	ratio between body motion frequency and its natural frequency
f_c, f_c^*	motion frequency
f_n, f_n^*	natural frequency of a cylinder
f_v	frequency of lift coefficient for a fixed cylinder
F_D	drag force
F_L	lift force
F_{L0}	maximum value of lift force
\mathbf{g}	body force on the fluid
\mathbf{G}	body force on the boundary
k, k^*	structural stiffness
k_B	Boltzmann constant

\tilde{k}^*	related stiffness
\mathbf{K}	particular velocity
l, δ_x, δ_y	lattice spacing
L, L^*	centre-to-centre spacing in a two-cylinder system
Le, Ls, Lr	length of computational domain
m, m^*	body mass
m_{cf}	ratio of the space steps between coarser and finer blocks
M	molecular mass
M_a	Mach number
M_e^*	effective added mass
M_p, M_p^*	potential flow added mass
p	fluid pressure
\bar{p}	filtered fluid pressure
$Q_{\alpha\beta}$	momentum flux tensor
R	gas constant
Re	Reynolds number
s	grid parameter
\mathbf{S}	strain rate tensor
St	Strouhal number for a fixed cylinder
t	time
T	nondimensional time
\mathbf{T}	Reynolds stress tensor
T_c	period of cylinder oscillation
T_v	period of lift coefficient for a fixed cylinder
\mathbf{u}	fluid velocity
\mathbf{u}^d	desired fluid velocity
$\bar{\mathbf{u}}$	filtered fluid velocity
u_0	incoming free-stream velocity
U^*	reduced velocity

U^*	desired velocity on the boundary
U^d	velocity of the body surface
U_{IU}^*, U_{UL}^*	critical value of reduced velocity
Y_0, Y_0^*	motion amplitude
Y_{0max}, Y_{0max}^*	peak amplitude
\dot{Y}	oscillation velocity of a cylinder
α	alignment angle between the line linking two cylinder centres and flow direction
Δ	filter width
δ_l	delta function
δ_t	time step
δ_s	arc length of the boundary element
$\delta_{\alpha\beta}$	Kronecher delta function
ζ	structural damping ratio
ζ_c	redefined damping ratio
λ^*	wavelength
ν	kinetic viscosity
ν_e	eddy viscosity
ν_T	total viscosity including kinetic and eddy viscosity
ρ	fluid density
ξ	particle velocity
τ_0, τ	relaxation time/ nondimensionalized relaxation time
\mathcal{T}	temperature
ϕ	phase angle between lift coefficient and cylinder motion
ω_c	motion angular frequency of a body
ω_i	weighting coefficient
ω_n	natural angular frequency of a body with the added mass effect
Ω	collision operator
Ω_{BGK}	BGK collision operator

Contents

Abstract	3
Impact Statements	5
Nomenclature	7
1. Introduction	19
1.1 Engineering Background.....	19
1.2 Literature Review	21
1.2.1 Flow past two stationary cylinders in different arrangements.....	21
1.2.2 Relationship between transverse-only forced and free vibration.....	27
1.2.3 Effect of Reynolds number on VIV amplitude branches.....	32
1.3 Research Equations, Objectives and Contributions.....	35
1.4 List of Publications.....	37
1.5 Thesis Layout.....	38
2. Lattice Boltzmann Method	39
2.1 Lattice Boltzmann equation.....	39
2.2 Recovery of Navier-Stokes equations from lattice Boltzmann equation.....	46
2.3 Immersed boundary method.....	49
2.4 Turbulence model.....	53
2.5 Multi-block method in lattice Boltzmann method.....	55
3. Flow past two cylinders in different arrangements	60
3.1 Convergence and comparison.....	60
3.2 The flow past two stationary cylinders in various arrangements.....	62
3.2.1 two tandem cylinders.....	64
3.2.2 two staggered cylinders with $\alpha = 15^\circ$	66
3.2.3 two staggered cylinders with $\alpha = 30^\circ$	69

3.2.4 two staggered cylinders with $\alpha = 45^\circ$	71
3.2.5 two staggered cylinders with $\alpha = 46^\circ$	74
3.2.6 two staggered cylinders with $\alpha = 60^\circ$	76
3.2.7 two side-by-side cylinders.....	78
3.3 Summary.....	80
4. Free vibration predicted using forced oscillation in the lock-in region.....	82
4.1 Equivalence between free motion and force motion at lock-in.....	82
4.2 Convergence and comparison.....	84
4.3 Simulations of forced motion at lock-in.....	86
4.4 Prediction and simulation of free motion of a body.....	90
4.5 Predicting the free motion from the $b^* - \tilde{k}^*$ diagram of the forced motion.....	93
4.6 Summary.....	101
5. Effect of Reynolds number on VIV amplitude branches with turbulence model.....	103
5.1 Free motion of a body.....	103
5.2 Verification through comparison.....	104
5.3 Variation of body motion with reduced velocities at different fixed Reynolds number.....	108
5.4 Body motion at U_{IU}^* and U_{UL}^* shown in Fig. 5-2.....	113
5.5 Summary.....	116
6. Conclusion and future work.....	118
6.1 Conclusions from the finished studies.....	118
6.2 Suggestions for the future work.....	121
Acknowledgements.....	124
Bibliography.....	126

Abstract.....	3
Impact Statements.....	5
Nomenclature.....	7
1. Introduction.....	19
1.1 Engineering Background.....	19
1.2 Literature Review	21
1.2.1 Flow past two stationary cylinders in different arrangements.....	21
1.2.2 Relationship between transverse-only forced and free vibration.....	27
1.2.3 Effect of Reynolds number on VIV amplitude branches.....	32
1.3 Research Equations, Objectives and Contributions.....	35
1.4 List of Publications.....	37
1.5 Thesis Layout.....	38
2. Lattice Boltzmann Method.....	39
2.1 Lattice Boltzmann equation.....	39
2.2 Recovery of Navier-Stokes equations from lattice Boltzmann equation.....	46
2.3 Immersed boundary method.....	49
2.4 Turbulence model.....	53
2.5 Multi-block method in lattice Boltzmann method.....	55
3. Flow past two cylinders in different arrangements.....	60
3.1 Convergence and comparison.....	60
3.2 The flow past two stationary cylinders in various arrangements.....	62
3.2.1 two tandem cylinders.....	64
3.2.2 two staggered cylinders with $\alpha = 15^\circ$	66
3.2.3 two staggered cylinders with $\alpha = 30^\circ$	69
3.2.4 two staggered cylinders with $\alpha = 45^\circ$	71
3.2.5 two staggered cylinders with $\alpha = 46^\circ$	74
3.2.6 two staggered cylinders with $\alpha = 60^\circ$	76

3.2.7 two side-by-side cylinders.....	78
3.3 Summary.....	80
4. Free vibration predicted using forced oscillation in the lock-in region.....	82
4.1 Equivalence between free motion and force motion at lock-in.....	82
4.2 Convergence and comparison.....	84
4.3 Simulations of forced motion at lock-in.....	86
4.4 Prediction and simulation of free motion of a body.....	90
4.5 Predicting the free motion from the $b^* - \tilde{k}^*$ diagram of the forced motion.....	93
4.6 Summary.....	101
5. Effect of Reynolds number on VIV amplitude branches with turbulence model.....	103
5.1 Free motion of a body.....	103
5.2 Verification through comparison.....	104
5.3 Variation of body motion with reduced velocities at different fixed Reynolds number.....	108
5.4 Body motion at U_{IU}^* and U_{UL}^* shown in Fig. 5-2.....	113
5.5 Summary.....	116
6. Conclusion and future work.....	118
6.1 Conclusions from the finished studies.....	118
6.2 Suggestions for the future work.....	121
Acknowledgements.....	124
Bibliography.....	126

List of Figures

1-1	Arrangements of two cylinders: (a) tandem; (b) side-by-side and (c) staggered arrangements.....	21
1-2	Instantaneous vorticity contours with $\alpha = 0^\circ$ according to the wake pattern: (a) extended-body pattern; (b) reattachment pattern; (c) bi-stable pattern; (d) co-shedding pattern.....	23
1-3	Instantaneous vorticity contours with $\alpha = 90^\circ$ according to the wake pattern: (a) single bluff-body pattern; (b) deflected pattern; (c) flip-flopping pattern; (d) antiphase-synchronized pattern; (f) in-phase-synchronized pattern.....	25
1-4	Instantaneous vorticity contours with $0^\circ < \alpha < 90^\circ$ according to the wake pattern: (a) single bluff-body pattern with smaller (left) and larger (right) alignment angle; (b) reattachment pattern with smaller alignment angle; (c) co-shedding pattern with smaller alignment angle; (d) co-shedding pattern with larger alignment angle.....	27
1-5	The type of the motion amplitude curve of a low mass cylinder against reduced velocity (or Reynolds number).....	34
2-1	$DdQq$ models: (a) $D1Q3$; (b) $D2Q9$; (c) $D3Q19$. Velocities with length $ e_i = c, \sqrt{2}c$ in blue and other colours, respectively.....	44
2-2	Lattice and discrete velocities of the $D2Q9$ model.....	45
2-3	Immersed boundary illustration.....	50
2-4	Two blocks of different lattice spacing near their interface.....	56
2-5	Sketch for three-point Lagrangian interpolation.....	58
3-1	Computational configurations for (a) a single cylinder and (b) two cylinders.....	60
3-2	Vortex contour for a single cylinder at $T = 185.7$ with $Re = 200$	62
3-3	Drag and lift coefficients on a single cylinder at $Re = 200$	62
3-4	Power spectra of (a) the lift and (b) drag coefficients on a single cylinder with $Re = 200$	62
3-5	Mean drag and lift coefficients as functions of α	64
3-6	Force coefficient time histories on two cylinders with $\alpha = 0^\circ$	65

3-7	Spectra of force coefficients for (a)-(b) downstream cylinder; (c)-(d) upstream cylinder with $\alpha = 0^\circ$	66
3-8	Vortex contour at $T = 273$ with $\alpha = 0^\circ$	66
3-9	Force coefficient time histories on two cylinders with $\alpha = 15^\circ$	68
3-10	Spectra of force coefficient for (a)-(b) upper cylinder and (c)-(d) lower cylinder with $\alpha = 15^\circ$	68
3-11	Vortex contour at $T = 273$ with $\alpha = 15^\circ$	69
3-12	Force coefficient time histories on two cylinders with $\alpha = 30^\circ$	70
3-13	Spectra of force coefficients for (a)-(b) upper cylinder and (c)-(d) lower cylinder with $\alpha = 30^\circ$	70
3-14	Vortex contour at $T = 273$ with $\alpha = 30^\circ$	71
3-15	Force coefficient time histories on two cylinders with $\alpha = 45^\circ$	72
3-16	Spectra of force coefficients for (a)-(b) upper cylinder and (c)-(d) lower cylinder with $\alpha = 45^\circ$	73
3-17	Y-direction velocity of four points (left) and their spectra (right) with $\alpha = 45^\circ$ (Indexes 1-4 represent points at $(7.5D, 12.0D)$, $(7.0D, 10.2D)$, $(6.2D, 9.8D)$ and $(6.2D, 9.3D)$, respectively.).....	74
3-18	Vortex contour at $T = 217$ with $\alpha = 45^\circ$	74
3-19	Force coefficient time histories on two cylinders with $\alpha = 46^\circ$	75
3-20	Spectra of force coefficients for (a)-(b) upper cylinder and (c)-(d) lower cylinder with $\alpha = 46^\circ$	76
3-21	Vortex contour at $T = 637$ with $\alpha = 46^\circ$	76
3-22	Force coefficient time histories on two cylinders with $\alpha = 60^\circ$	77
3-23	Spectra of force coefficients for (a)-(b) upper cylinder and (c)-(d) lower cylinder with $\alpha = 60^\circ$	78
3-24	Vortex contour with $\alpha = 60^\circ$: (a) at $T = 1309$; (b) at $T = 1344$	78
3-25	Force coefficient time histories on two cylinders with $\alpha = 90^\circ$	79
3-26	Spectra of force coefficients for (a)-(b) upper cylinder and (c)-(d) lower cylinder with $\alpha = 90^\circ$	80
3-27	Vortex contour with $\alpha = 90^\circ$ at (a) $T = 693$ and (b) $T = 721$	80

4-1	Comparison of motion amplitude against k^* for free vibration at $m^* = 2$, $b^* = 0$, and $Re = 150$ ($s = 70$; $M = 0.02$).....	87
4-2	Results of lock-in forced oscillation with different amplitudes at $f_c^* = 0.2$	88
4-3	Results of lock-in forced oscillation with different amplitudes at $f_c^* = f_v^* = 0.177$...	89
4-4	Results of lock-in forced oscillation with different amplitudes at $f_c^* = 0.15$	90
4-5	$b^* - \tilde{k}^*$ diagram at various f_c^* and Y_0^* (solid lines denote values of $f_c^* = 0.14 - 0.2$ and dashed-dotted lines $Y_0^* = 0.050 - 0.55$ with 0.025 increment).....	95
4-6	Amplitude and frequency of free motion against k^* in the lock-in region predicted from the forced motion results with $m^* = 10$	97
4-7	Vortex contour at the maximum value of lift coefficient for (a) the point (I) and (b) the point (II) shown in Fig. 4-6.....	98
4-8	The ratio between body motion frequency and its natural frequency as well as the motion amplitude in the lock-in region predicted from the forced motion results with $b^* = 0.5$	98
4-9	Lift coefficient and displacement as well as their amplitude spectra from the free motion simulations at $m^* = 10$, $b^* = 0$ and $k^* = 26$	100
4-10	Lift coefficient and displacement as well as their amplitude spectra from the free motion simulations at $m^* = 10$, $b^* = 0$ and $k^* = 5$	101
5-1	(a) Computational configuration and (b) schematic diagram of grid levels.....	105
5-2	Comparison of motion amplitude and frequency ratio between experimental data from Govardhan and Williamson (2000) and present results.....	107
5-3	Displacement and lift coefficient near critical reduced velocity between initial and upper branches ((a) corresponding point (I) and (b) corresponding point (II) shown in Fig. 5-2), and near that between upper and lower branches ((c) corresponding point (III) and (d) corresponding point (IV) shown in Fig. 5-2) (a) $U^* = 5.0$ ($Re = 2540$), (b) $U^* = 5.1$ ($Re = 2590$), (c) $U^* = 10.5$ ($Re = 5334$) and (d) $U^* = 10.6$ ($Re = 5385$).....	107
5-4	Amplitude of lift coefficient in the region of $U^* = 3.5 - 17.5$	108
5-5	(a) Motion amplitude, (b) frequency ratio and (c) amplitude of lift coefficient at $Re = 1778$	109

5-6	(a) Motion amplitude, (b) frequency ratio and (c) amplitude of lift coefficient at $Re = 3556$	109
5-7	(a) Motion amplitude, (b) frequency ratio and (c) amplitude of lift coefficient at $Re = 5334$	110
5-8	(a) Motion amplitude, (b) frequency ratio and (c) amplitude of lift coefficient at $Re = 8890$	110
5-9	Motion amplitude at $Re = 2540$ and $Re = 2590$ as well as that from Fig. 5-2(a)...	113
5-10	Motion amplitude at $U^* = 5.0$ and $U^* = 5.1$	114
5-11	Motion amplitude at $Re = 5334$ and $Re = 5385$	114
5-12	Motion amplitude at $U^* = 10.5$ and $U^* = 10.6$	115
6-1	Mean drag coefficient and Strouhal number against Reynolds number for a fixed circular cylinder from Sumer and Fredsoe (1997).....	123

Chapter 1

Introduction

1.1 Engineering background

Vortex-induced vibration (VIV) can be found in many fields of engineering, such as riser tubes bringing oil from the seabed to the surface, tethered structures in the ocean, bridges, nuclear reactors, heat exchanger tubes, and high-rise buildings. VIV may cause large-amplitude vibration of structures and lead to structural damage or even collapse of the whole system. For instance, the incident of the Tacoma Narrows bridge in the U.S. state of Washington on November 7, 1940 is one of famous examples which occurs as a result of VIV ([Billah and Scanlan, 1991](#)). The break of a thermowell inside a pipe carrying sodium coolant in Japan Monju nuclear reactor on December 8, 1995 was also due to VIV, which caused a major fire of this reactor ([Khan et al., 2018](#)). One of the 265-foot-tall tower of the thriller ride, VertiGo in the U.S. state of Ohio on January 14, 2002 collapsed still because of VIV ([Khan et al., 2018](#)). It is therefore highly important and relevant to investigate the VIV problem.

VIV is a kind of motion as a result of the interaction between fluid and structure. When the fluid moves past an unstreamed blunt body, for Reynolds number above a critical value, an unsteady wake is created even if the incoming flow is steady, and vortices shedding may occur alternatively at either side of a slender transverse body. These shed vortices result in oscillating forces on the body. The oscillating force may be strong enough to generate body vibration. Such phenomenon is known as VIV. The study on VIV has a wide range of practical interests in ocean engineering. There are various types of offshore structures designed for floating wind turbine and oil platforms. They usually have a large number of cylindrical components. Risers, mooring lines and pipelines are also extensively utilized. It is common that VIV occurs in this type of structure. This may be an important source of the fatigue damage of cylindrical components and further cause environmental issues.

The results from [Wanderley *et al.* \(2012\)](#) indicated that the three-dimensionality had insignificant influence on the motion amplitude and frequency of a relatively long cylinder in the sub-critical turbulent range. Later, [Wanderley and Soares \(2015\)](#) and [Pigazzini *et al.* \(2018\)](#) provided the similar conclusion. In such a case, the scope of this PhD study is to undertake two-dimensional (2D) numerical simulations for VIV of circular cylinders in the laminar and sub-critical turbulent ranges using multi-block immersed boundary-lattice Boltzmann method (IB-LBM). Lattice Boltzmann method (LBM) has become an alternative to Navier-Stokes (NS) equations, while they are equivalent for simulating fluid flows ([Chen and Doolen, 1998](#)). LBM is based on microscopic models and mesoscopic kinetic equations. Its equations may appear to be very different, but they are in fact equivalent to the NS equations. It has some distinctive features, such as the simple algorithm and the natural parallelism ([Chen and Doolen, 1998](#)). IBM is used to treat the structure-fluid boundary. The body surface is replaced by a layer of distributed force, whose value is determined by the no-slip boundary. It allows a complex boundary to be treated in a simpler way. It aims to uncover some of the physical mechanism of this problem and provide some practical solutions for engineering design through the following three aspects. First, a structure may have multi-components. Their interactions may be important for the whole system, and thus the fluctuating force acting on two stationary cylinders in different arrangements will be considered systematically. Second, a cylinder can be set into motion. The characters of the motion can have serious implications to the safety of the structure. An approach to understanding the fluid- structure is to control the motion of the body, or forced motion as commonly called. In the forced oscillation, the motion of the body is prescribed and response of the wake to the motion can be examined in isolation. It is easier to do forced motion systematically than the free motion. It is part of the purpose of this work to provides the mathematical analysis for the conditions of the equivalent forced and free motions first, and then uncover the motion characters of a free cylinder through the results from forced motion, including how the combined mass-damping parameter influences the motion amplitude. Third, real engineering problems correspond to high Reynolds number. The methodology will be refined with multi grids and turbulence model. The well-known motion amplitude branches will be investigated systematically.

1.2 Literature review

1.2.1 Flow past two stationary cylinders in different arrangements

The flow past bluff bodies is common in engineering applications, such as offshore wind farms, oil exploration, bridge pilings and high-rise buildings. Compared with the flow over a single bluff body, the wake interference between multiple bluff bodies gives rise to the complete change of the flow characteristics, including the vortex shedding, which leads to a very different pattern of the force acting on the cylinder (Sumner, 2010; Jiao and Wu, 2018a). Thus, some insightful analysis into flows in such a case have important implications to vortex-induced vibration. Here, two identical circular cylinders of equal diameter will be taken into consideration.

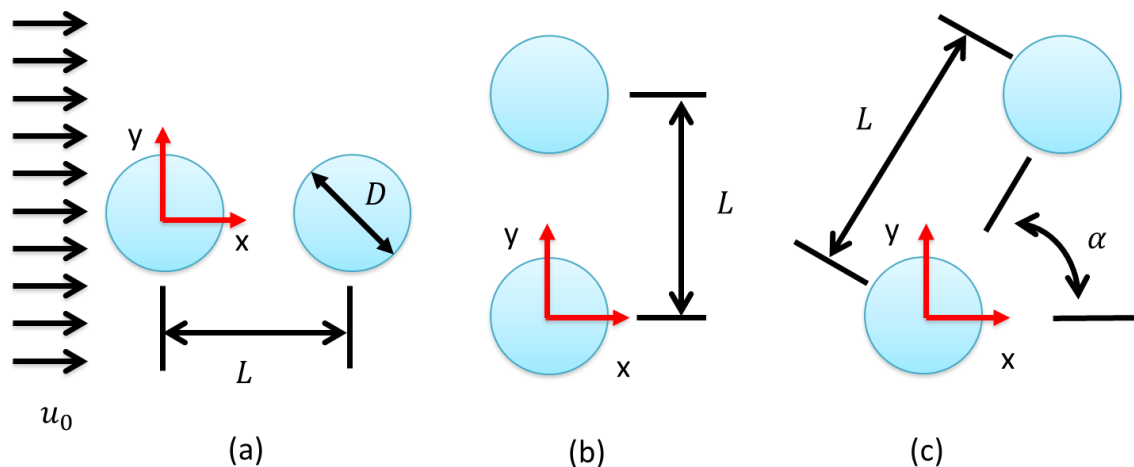


Fig. 1-1 Arrangements of two cylinders: (a) tandem; (b) side-by-side and (c) staggered arrangements

Flow characteristics in the two-cylinder system depend on the ratio of the centre-to-centre spacing (L) to the cylinder diameter (D), $L^* = L/D$, the alignment angle (α) between the line linking two cylinder centres and flow direction, as well as Reynolds number $Re = u_0 D / \nu$, where u_0 is the incoming free-stream velocity, and ν is the kinetic viscosity. Arrangements of two cylinders can be classified into three categories shown in Fig. 1-1, including tandem ($\alpha = 0^\circ$), staggered ($0^\circ < \alpha < 90^\circ$) and side-by-side ($\alpha = 90^\circ$). Reviews of earlier work were given by Zdravkovich (1977; 1987; 2003) and more recent ones by Sumner (2010). Broadly speaking,

at sufficient small L^* , the two cylinders behave like a single bluff body, while at sufficiently large L^* , they behave like two independent bodies in the free-stream and wake interaction between two cylinders vanishes. It is within certain range of L^* , the interactions between the flows past two cylinders become highly complex.

For cylinders in tandem arrangement, or $\alpha = 0^\circ$, Zdravkovich (1987) discussed some essential features for this case based on experimental evidence. These features in the wake were also observed later by many numerical simulations (Slaouti and Stansby, 1992; Mittal et al., 1997; Meneghini et al., 2001; Carmo and Meneghini, 2006). The two cylinders can be combined as a single bluff-body shown in Fig. 1-2(a) when $1 < L^* < 1.2 - 1.8$ (Zdravkovich, 1987). The free shear layer by the upstream body will pass by the downstream cylinder and the vortex shed from the two cylinders will be mainly in the wake behind the downstream cylinder. The oscillation of the flow is mainly periodic with period T_v . This gives the frequency $f_v = 1/T_v$, which is usually defined through the Strouhal number $St = f_v D / u_0$. Although the oscillation may have frequency components $n f_v$ ($n = 1, 2, 3 \dots$), $n = 1$ is usually dominant and it is usually referred as a single frequency oscillation. When $1.2 - 1.8 < L^* < 3.4 - 3.8$ (Zdravkovich, 1987), shear layer shed from the upstream body will reattach at the downstream body and a vortex street is formed only behind the downstream cylinder shown in Fig. 1-2(b). The oscillation of the flow is still dominated by a single frequency. When $3 < L^* < 4$ (Zdravkovich, 2003) or $3 < L^* \leq 5$ (Xu and Zhou, 2004), the wake pattern behind the upstream cylinder or before the downstream cylinder may intermittently change between attachment on the downstream cylinder and eddy shedding from the upstream cylinder at a higher Reynolds number, say at an order around $O(10^4)$, and it is referred as “bi-stable flow” (Igarashi, 1981) shown in Fig. 1-2(c). The oscillation of flow has two different periods and two dominant frequency components at the bi-stable regimes. This can be understood by the fact for the upstream cylinder the incoming flow is steady and uniform. The flow behind the upstream cylinder or before the downstream body is, however, oscillatory. A new kind of oscillatory flow could be generated by the second cylinder, and hence two frequency components or bi-stable flow phenomenon. When $L^* > 3.4 - 3.8$ (Zdravkovich, 1987), the shed vortex will appear evidently behind each of the cylinders or co-shedding shown in Fig. 1-2(d) will occur. The oscillation is once again dominated by a single frequency. This could

partly be due to the lock in effect (Xu and Zhou, 2004). Also, at relatively lower Reynolds number, the oscillatory flow behind the upstream cylinder will decrease faster away from the cylinder because of the larger viscous effect. Thus as L^* increases, the flow to the downstream cylinder becomes more uniform. The value of the single frequency at this range of L^* is still different from that of an isolated cylinder. It can be expected, however, as L^* further increases, the frequency will tend to that corresponding to a single cylinder.

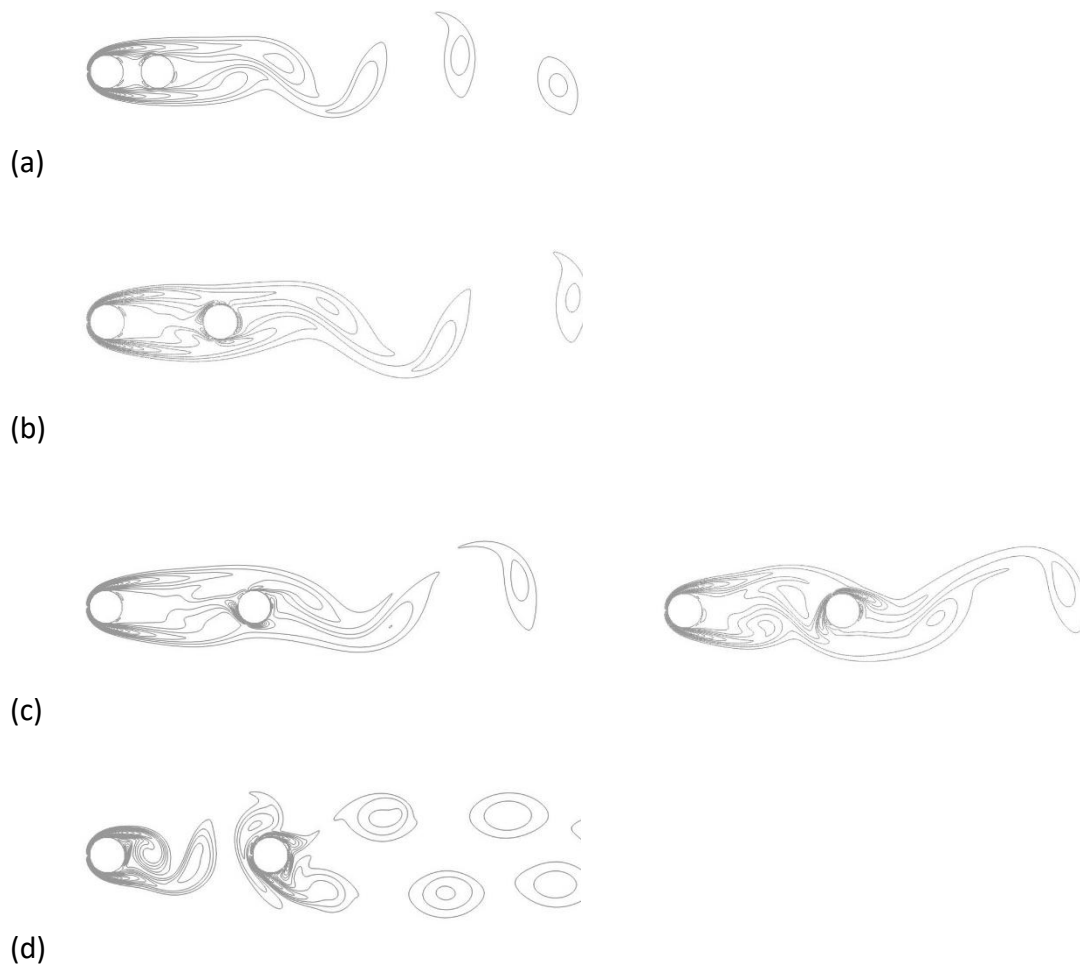
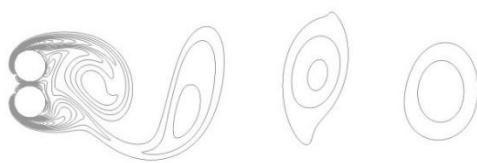
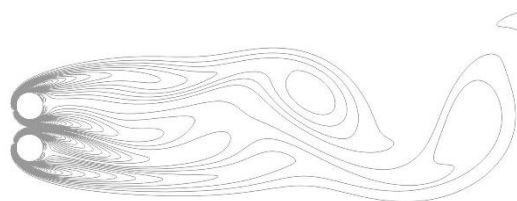


Fig. 1-2 Instantaneous vorticity contours with $\alpha = 0^\circ$ according to the wake pattern: (a) extended-body pattern; (b) reattachment pattern; (c) bi-stable pattern; (d) co-shedding pattern.

For the flow past two side-by-side ($\alpha = 90^\circ$) cylinders, detailed discussions can be found in Bearman and Wadcock (1973), Williamson (1985), Kim and Durbin (1988), Sumner *et al.* (1999), Zhou *et al.* (2002), Kang (2003), Carini *et al.* (2014) and Singha *et al.* (2016). Sumner (2010) identified three flow regimes. When $1 \leq L^* \leq 1.1 - 1.2$, the flow behaves in a manner similar to that corresponding a single bluff-body, or “the single body case” shown in Fig. 1-3(a). The oscillation of the flow is dominated by a single frequency. The Strouhal number is not sensitive to L^* within this range and its value is lower than that of a single cylinder. When $1.1 - 1.2 \leq L^* \leq 2 - 2.2$, the gap flow between two side-by-side cylinders is asymmetrical and biased towards one cylinder. The bias may be permanent, the “deflected case” shown in Fig. 1-3(b) or alternate randomly, the “flip-flopping case” shown in Fig. 1-3(c). For deflected patterns, the developed flow is periodic and the oscillation of the flow is still dominated by a single frequency. For flip-flopping patterns, however, highly complex wake and vortex-street interaction occur. The oscillation of the flow is no longer periodic and therefore the frequency of flow oscillation is a broadband spectrum rather than discrete. When $L^* \geq 2 - 2.5$, two parallel synchronized vortex streets are formed, which can be either symmetric about the centreline between the cylinders, the “anti-phase case” shown in Fig. 1-3(d), or anti-symmetric, the “in-phase case” shown in Fig. 1-3(e). For both of these two cases, the flow is periodic and the flow oscillation is dominated by a single frequency, whose value is close to that for an isolated cylinder.



(a)



(b)

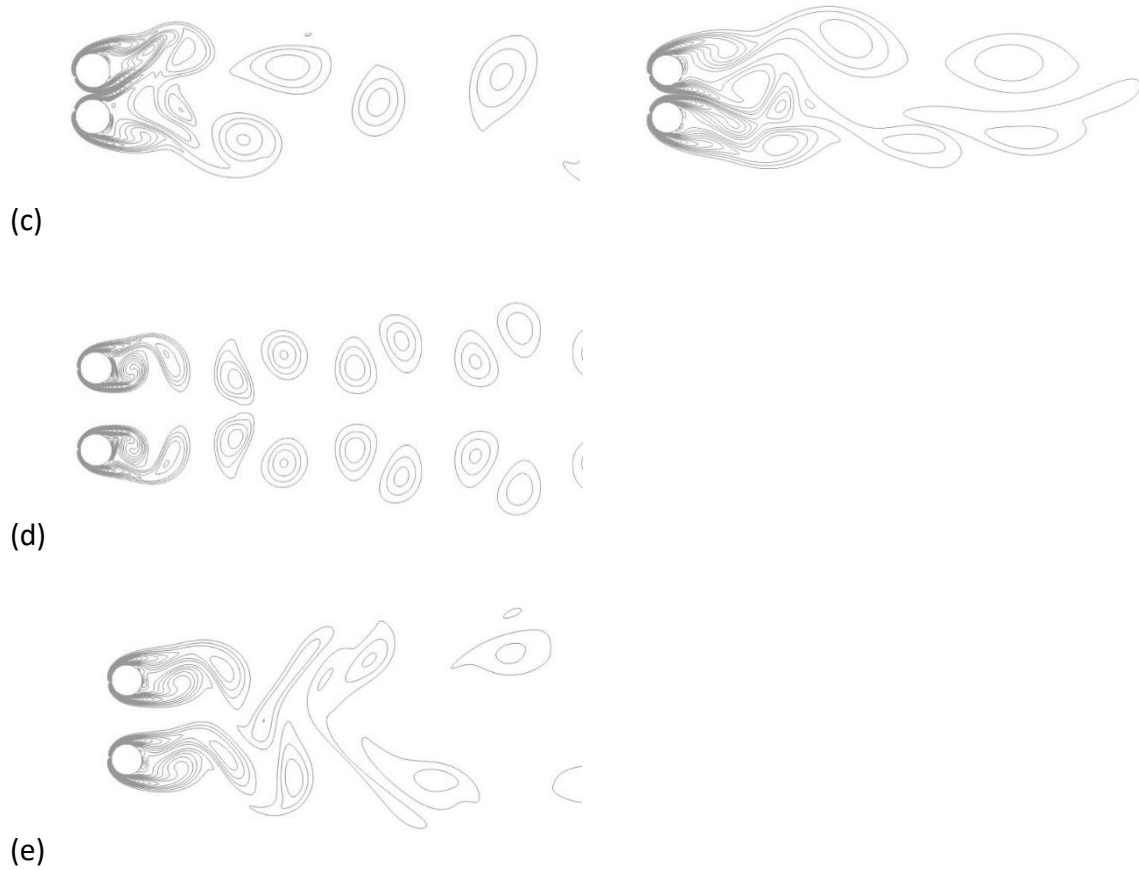
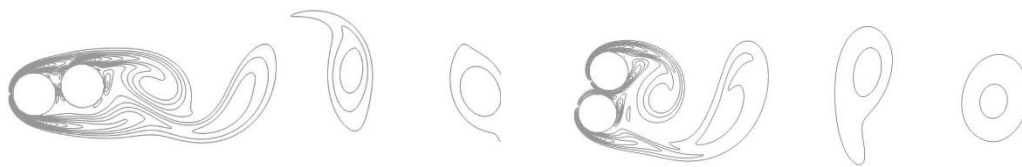


Fig. 1-3 Instantaneous vorticity contours with $\alpha = 90^\circ$ according to the wake pattern: (a) single bluff-body pattern; (b) deflected pattern; (c) flip-flopping pattern; (d) antiphase-synchronized pattern; (e) in-phase-synchronized pattern.

For two staggered ($0^\circ < \alpha < 90^\circ$) cylinders, studies have been undertaken by [Kiya *et al.* \(1980\)](#), [Zdravkovich \(1987\)](#), [Sumner *et al.* \(2000\)](#), [Jester and Kallinderis \(2003\)](#), [Akbari and Price \(2005\)](#), [Hu and Zhou \(2008a; 2008b\)](#) and [Tong *et al.* \(2015\)](#). [Sumner \(2010\)](#) provided a comprehensive review. The interactions involve four shear layers from the upper and lower sides of two cylinders, Karman vortex formation process as well as two Karman vortex streets. The complex nature of the interactions depends on both the spacing ratio L^* and the alignment angle α . It is suggested that the behaviour of the St data can be classified into three groups by spacing ratio L^* . At all α and small spacing with $1 \leq L^* \leq 1.25$ ([Sumner *et al.*, 2000](#)), the behaviour of the flow is similar to that of a single-bluff body shown in Fig. 1-4(a). At $\alpha \leq 30^\circ$ and $1.125 \leq L^* \leq 3 - 4$ ([Sumner *et al.*, 2000](#)) the vortex shed by the lower cylinder is mostly suppressed shown in Fig. 1-4(b), while at large spacing ratio ($L^* > 3 - 4$)

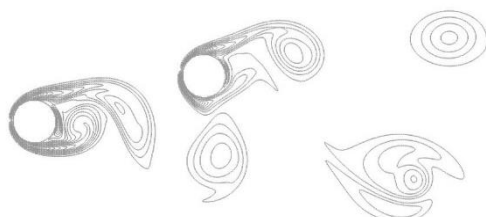
(Sumner *et al.*, 2000), in its near-wake region, an uninhibited vortex street can be formed, similar to a single, isolated circular cylinder shown in Fig. 1-4(c). The oscillation at $\alpha \leq 30^\circ$ is dominated by a single frequency. The bi-stable case was not discussed in Sumner (2010), which could be due to the fact the Reynolds number is not the same as that in Igarashi (1981). At $\alpha \geq 30^\circ$ and $L^* \geq 1.25$ (Sumner *et al.*, 2000), the shed vortex occurs from each of the cylinders shown in Fig. 1-4(d). For most but not all cases, the oscillation of the flow is dominated by two frequencies. The difference between these two frequencies becomes smaller as the distance of two cylinders becomes larger and the wake interference weakens. When L^* further increases, the two pronounced frequency cases are hardly observed and the oscillation is dominated by a single frequency. At $L^* \geq 1.25$, which covers the flip-flopping region for the side-by-side case, the oscillatory behaviour of the flow is expected to very much depend on α . The frequency components change from some discrete values to a continuous spectrum, which is a focus of the current investigation.



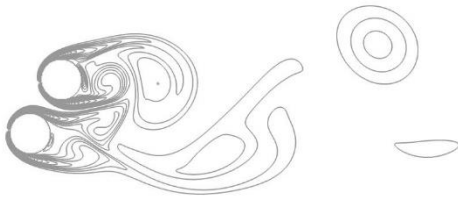
(a)



(b)



(c)



(d)

Fig. 1-4 Instantaneous vorticity contours with $0^\circ < \alpha < 90^\circ$ according to the wake pattern: (a) single bluff-body pattern with smaller (left) and larger (right) alignment angle; (b) reattachment pattern with smaller alignment angle; (c) co-shedding pattern with smaller alignment angle; (d) co-shedding pattern with larger alignment angle.

1.2.2 Relationship between transverse-only forced and free vibration

After having discussed the system with fixed cylinders, we will focus on a free cylinder in a fluid stream. At Reynolds number above a critical value, the vibration of the cylinder in transverse and in-line directions may occur. The lift (transverse) fluctuation is usually much larger than the drag (in-line) fluctuation, especially in the lock-in regime where the frequency of the periodic wake vortex mode matches the body oscillation frequency (Williamson and Govardhan, 2004). Thus, here the transverse-only oscillation in the lock-in regime is considered. There are two kinds of VIV: (1) free vibration where the cylinder oscillates freely under vortex-induced motion and (2) forced oscillation where the cylinder is prescribed to have a sinusoidal motion. Forced oscillation, allowing the response of the wake to the motion to be examined in isolation, can be used to predict its related free vibration. Reviews of the earlier work on forced and free motions were given by Bearman (1984), Blevins (1990) and Sumer and Fredsoe (1997) and more recent ones by Williamson and Govardhan (2004) and Bearman (2011).

Fluid parameters which have significant effect on both forced and free motions include the fluid density ρ , kinematic viscosity ν and incoming velocity u_0 . In the forced sinusoidal oscillation of a cylinder, important parameters are the motion frequency f_c , motion amplitude Y_0 and its diameter D . In the free vibration, the body mass m , structural damping

b and structural stiffness k become important together with D , while motion frequency and amplitude are to be determined instead of being prescribed. The rationale of using forced oscillation results to predict free vibration is based on energy transfer $E_{fc} = \int_0^{T_c} F_L(t) \dot{Y}(t) dt$ from the flow to the cylinder over a period T_c . Here F_L is the lift force of the body by the fluid and \dot{Y} the oscillation velocity of the body. In the forced oscillation, results are obtained at various prescribed motion frequencies f_c and motion amplitudes Y_0 . It is common that energy transfer contours are plotted with f_c and Y_0 being the horizontal and vertical axes, respectively. In the free motion, body mass m and structural damping b are given together with structural stiffness k . The free motion frequency f_c and amplitude Y_0 can be obtained from the measurement or simulations. Comparison could then be made between the energy transfer in the free motion and that on the energy transfer contours of the forced motion to see the compatibility of these two motions.

The comparison between the forced and free motions is based on the assumption of their equivalence. One should note that the forced motion is imposed by an external force. If the external force could be replaced by the corresponding mechanic mechanism, such as the structural damping b and structural stiffness k , the forced motion is then equivalent to the free motion with such a mechanic mechanism without external force. A necessary condition for this equivalence is a positive value of E_{fc} , which represents net energy transfer from the flow to the cylinder. [Leonitini et al. \(2006\)](#) undertook numerical studies on both forced and free motions at Reynolds number $Re = 200$ by a spectral-element technique coupled with a high-order three-step time-splitting scheme. It should be noted that ρ , u_0 and D are used for nondimensionalisation and the normalized parameters are marked by * below. A zero-energy contour $E_{fc}^* = \frac{E_{fc}}{0.5\rho u_0^2 D^2} = 0$ on the $f_c^* - Y_0^*$ plane was displayed in the lock-in region of the forced oscillation within $0.14 < f_c^* < 0.24$, where $f_c^* = \frac{f_c D}{u_0}$ and $Y_0^* = \frac{Y_0}{D}$. They also obtained E_{fc}^* from free vibration with a given body mass $m^* = \frac{m}{\rho D^2} = 10$ and structural damping ratio $\zeta = \frac{b}{2(m+M_p)\omega_n} = 0.01$ in the same motion frequency region as that of forced motion. Here $M_p = \frac{\pi}{4} \rho D^2$ is the potential flow added mass for a circular cylinder and $\omega_n = \sqrt{\frac{k}{m+M_p}}$ the

natural angular frequency of the body with the added mass effect. It was found that all E_{fc}^* from free vibration was in the zone of the positive energy transfer obtained from the forced oscillation, which was qualitatively consistent with the positive damping ratio ζ . [Kumar et al. \(2016\)](#) used a more stringent lock-in criterion, which was adopted to obtain energy transfer contour in lock-in forced motion at $Re = 100$. The free vibration with $\zeta = 0$ was considered. Its results of f_c^* and Y_0^* were used on the energy transfer contour of the forced motion and were found to lie almost on the $E_{fc}^* = 0$ line, which was quantitatively consistent with $\zeta = 0$.

Some other studies (e.g. [Hover et al., 1998](#); [Carberry et al., 2004](#); [Carberry et al., 2005](#)) have indicated that the results of f_c and Y_0 from the free motion could fall into regions of negative E_{fc} predicted from the forced oscillation, especially at high Reynolds number. Such a contradiction may be due to the fact that the free motion of a cylinder with constant stiffness and structural damping is in fact not fully sinusoidal as imposed in the forced oscillation. In other words, the external force in the forced sinusoidal motion cannot be equivalently replaced by the constant mechanical damping and stiffness. In general, the motion in forced oscillation can be prescribed precisely sinusoidal, while the hydrodynamic force may not be exactly sinusoidal, especially at high Reynolds number. In such a case, exactly equivalent free motion of a cylinder with constant structural stiffness and damping is no longer possible. For example, [Hover et al. \(1998\)](#) compared some results from forced and free vibrations in the regime of $1/12 < f_c^* < 1/3$ at $Re = 3800$ and at zero energy transfer condition. The nondimensionalized mass was set as $m^* = \pi/4$ and structural damping ratio was taken as $\zeta = 0$ in the free motion. It was found that in the most cases the values of Y_0^* and f_c^* from the free motion were not on the zero energy transfer encounter line obtained from the forced motion, including the case of the largest Y_0^* in the free motion. This means that the external force in the forced motion could not be exactly replaced by the mechanical system with constant damping and stiffness.

[Staubli \(1983\)](#) and [Morse and Williamson \(2009a\)](#) adopted a method different from that mentioned above to investigate the rationale of using forced oscillation results to predict free vibration. Both the maximum value of lift force F_{L0} and phase angle ϕ between lift coefficient

and cylinder motion can be measured from forced motion at various f_c and Y_0 first, and then the response of possible lock-in free motions with various structural stiffnesses k (or various natural frequencies of the cylinder f_n) at a given m and b can be predicted based on results from forced oscillation. Comparison can be subsequently made between the predicted free motion results and those corresponding real free motion results. [Staubli \(1983\)](#) used experimental data from forced oscillation with $Y_0^* = (0, 0.8)$ and $f_c^* = (0.09, 0.33)$ at $Re = 60000$ to make prediction for the response of free vibration with a given $m^* = 247.78$ and $\zeta = 0.00356$, and then compared with experimental measurements of free vibration from [Feng66](#). The prediction was reasonable for natural frequency within $f_n^* = (0.15, 0.2)$, but was not close at $f_n^* = (0.12, 0.15)$. It ought to be pointed out that the Reynolds number of the free-vibration experiment of [Feng \(1968\)](#) was not fixed at $Re = 60000$ and therefore the conditions for the forced motion and free motions were not exactly the same. [Morse and Williamson \(2009a\)](#) extended the frequency and amplitude ranges of forced oscillation to predict free-vibration response at a different Reynolds number $Re = 4000$. The motion amplitude was taken as $Y_0^* = (0, 1.6)$ and the frequency $f_c^* = (0.0625, 0.5)$. Two free vibration cases at (1) $\zeta = 0$ and (2) $\zeta = 0.0232$, respectively, with $m^* = 8.24$ were predicted by the results of the forced oscillation. Comparison was then made with the corresponding real free motion data from [Govardhan and Williamson \(2006\)](#) in which Reynolds number was not always the same either. A good agreement was nevertheless found close to the peak amplitude Y_{0max}^* , where Reynolds numbers of [Morse and Williamson \(2009a\)](#) and [Govardhan and Williamson \(2006\)](#) were matched.

It can be seen that far fewer studies have systematically considered the relationship between forced oscillation and free vibration. In this work, the rationale of using the results from the transverse forced oscillation of a cylinder in the lock-in region to predict the corresponding free vibrations will be provided based on the mathematical analysis and verified through the numerical results. In addition, from the mathematical analysis, we will show that when a body of mass m_1 , stiffness k_1 and damping b_1 is found to be in sinusoidal motion with frequency ω_c and amplitude Y_0 , its motion will be the same at m_2 , k_2 and b_2 if $m_2 - m_1 = (k_2 - k_1)/\omega_c^2$ and $b_2 = b_1$. This can be linked to the studies on how the parameter $m^*\zeta$ influences the motion amplitude, which is an important question in VIV investigations

(Vickery and Watkins, 1964; Skop, 1974; Williamson and Govardhan, 2004). It has been well established that for $m^* = O(100)$ and $\zeta = O(0.001)$ (or $m^*\zeta > 0.1$), the amplitude at resonance is usually the largest. In such a case, the largest motion becomes a unique function of the combined $m^*\zeta$ parameter at resonance, or $(m^* + M_p^*)\zeta$ in the case where the added mass is also important. Here, $M_p^* = \frac{M_p}{\rho D^2} = \frac{\pi}{4}$ is the nondimensionalized potential added mass for a circular cylinder. The logic for this can be shown that the motion amplitude can be obtained as $Y_0^* = \frac{C_{L0} \sin \phi}{16\pi^2(m^* + M_p^*)\zeta} \left(\frac{U^*}{f^*}\right)^2 f^*$ (Bearman, 1984; Khalak and Williamson, 1999). Here $U^* = 1/f_n^*$ is the reduced velocity, $f^* = f_c^*/f_n^* = \sqrt{\frac{m^* + M_p^*}{m^* + M_e^*}}$ is the ratio between body motion frequency f_c^* and its natural frequency f_n^* , where $M_e^* = \frac{C_{L0} \cos \phi}{8\pi^2 Y_0^*} \left(\frac{U^*}{f^*}\right)^2$ is the effective added mass due to the lift force in phase with body acceleration. At resonance, $f^* = 1$, and thus the amplitude can be written $Y_0^* \propto \frac{C_{L0} \sin \phi}{(m^* + M_p^*)\zeta}$, which depends on $(m^* + M_p^*)\zeta$. For $m^* = O(1 \sim 10)$ and $\zeta = O(0.001)$ (or $m^*\zeta \ll 0.1$), the large response, including the peak response, may not always be found at resonance, but at a different frequency of lock-in region, where the body oscillation frequency matches with that of the periodic wake vortex mode (Sarpkaya, 1995; Khalak and Williamson, 1999). In the region of lock-in, f^* may be no longer equal to one. For instance, f^* was about 1.4 for the largest free motion with $m^* = 2.4$ and $\zeta = 0.0045$ in the lock-in region Williamson and Govardhan (2004). From the result, it has been suggested that the amplitude is no longer a unique function of $(m^* + M_p^*)\zeta$, as $f^* = 1$ in the case of at large m^* . The dynamic response of the free motion would be affected by $m^* + M_p^*$ and ζ independently, not just by $(m^* + M_p^*)\zeta$ as a single parameter (Khalak and Williamson, 1996). This has led to a conclusion seemingly contradicting to the one mentioned previously. The fact is most earlier studies might have focused on the high mass ($m^* = O(100)$) in aerodynamic applications where the fluid is air, not the low mass ($m^* = O(1 \sim 10)$) in hydrodynamic fields where water is the fluid medium. For the high m^* , the difference between M_e^* and M_p^* can be neglected in $f^* = \sqrt{\frac{m^* + M_p^*}{m^* + M_e^*}}$, compared with m^* in the lock-in free motion. Therefore, f^* is very close to unity and may be regarded as 1 approximately in the full lock-in region. Thus, the largest motion occurs always at f^* close to 1. For the low m^* , the effect of the difference between M_e^* and M_p^* is relatively more significant in the lock-in free

motion, and thus f^* may not be close to unity in the most part of the lock-in region, including that at the peak response.

1.2.3 Effect of Reynolds number on VIV amplitude branches

Apart from $(m^* + M_p^*)\zeta$ discussed in the previous section, another parameter on VIV is Reynolds number, which is generally neglected in discussions of motion amplitude (Bearman, 2011). Most previous experimental studies (e.g. Feng, 1968; Skop 1974; Griffin 1980; Anagnostopoulos and Bearman, 1992; Khalak and Williamson, 1996; Newman and Karniadakis, 1997) on the transverse free vibration of a cylinder fixed structural parameters (m , k , b and D) and the fluid medium (ρ and ν), and varied the incoming fluid velocity u_0 . In general, the response of the nondimensional cylinder motion amplitude Y_0^* depends on the nondimensional mass m^* , damping ratio ζ , reduced velocity U^* and Reynolds number Re . It means that in the experiment both U^* and Re could change with u_0 . Then simulations tried to capture what was observed in experiments and thus followed the same practice. These early experimental and numerical studies assumed that the effect on the results was attributed to the variation of U^* rather than the Reynolds number. A possible reason may be that in the sub-critical turbulence range, St is found not to be too much affected by Re or to be nearly constant with a value of 0.2, as discussed in reviews by Williamson (1996) and Sumer and Fredsoe (1997). Also, the amplitude of C_L for a fixed cylinder was considered to be not very much affected by Re or to be nearly constant with a value of about 0.3 (Skop and Griffin, 1973; 1975). Then, the early assumption was that the amplitude of C_L would not be significantly affected by Re for a free body either. Therefore, as pointed out by Bearman (2011), “there was a popular belief at the time that Reynolds number plays a minor role and that the flow around a cylinder undergoing large vortex-induced vibrations is insensitive to Reynolds number changes”.

Based on the more extensive work (e.g. Norberg, 2003; Klamo *et al.*, 2005; Govardhan and Williamson, 2006; Morse and Williamson, 2009b; Wanderley and Soares, 2015) undertaken later on, it is found that the effect of Re is important for various results (Bearman, 2011). For example, Norberg (2003) reviewed data of the root-mean-square lift coefficient C_{Lrms} acting

on a stationary cylinder in the sub-critical turbulent range. Results indicated that even though the value of C_{Lrms} was usually about 0.27, around $Re \approx 1600$ it suddenly dropped to 0.048. This suggested that the effect of Re on C_L for a fixed cylinder could not be always ignored. For a free body, the variation of C_L with Re should be more complex compared with that of a fixed cylinder, and thus the Re effect on free motions may need to be considered. [Klamo et al. \(2005\)](#) investigated the effect of Reynolds number in the range $Re = 525 - 2600$ on the maximum amplitude of a cylinder free motion. In their experiments, both U^* and Re still changed with the incoming fluid velocity u_0 at given m^* and ζ . A curve of motion amplitude Y_0^* against U^* was plotted between $U_1^* < U^* < U_2^*$, with $Re_1 < Re < Re_2$, where Re_1 and Re_2 correspond to U_1^* and U_2^* , respectively. Then, values of m^* and ζ remained unchanged, while f_n was varied. To achieve the same range U^* , u_0 was changed and therefore Re too. Another curve of motion amplitude Y_0^* against U^* between $U_1^* < U^* < U_2^*$, with $Re_3 < Re < Re_4$ was plotted, where Re_3 and Re_4 correspond to U_1^* and U_2^* with new u_0 , respectively. Comparing Y_0^* values from the two curves at same U^* , they found that at larger Re , the peak amplitude of the cylinder motion was also larger and pointed out that the Reynolds number was an important parameter for the maximum amplitude. [Govardhan and Williamson \(2006\)](#) extended the Re range to 500 – 33000 to investigate its effect on the maximum motion amplitude and presented a similar conclusion to that from [Klamo et al. \(2005\)](#).

Later, [Wanderley and Soares \(2015\)](#) did numerical study. For given m^* and ζ , a curve of Y_0^* was plotted against U^* at a fixed Re . Curves Y_0^* at other Re values were also plotted against the same range of U^* . Similarly, curves for dominant frequency f_c^* of cylinder motion against U^* were plotted. In particular, four different Re values in the sub-critical turbulence range were chosen, or $Re = 300, 400, 1000$ and 1200 . The body mass was $m^* = 1.88$ and damping ratio $\zeta = 0.00542$. It was found that the effect of Re was significant. With the increase in Re , the range of U^* within which lock-in occurred became much larger. In addition, at the same U^* , the value of motion amplitude from higher Reynolds number was higher than that from lower Reynolds number.

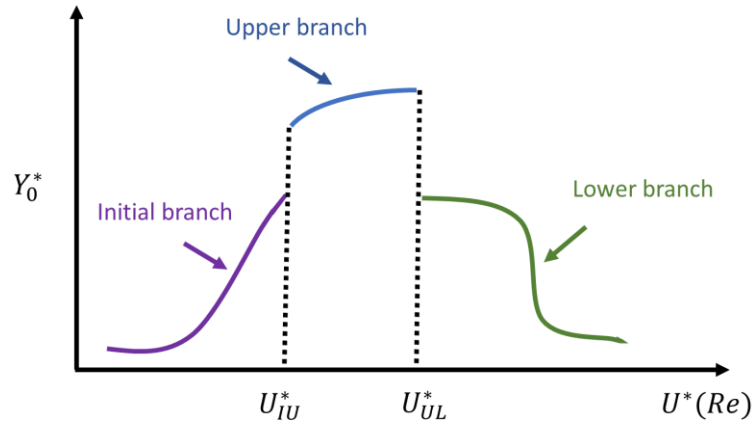


Fig. 1-5 The type of the motion amplitude curve of a low mass cylinder against reduced velocity (or Reynolds number).

One of the important features of the motion amplitude curve of a low mass cylinder ($m^* = O(1\sim 10)$) against U^* is that it has jumps. [Khalak and Williamson \(1997, 1999\)](#) observed that for $m^* = O(1\sim 10)$, there were three branches of response in the curve, shown in Fig. 1-5. The curve started with an initial branch at lower U^* , then became an upper branch when U^* was beyond a critical value and dropped to a lower branch as U^* further increased to be beyond another critical value. Therefore, there are two jumps in the curve at: (1) the transition between initial-upper branches and (2) the transition between upper-lower branches. In the initial branch, with the increase of U^* , Y_0^* also increased. Further increase of U^* to a critical value U_{IU}^* , Y_0^* jumped nearly vertically from initial branch to the upper branch. The peak of the motion amplitude was located in the upper branch. As U^* continued to increase to the next critical value U_{UL}^* , the transition between upper-lower branches occurred, and Y_0^* dropped nearly vertically. It should be noted that in experiments mentioned above, U^* and Re both changed with u_0 and Re was in the range of 2000-14000. In the work of [Wanderley and Soares \(2015\)](#) mentioned previously, Re was fixed in the curve Y_0^* against U^* and was in the range $Re = 300 - 1200$. With the increase of U^* , Y_0^* increased slowly. Further increase in U^* , Y_0^* jumped to its peak first and then decreased. The curve changed rapidly before its peak, and thus there was only one critical value U_{IU}^* connecting initial and upper branches, no U_{UL}^* where Y_0^* dropped nearly vertically. It seems that the effect of Re on the response branches may be important and it may affect the response branches.

1.3 Research questions, objectives and contributions

This thesis focuses on how the fluid interacts with circular cylinders during VIV using an in-house code developed based on immersed boundary-lattice Boltzmann method. According to different physical scenarios, four research questions have been considered in this thesis, namely,

Q1. How do detailed frequency components of forces on two stationary cylinders in tandem, side-by-side and staggered arrangements vary with different alignment angle?

Q2. Can the free motion be predicted using results from the corresponding forced motion?

Q3. Under what conditions does the free motion depend only on the combined mass-damping parameter?

Q4. How does Reynolds number influence the well-known three response branches, when Reynolds number and reduced velocity are considered as independent parameters?

From the literature review of two stationary cylinders in different arrangements in Section 1.2.1, most previous studies focused on wake patterns and forces at the dominant frequency. However, at an intermediate centre-to-centre spacing, the wake and vortex-street interaction with the alignment angle α become highly complex. The fluid force is periodic and dominated virtually by a single frequency component in the tandem arrangement. It is random with a continuous frequency spectrum in the side-by-side arrangement. Here, random means that the components of the force are not in the form of discrete frequencies but are in the form of continuous spectrum. This motivates us to study detailed frequency components or spectrum of lift and drag coefficients at different α in **Q1**. This thesis will provide a careful consideration of this evolution process with α . Detailed frequency components or spectrum of lift and drag coefficients at different α will be carefully studied. Furthermore, how the force and wake vary with α will be systematically investigated, including the change from one set of discrete frequency components to another set of discrete frequency components and the change from discrete frequency components to continuous spectrum. The results can help to estimate the fluid force acting on cylinders and minimize some unwanted characteristics of the system, including the severe oscillatory motion of the downstream cylinder due to the

vortex shed from the upstream cylinder and the adverse loads induced on the nearby cylinders.

In engineering problems, the tensioned cables are often so long that their motions are easy to be excited. Thus, after considering the system with fixed cylinders in **Q1**, we will focus on a free cylinder in a fluid stream. Questions from **Q2** to **Q4** are of significant interest, as reviewed by [Williamson and Govardhan \(2004\)](#) and [Bearman \(2011\)](#). There have been a large number of experimental and numerical efforts to investigate the transverse forced oscillation of a cylinder, especially its lock-in phenomenon. Equally, there is also a large body of work on a cylinder in free motion due to the excitation of the incoming flow. However, far fewer studies have considered systematically the relationship between forced oscillation and free vibration, which is the motivation in **Q2**. The rationale of using the results from the transverse forced oscillation of a body in the lock-in region to predict the corresponding free vibration is provided based on the mathematical analysis and verified through the numerical results. It is also shown through mathematical analysis that when the structural damping is fixed, if the body mass and stiffness vary together following a particular relationship, or $m_2 - m_1 = (k_2 - k_1)/\omega_c^2$, the free motion will remain the same. With this conclusion, the relationship between the combined mass-damping parameter and motion amplitude in **Q3** may be uncovered. It has been well established that the motion amplitude at the resonance depends on only the mass-damping parameter $(m^* + M_p^*)\zeta$ not the two parameters, mass and damping, separately. The importance of the result has been widely recognized ([Williamson and Govardhan, 2004](#)). We aim to extend this important result to other frequencies and the result at the resonance frequency will be a special case. The damping ratio is redefined as $\zeta_c = b/2(m + M_p)\omega_c$. Here the motion frequency of the body ω_c is used instead of natural frequency of the body ω_n . Using this definition, we are then able to conclude that when a sinusoidal free motion of a cylinder is achieved, its motion will remain the same if (1) the mass-damping $(m + M_p)\zeta_c$ remains unchanged, and (2) the variation of $m + M_p$ and that of the stiffness k follow a particular relationship. In this sense, even away from the resonance, the different $m + M_p$, whether it is high or low, the motion of the body will always be the same,

provided the above conditions are met. In other words, the motion will depend on mass-damping $(m + M_p)\zeta_c$, even when the individual $m + M_p$ and ζ_c change.

The study of **Q3** leads us to the further research on the effect of another parameter, Reynolds number on VIV, or **Q4**. Here turbulent flow is considered. Large eddy simulation as turbulent model is incorporated into IB-LBM. Multi-block grid method is used to improve the numerical efficiency and accuracy. The grid is finer near the fluid-structure boundary, where the flow is usually more complex, while it is coarser away from the body. It is well established that when the variation of Reynolds number changes with the reduced velocity, there are three branches in the motion amplitude curve of a low mass cylinder, including initial, upper and lower branches connected by two jumps. However, in this thesis, Reynolds number and reduced velocity are considered as independent parameters. We shall focus on the case with Re , within which the curve of motion amplitude has two jumps and three branches when the variation of Reynolds number changes with the reduced velocity. This study will systematically investigate the effect of Reynolds number on free motions in the lock-in region. For instance, (1) how Re will affect both critical values, U_{IU}^* and U_{UL}^* at which the jump occurs; (2) how it will affect the shape of the curve within each branch; (3) how the motion amplitude changes near the jump when the reduced velocity is fixed while the Reynolds number varies.

1.4 Lists of publications

This thesis contains the contents of the following three papers, the second of which was chosen as one of the best papers of *Physics of Fluids*. They are listed below:

[1] **H. Jiao** and G. X. Wu. Analysis of fluctuating force acting on two cylinders in different arrangements through Lattice Boltzmann Method. *Journal of Fluids and Structures*, 82:101-120, 2018a.

[2] **H. Jiao** and G. X. Wu. Free vibration predicted using forced oscillation in the lock-in region. *Physics of Fluids*, 30:113601, 2018b.

[3] **H. Jiao** and G. X. Wu. Effect of Reynolds number on amplitude branches of vortex-induced vibration of a cylinder. Accepted by *Journal of Fluids and Structures*.

1.5 Thesis Layout

The thesis is composed of 6 chapters, which is organized as follow. Following the current chapter, the numerical method developed and used in this work is presented in Chapter 2, including the procedure of LBM, the equivalence between lattice Boltzmann equation (LBE) and Navier-Stokes (NS) equations, immersed boundary method (IBM) treating the structure-fluid boundary, large-eddy simulation (LES) as the turbulent model and multi-block method for improving the accuracy and the computational efficiency. In Chapter 3, the force acting on two identical circular cylinders of equal diameter in different arrangement is investigated, as well as the pattern of the vortex shedding. In Chapter 4, the rational procedure to predict the periodic free vibration of a cylinder based on results from the corresponding forced oscillation in the lock-in region is developed. The effect of Reynolds number on free motions in the sub-critical turbulent range is investigated systematically in Chapter 5, followed by conclusions in Chapter 6.

Chapter 2

Lattice Boltzmann Method

In this chapter, the theory and procedure of the lattice Boltzmann method (LBM) will be outlined. After presenting an introduction of lattice Boltzmann equation (LBE) in Section 2.1, we apply a method known as the Chapman-Enskog expansion to show the relationship between the LBE and Navier-Stokes (NS) equations in Section 2.2. Section 2.3 outlines immersed boundary method (IBM), which will be used for treating the structure-fluid boundary. This is followed by the large-eddy simulation (LES) for turbulent flow and multi-block method to improve accuracy and efficiency in computations.

2.1 Lattice Boltzmann Equation

Lattice Boltzmann method (LBM) has become an efficient algorithm for simulating fluid flows. Historically, LBM originated from lattice gas cellular automaton (LGCA), a simplified, fictitious molecular model where space, time and particle velocities are all discrete ([McNamara and Zanetti, 1988](#)). Later, [Abe \(1997\)](#) proved that it could also be viewed as a finite difference scheme for the continuum Boltzmann equation. Both approaches demonstrate that LBM is quite different from the traditional computational fluid dynamics (CFD) algorithms directly solving Navier-Stokes (NS) equations by some numerical schemes, such as finite-volume, finite-element or finite-difference methods. LBM is based on microscopic models and mesoscopic kinetic equations ([Chen and Doolen, 1998](#)). The major advantage of LBM is that it is much simpler to implement than traditional CFD. LBM does not involve Poisson equation which is difficult to solve due to its non-locality. The pressure in LBM can be calculated directly based on the equation of state. In addition, the heaviest computations in LBM are local, or restricted to within lattice nodes. It is easier to implement parallel for improving computational efficiency. Therefore, LBM will be used to simulate VIV in the present thesis.

LBM evolved out of LGCA. However, in order to provide clear physical pictures, we will introduce the lattice Boltzmann equation (LBE) and start from the Boltzmann equation (BE), an essential kinetic equation. BE is named after the Austrian Physician Ludwing Boltzmann. The fundamental variable of this equation is the particle density distribution function $f(\mathbf{x}, \boldsymbol{\xi}, t)$, which is a function of position \mathbf{x} , particle velocity $\boldsymbol{\xi}$ and time t . Consider a spatial domain $d\mathbf{x}$ around point \mathbf{x} and a velocity range $d\boldsymbol{\xi}$ around velocity $\boldsymbol{\xi}$. $f d\mathbf{x} d\boldsymbol{\xi}$ represents the total mass of the fluid particles within these domains at time t . In other words, the function f can be seen as the density of particles with velocity $\boldsymbol{\xi}$ at position \mathbf{x} and time t . It should be noticed that in some references, f can be also defined as the distribution function, which is the number of the fluid particles with velocity $\boldsymbol{\xi}$ at position \mathbf{x} and time t . Without loss of generality, the molecular mass M is assumed to be 1. The BE describes the transportation of f

$$\frac{\partial f}{\partial t} + \boldsymbol{\xi} \cdot \nabla f = \Omega(f, f), \quad (2-1)$$

Where ∇f is the gradient of particle distribution function and Ω is called the collision operator representing the rate of change in f due to binary molecular collisions (Huang, 1963; Wolf-Gladrow, 2000). Here, gravity is ignored, and thus the terms of the left-hand side in Eq. (2-1) represents the total derivative of f with the respect to time t , or $\frac{df}{dt} = \frac{\partial f}{\partial t} + \boldsymbol{\xi} \cdot \nabla f$. Macroscopic variables like the density ρ and the fluid velocity \mathbf{u} can be determined from the distribution function $f(\mathbf{x}, \boldsymbol{\xi}, t)$. For instance, based on the definition of f , the fluid density ρ can be defined as follow

$$\rho(\mathbf{x}, t) = \int f(\mathbf{x}, \boldsymbol{\xi}, t) d\boldsymbol{\xi}. \quad (2-2)$$

By integrating over velocity space in this way, we are considering the contribution to the density of particles of all possible velocities at position \mathbf{x} and time t . Similarly, through momentum and energy conservations, fluid velocity \mathbf{u} and internal energy E can be found as follow

$$\rho(\mathbf{x}, t) \mathbf{u}(\mathbf{x}, t) = \int \boldsymbol{\xi} f(\mathbf{x}, \boldsymbol{\xi}, t) d\boldsymbol{\xi}, \quad (2-3)$$

$$\rho(\mathbf{x}, t) E(\mathbf{x}, t) = \frac{1}{2} \int K^2 f(\mathbf{x}, \boldsymbol{\xi}, t) d\boldsymbol{\xi}, \quad (2-4)$$

which are weighted averages through f . Here, K is the magnitude of the particular velocity (relative velocity) $K = \xi - \mathbf{u}$, which is the deviation of the particle velocity from the fluid velocity.

Boltzmann's original collision operator Ω in Eq. (2-1) is a complex and cumbersome quadratic integral function of f (Huang, 1963; Wolf-Gladrow, 2000). It is often replaced by simpler expressions aimed at relinquishing most of the mathematical difficulty and keeping the basic physical principle, including conservation laws and the H -theorem proved by Boltzmann in 1872 (Wolf-Gladrow, 2000). The most widely known one for recovering NS equations is the BGK (Bhatnagar *et al.*, 1954) model, or

$$\Omega_{BGK} = -\frac{1}{\tau_0}(f - f^{eq}), \quad (2-5)$$

which is proposed by Bhatnagar, Gross and Krook. Here, τ_0 is the relaxation time related to viscosity, as we will show later in Section 2.2. f^{eq} is the equilibrium distribution function

$$f^{eq}(\mathbf{x}, \xi, t) = A \exp\left[\frac{(\xi - \mathbf{u}) \cdot (\xi - \mathbf{u})}{B}\right]. \quad (2-6)$$

A and B are generic constants. They should be constrained by the requirement of Eqs. (2-2) – (2-4). When

$$A = \frac{\rho}{(2\pi RT)^{d/2}} \quad (2-7)$$

and

$$B = -2RT, \quad (2-8)$$

Eq. (2-6) can become the Maxwell distribution function (Maxwell, 1867; Huang, 1963). $R = \frac{k_B}{M}$ is the gas constant with the Boltzmann constant k_B and the molecular mass M , T is the temperature and d is the number of spatial dimensions.

According to Eqs. (2-1), (2-5) and (2-6), the BGK Boltzmann equation can be obtained

$$\frac{\partial f(\mathbf{x}, \xi, t)}{\partial t} + \xi \cdot \nabla f(\mathbf{x}, \xi, t) = -\frac{1}{\tau_0}[f(\mathbf{x}, \xi, t) - f^{eq}(\mathbf{x}, \xi, t)]. \quad (2-9)$$

Now we will show how to get LBE from the continuous Boltzmann equation in Eq. (2-9). The first step is to discretize the velocity space of ξ into a finite set of velocities $\{\mathbf{e}_i\}$ without affecting the conservation laws. The Maxwell distribution function f^{eq} is expanded into a Taylor series in term of the fluid velocity

$$f^{eq} = A \exp\left(\frac{\xi \cdot \mathbf{u}}{B}\right) \left[1 - \frac{2\xi \cdot \mathbf{u}}{B} + \frac{2(\xi \cdot \mathbf{u})^2}{B^2} + \frac{\mathbf{u} \cdot \mathbf{u}}{B}\right]. \quad (2-10)$$

Here, the term of $O\left[\left(\frac{u}{\sqrt{-B}}\right)^3\right]$ has been neglected. It should be noticed that this expansion can only be used for low Mach number flow, or $\frac{u}{\sqrt{-B}} \ll 1$. The discrete velocity set should be chosen so that the following quadrature of the expanded Maxwell distribution function holds

$$\int \xi^k f^{eq} d\xi = \sum_i w_i \mathbf{e}_i^k f^{eq}(\mathbf{e}_i), \quad 0 \leq k \leq 2 \quad (2-11)$$

where w_i is the weight of the numerical quadrature rule. Then, we can define a discrete distribution function, $f_i(\mathbf{x}, t) = w_i f(\mathbf{x}, \mathbf{e}_i, t)$, which satisfies the following equation

$$\frac{\partial f_i}{\partial t} + \mathbf{e}_i \cdot \nabla f_i = -\frac{1}{\tau_0} (f_i - f_i^{eq}), \quad (2-12)$$

where $f_i^{eq}(\mathbf{x}, t) = w_i f^{eq}(\mathbf{x}, \mathbf{e}_i, t)$ is the discrete equilibrium distribution function. The terms of the left-hand side in Eq. (2-12) represents the total derivative of f with the respect to time t , or $\frac{df_i}{dt} = \frac{\partial f_i}{\partial t} + \mathbf{e}_i \cdot \nabla f_i$. The fluid density and velocity can be obtained from the discrete distribution function, or

$$\rho(\mathbf{x}, t) = \sum_i f_i(\mathbf{x}, t), \quad (2-13)$$

$$\rho(\mathbf{x}, t) \mathbf{u}(\mathbf{x}, t) = \sum_i f_i(\mathbf{x}, t) \mathbf{e}_i. \quad (2-14)$$

Using forward difference method to calculate the derivative on the left-hand side of Eq. (2-12), we can have

$$f_i(\mathbf{x} + \mathbf{e}_i \delta_t, t + \delta_t) - f_i(\mathbf{x}, t) = -\frac{1}{\tau} [f_i(\mathbf{x}, t) - f_i^{eq}(\mathbf{x}, t)], \quad (2-15)$$

which is known as lattice Boltzmann equation or lattice BGK equation (Chen and Doolen, 1998). Here, $\tau = \frac{\tau_0}{\delta_t}$ is the nondimensionalized relaxation time and δ_t is the time step.

A set of LBM models are usually known by $DdQq$, which is proposed by [Qian et al. \(1992\)](#). The first part (Dd) of $DdQq$ refers to the dimensionality and its second part (Qq) refers to the number of discrete velocities. In $DdQq$, the discrete equilibrium distribution function can be expressed as

$$f_i^{eq}(\mathbf{x}, t) = \rho \omega_i \left[1 + \frac{\mathbf{e}_i \cdot \mathbf{u}}{c_s^2} + \frac{(\mathbf{e}_i \cdot \mathbf{u})^2}{2c_s^4} - \frac{\mathbf{u} \cdot \mathbf{u}}{2c_s^2} \right], \quad (2-16)$$

where $\omega_i = \frac{A \omega_i}{\rho} \exp\left(\frac{\xi \cdot \xi}{B}\right)$ is the weighting coefficient associated with the discrete velocity \mathbf{e}_i . c_s is used instead of B in Eq. (2-10), or $c_s^2 = RT$. In the isothermal LBM, c_s determines the relation $p = \rho RT = \rho c_s^2$ between the pressure p and density ρ , and thus it can represent the equivalent sound speed in $DdQq$ models. In such a case, the Mach number is defined as $M_a = \frac{u}{c_s}$. It should be noted that Eq. (2-16) retains the terms up to $O\left(\frac{u^2}{c_s^2}\right)$ (or $O(M_a^2)$). The equilibrium distribution function should satisfy the following constraints ([Aidun and Clausen, 2010](#)):

$$\sum_i f_i^{eq} = \rho, \quad (2-17)$$

$$\sum_i f_i^{eq} \mathbf{e}_i = \rho \mathbf{u}, \quad (2-18)$$

and it has the following properties ([Aidun and Clausen, 2010](#))

$$\sum_i f_i^{eq} e_{i\alpha} e_{i\beta} = \rho u_\alpha u_\beta + \rho c_s^2 \delta_{\alpha\beta} = \rho u_\alpha u_\beta + p \delta_{\alpha\beta}, \quad (2-19)$$

$$\sum_i f_i^{eq} e_{i\alpha} e_{i\beta} e_{i\gamma} = \rho c_s^2 (u_\alpha \delta_{\beta\gamma} + u_\beta \delta_{\alpha\gamma} + u_\gamma \delta_{\alpha\beta}). \quad (2-20)$$

Here, A_α (or A_β , or A_γ) is the α -th (or β -th, or γ -th) element of a vector \mathbf{A} , which is also used in the rest part of the thesis. $\delta_{\alpha\beta}$ is the Kronecher delta function, or

$$\delta_{\alpha\beta} = \begin{cases} 1, & \alpha = \beta \\ 0, & \alpha \neq \beta \end{cases}.$$

The commonly used $DdQq$ models for simulating fluid flows are $D1Q3$, $D2Q9$ and $D3Q19$ ([Kruger et al., 2017](#)), whose corresponding velocity sets $\{\mathbf{e}_i\}$ at a node are depicted and numbered in Fig. 2-1. $D2Q9$ used in the following computations is quoted as an example of how to model the fluid flows by LBM and how to recover the NS equations from LBE. The

index $i = 0$: $\mathbf{e}_0 = \mathbf{0}$ shown in purple circles of Fig. 2-1 represents stationary particle. It should be noted that there are at least two conversions commonly used to describe the numbering of the velocities in a set $\{\mathbf{e}_i\}$: (1) the index i in $\{\mathbf{e}_i\}$ is chosen from 0 to $q-1$; (2) it from 1 to q . The former one is used in Fig. 2-1. In such a case, $\{\mathbf{e}_i\}$ of D2Q9 shown in Fig. 2-1(b) can be written as

$$\mathbf{e}_i = \begin{cases} (0,0) & i = 0 \\ c(\cos[(i-1)\pi/2], \sin[(i-1)\pi/2]) & i = 1-4, \\ \sqrt{2}c(\cos[(2i-1)\pi/4], \sin[(2i-1)\pi/4]) & i = 5-8 \end{cases} \quad (2-21)$$

where c is the lattice speed. The particle distribution functions f_i are assumed to move with the corresponding discrete velocities \mathbf{e}_i from one lattice node to another, except f_0 with $\mathbf{e}_0 = \mathbf{0}$ resting on its own node. It means that after one time step δ_t , each f_i ($i = 1-8$) should exactly reach a neighbouring node. In order to guarantee this, $c = \delta_x/\delta_t = \delta_y/\delta_t$, where δ_x and δ_y are the lattice spacing shown in Fig. 2-2. Without loss of generality, $l = \delta_x = \delta_y$ and δ_t are assumed to be 1, and thus $c = 1$. In the continuous form, A and B in Eq. (2-6) are constrained by Eqs. (2-2) – (2-4). In the discrete form, Eqs. (2-16) – (2-21) can give the values of a set of $\{\omega_i\}$ and c_s , and for D2Q9 they can be obtained, or $\omega_0 = 4/9$, $\omega_i = 1/9$ for $i = 1-4$, $\omega_i = 1/36$ for $i = 5-8$ and $c_s = c/\sqrt{3}$.

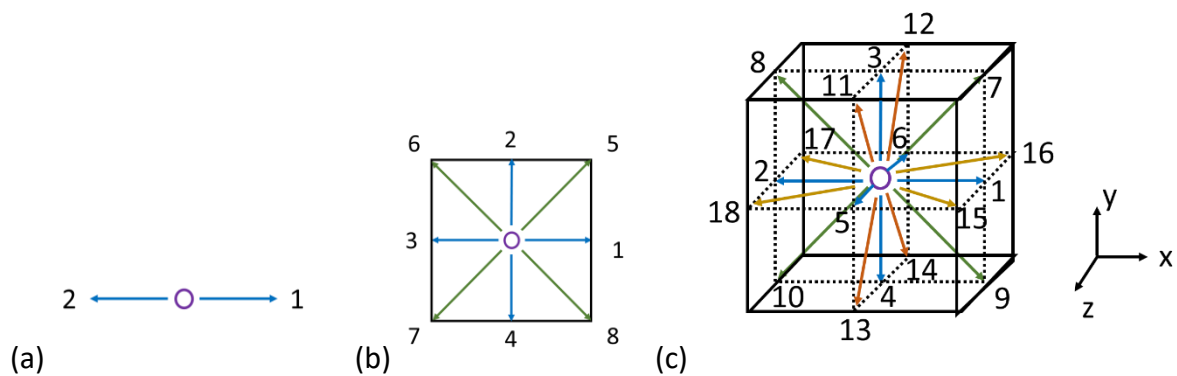


Fig. 2-1 DdQq models: (a) D1Q3; (b) D2Q9; (c) D3Q19. Velocities with length $|\mathbf{e}_i| = c, \sqrt{2}c$ in blue and other colours, respectively.

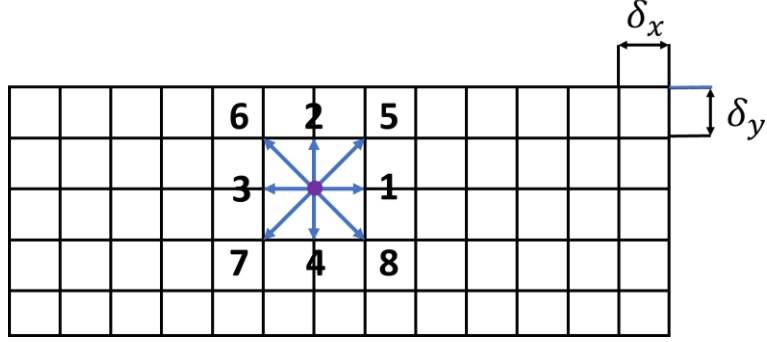


Fig. 2-2 Lattice and discrete velocities of the D2Q9 model.

During simulation process, Eq. (2-15) generally can be divided into two parts (Kruger et al., 2017): (1) collision which is a purely local and algebraic operation, or

$$f_i^*(\mathbf{x}, t) = f_i(\mathbf{x}, t) - \frac{1}{\tau} [f_i(\mathbf{x}, t) - f_i^{eq}(\mathbf{x}, t)], \quad (2-22)$$

where f_i^* is the density distribution function after collision process; (2) streaming in which f_0 with $\mathbf{e}_0 = \mathbf{0}$ is not changed and other f_i^* moves to the neighbouring node in the direction of its velocity \mathbf{e}_i , or

$$f_i(\mathbf{x} + \mathbf{e}_i \delta_t, t + \delta_t) = f_i^*(\mathbf{x}, t). \quad (2-23)$$

The detailed calculation process of D2Q9 is as follow:

(1) Compute the equilibrium distribution function $f_i^{eq}(\mathbf{x}, t)$ at the time $t = 0$ based on Eq. (2-16) with the given fluid velocity $\mathbf{u}(\mathbf{x}, t)$ and the given fluid density $\rho(\mathbf{x}, t)$. And set the initial particle distribution function $f_i(\mathbf{x}, t) = f_i^{eq}(\mathbf{x}, t)$.

(2) Calculate $f_i^*(\mathbf{x}, t)$ based on Eq. (2-22).

(3) Calculate $f_i(\mathbf{x} + \mathbf{e}_i \delta_t, t + \delta_t)$ based on Eq. (2-23).

(4) Update the fluid density $\rho(\mathbf{x}, t + \delta_t)$ based on Eq. (2-13) or $\rho(\mathbf{x}, t + \delta_t) = \sum_{i=0}^8 f_i(\mathbf{x}, t + \delta_t)$. Likewise, update velocity $\mathbf{u}(\mathbf{x}, t + \delta_t)$ based on Eq. (2-14) or $\rho(\mathbf{x}, t + \delta_t) \mathbf{u}(\mathbf{x}, t + \delta_t) = \sum_{i=0}^8 f_i(\mathbf{x}, t + \delta_t) \mathbf{e}_i$, and $f_i^{eq}(\mathbf{x}, t + \delta_t)$ based on Eq. (2-16).

(5) Return to Step (2) and start next time $(t + \delta_t) + \delta_t$.

2.2 Recovery of Navier-Stokes Equations from Lattice Boltzmann Equation

In order to show that LBE can actually be used to simulate the behaviour of fluid flows, this section is to show the equivalence between LBE and NS equations using Chapman-Enskog expansion (Cercignani, 1988), a multi-scale method, which is named after Sydney Chapman and David Enskog, two mathematical physicists from Britain and Sweden, respectively.

The distribution function f_i is expanded around the equilibrium distribution function f_i^{eq} , or

$$f_i = f_i^{eq} + \epsilon f_i^1 + \epsilon^2 f_i^2 + O(\epsilon^3). \quad (2-24)$$

Here, the assumption is that the deviation from the equilibrium distribution function f_i^{eq} is of a small order ϵ . Up to the second order, the multi-scale expansion of temporal and spatial derivatives in ϵ can be written as

$$\frac{\partial}{\partial t} = \epsilon \frac{\partial}{\partial t_1} + \epsilon^2 \frac{\partial}{\partial t_2}, \quad (2-25)$$

$$\nabla = \epsilon \nabla^1 + \epsilon^2 \nabla^2 \text{ (or } \frac{\partial}{\partial x} = \epsilon \frac{\partial}{\partial x^1} + \epsilon^2 \frac{\partial}{\partial x^2}). \quad (2-26)$$

Through Taylor expansion with respect to δ_t , we rewrite LBE in Eq. (2-15) accurate to second order in δ_t

$$\left(\frac{\partial}{\partial t} + \mathbf{e}_i \cdot \nabla \right) f_i(\mathbf{x}, t) + \frac{\delta_t}{2} \left(\frac{\partial}{\partial t} + \mathbf{e}_i \cdot \nabla \right)^2 f_i(\mathbf{x}, t) = -\frac{1}{\tau_0} [f_i(\mathbf{x}, t) - f_i^{eq}(\mathbf{x}, t)]. \quad (2-27)$$

Here, δ_t is also treated as the same order of ϵ . Substituting Eqs. (2-24) - (2-26) into Eq. (2-27) and using some algebra, we have the following equations

$$\left(\frac{\partial}{\partial t_1} + \mathbf{e}_i \cdot \nabla^1 \right) f_i^{eq} = -\frac{1}{\tau_0} f_i^1 \quad (2-28)$$

to order ϵ^1 and

$$\left(\frac{\partial}{\partial t_2} + \mathbf{e}_i \cdot \nabla^2 \right) f_i^{eq} + \left(\frac{\partial}{\partial t_1} + \mathbf{e}_i \cdot \nabla^1 \right) \left(1 - \frac{1}{2\tau} \right) f_i^1 = -\frac{1}{\tau_0} f_i^2 \quad (2-29)$$

to order ϵ^2 . According to Eqs. (2-13) - (2-14) and (2-17) - (2-18), f_i^k ($k = 1, 2$) should satisfy the following constraints:

$$\sum_i f_i^k = 0, \quad \sum_i \mathbf{e}_i f_i^k = 0. \quad (2-30)$$

The continuity equation to order ϵ^1 is obtained by summing Eq. (2-28) with respect to i and using Eqs. (2-17), (2-18) and (2-30)

$$\frac{\partial \rho}{\partial t_1} + \nabla^1 \cdot (\rho \mathbf{u}) = 0, \quad (2-31)$$

and the momentum equation to order ϵ^1 is obtained by multiplying Eq. (2-29) by \mathbf{e}_i first, then summing it with respect to i and using Eqs. (2-18), (2-19) and (2-30)

$$\frac{\partial \rho u_\alpha}{\partial t_1} + \frac{\partial}{\partial x_\beta^1} (\rho u_\alpha u_\beta) = -\frac{\partial p}{\partial x_\alpha^1}, \quad (2-32)$$

where the summation with respect to β is implied. Similarly, the continuity equation to order ϵ^2 is obtained by summing Eq. (2-29) with respect to i and using Eqs. (2-17) and (2-30)

$$\frac{\partial \rho}{\partial t_2} + \nabla^2 \cdot (\rho \mathbf{u}) = 0, \quad (2-33)$$

and the momentum equation to order ϵ^2 is obtained by multiplying Eq. (2-29) by \mathbf{e}_i first, then summing it with respect to i and using Eqs. (2-18) and (2-30)

$$\frac{\partial \rho u_\alpha}{\partial t_2} + \frac{\partial}{\partial x_\beta^2} (\rho u_\alpha u_\beta) + \left(1 - \frac{1}{2\tau}\right) \frac{\partial}{\partial x_\beta^1} (\sum_i e_{i\alpha} e_{i\beta} f_i^1) = -\frac{\partial p}{\partial x_\alpha^2}, \quad (2-34)$$

where the summation with respect to β is implied. The momentum flux tensor $Q_{\alpha\beta}$ is

$$Q_{\alpha\beta} = \sum_i e_{i\alpha} e_{i\beta} f_i^1. \quad (2-35)$$

Substituting Eq. (2-28) to Eq. (2-35), we have

$$Q_{\alpha\beta} = -\tau_0 \left[\frac{\partial}{\partial t_1} (\sum_i e_{i\alpha} e_{i\beta} f_i^{eq}) + \frac{\partial}{\partial x_\gamma^1} (\sum_i e_{i\alpha} e_{i\beta} e_{i\gamma} f_i^{eq}) \right]. \quad (2-36)$$

Inserting Eqs. (2-19) and (2-20) into Eq. (2-36), the following equation can be found

$$Q_{\alpha\beta} = -\tau_0 \left\{ \frac{\partial}{\partial t_1} (\rho u_\alpha u_\beta + \rho c_s^2 \delta_{\alpha\beta}) + \frac{\partial}{\partial x_\gamma^1} [\rho c_s^2 (u_\alpha \delta_{\beta\gamma} + u_\beta \delta_{\alpha\gamma} + u_\gamma \delta_{\alpha\beta})] \right\}. \quad (2-37)$$

Since

$$\frac{\partial}{\partial t_1} (\rho u_\alpha u_\beta + \rho c_s^2 \delta_{\alpha\beta}) = u_\alpha \frac{\partial \rho u_\beta}{\partial t_1} + u_\beta \frac{\partial \rho u_\alpha}{\partial t_1} - u_\alpha u_\beta \frac{\partial \rho}{\partial t_1} + c_s^2 \frac{\partial \rho}{\partial t_1} \delta_{\alpha\beta}, \quad (2-38)$$

using Eqs. (2-31) – (2-32), Eq. (2-38), we have

$$\begin{aligned} \frac{\partial}{\partial t_1} (\rho u_\alpha u_\beta + \rho c_s^2 \delta_{\alpha\beta}) &= -u_\alpha c_s^2 \frac{\partial \rho}{\partial x_\beta^1} - u_\beta c_s^2 \frac{\partial \rho}{\partial x_\alpha^1} - u_\alpha \frac{\partial \rho u_\beta u_\gamma}{\partial x_\gamma^1} - u_\beta \frac{\partial \rho u_\alpha u_\gamma}{\partial x_\gamma^1} + u_\alpha u_\beta \frac{\partial \rho u_\gamma}{\partial x_\gamma^1} - \\ &c_s^2 \frac{\partial \rho u_\gamma}{\partial x_\gamma^1} \delta_{\alpha\beta} = -u_\alpha c_s^2 \frac{\partial \rho}{\partial x_\beta^1} - u_\beta c_s^2 \frac{\partial \rho}{\partial x_\alpha^1} - \frac{\partial}{\partial x_\gamma^1} (\rho u_\alpha u_\beta u_\gamma) - c_s^2 \frac{\partial \rho u_\gamma}{\partial x_\gamma^1} \delta_{\alpha\beta}. \end{aligned} \quad (2-39)$$

The last term in Eq. (2-37) can be rewritten as

$$\begin{aligned} \frac{\partial}{\partial x_\gamma^1} [\rho c_s^2 (u_\alpha \delta_{\beta\gamma} + u_\beta \delta_{\alpha\gamma} + u_\gamma \delta_{\alpha\beta})] &= c_s^2 \frac{\partial \rho u_\gamma}{\partial x_\gamma^1} \delta_{\alpha\beta} + c_s^2 \frac{\partial \rho u_\beta}{\partial x_\alpha^1} + c_s^2 \frac{\partial \rho u_\alpha}{\partial x_\beta^1} \\ &= c_s^2 \frac{\partial \rho u_\gamma}{\partial x_\gamma^1} \delta_{\alpha\beta} + \rho c_s^2 \left(\frac{\partial u_\alpha}{\partial x_\beta^1} + \frac{\partial u_\beta}{\partial x_\alpha^1} \right) + c_s^2 u_\alpha \frac{\partial \rho}{\partial x_\beta^1} + c_s^2 u_\beta \frac{\partial \rho}{\partial x_\alpha^1}. \end{aligned} \quad (2-40)$$

Substituting Eqs. (2-37) – (2-40) to Eq. (2-36), we have

$$Q_{\alpha\beta} = -\tau_0 \left[\rho c_s^2 \left(\frac{\partial u_\alpha}{\partial x_\beta^1} + \frac{\partial u_\beta}{\partial x_\alpha^1} \right) - \frac{\partial}{\partial x_\gamma^1} (\rho u_\alpha u_\beta u_\gamma) \right].$$

Here as in [Qian and Orszag \(1993\)](#), $\frac{\partial \rho \bar{u}_\alpha \bar{u}_\beta \bar{u}_\gamma}{\partial x_\gamma^1} / \left[\rho c_s^2 \left(\frac{\partial u_\alpha}{\partial x_\beta^1} + \frac{\partial u_\beta}{\partial x_\alpha^1} \right) \right] \approx O(M_a^2)$, and thus if $M_a^2 \ll$

1, the second term in the above equation can be neglected. We have

$$Q_{\alpha\beta} = -\tau_0 \rho c_s^2 \left(\frac{\partial u_\alpha}{\partial x_\beta^1} + \frac{\partial u_\beta}{\partial x_\alpha^1} \right). \quad (2-41)$$

Combing the mass conservation equations on both the ϵ^1 and ϵ^2 scales from Eqs. (2-31) and (2-33), we can have

$$\epsilon^1 \frac{\partial \rho}{\partial t_1} + \epsilon^2 \frac{\partial \rho}{\partial t_2} + \epsilon^1 \nabla^1 \cdot (\rho \mathbf{u}) + \epsilon^2 \nabla^2 \cdot (\rho \mathbf{u}) + O(\epsilon^3) = 0. \quad (2-42)$$

Likewise, combining the momentum conservation equations on both the ϵ^1 and ϵ^2 scales based on Eqs. (2-32), (2-34) – (2-41), we have

$$\begin{aligned} \epsilon^1 \frac{\partial \rho u_\alpha}{\partial t_1} + \epsilon^2 \frac{\partial \rho u_\alpha}{\partial t_2} + \epsilon^1 \frac{\partial}{\partial x_\beta^1} (\rho u_\alpha u_\beta) + \epsilon^2 \frac{\partial}{\partial x_\beta^2} (\rho u_\alpha u_\beta) + \epsilon^1 \frac{\partial p}{\partial x_\alpha^1} + \epsilon^2 \frac{\partial p}{\partial x_\alpha^2} - \epsilon^1 \frac{\partial}{\partial x_\beta^1} \left[\left(\tau - \right. \right. \\ \left. \left. \frac{1}{2} \right) c_s^2 \delta_{t\rho} \left(\frac{\partial u_\alpha}{\partial x_\beta^1} + \frac{\partial u_\beta}{\partial x_\alpha^1} \right) \right] + O(\epsilon^3) = 0. \end{aligned}$$

Adding $-\epsilon^2 \frac{\partial}{\partial x_\beta^2} \left[\left(\tau - \frac{1}{2} \right) c_s^2 \delta_{t\rho} \left(\frac{\partial u_\alpha}{\partial x_\beta^2} + \frac{\partial u_\beta}{\partial x_\alpha^2} \right) \right]$ into the left side of the above equation, which has the order of $O(\epsilon^3)$, and thus does not affect the order, we have

$$\begin{aligned} \epsilon^1 \frac{\partial \rho u_\alpha}{\partial t_1} + \epsilon^2 \frac{\partial \rho u_\alpha}{\partial t_2} + \epsilon^1 \frac{\partial}{\partial x_\beta^1} (\rho u_\alpha u_\beta) + \epsilon^2 \frac{\partial}{\partial x_\beta^2} (\rho u_\alpha u_\beta) + \epsilon^1 \frac{\partial p}{\partial x_\alpha^1} + \epsilon^2 \frac{\partial p}{\partial x_\alpha^2} - \epsilon^1 \frac{\partial}{\partial x_\beta^1} \left[\left(\tau - \right. \right. \\ \left. \left. \frac{1}{2} \right) c_s^2 \delta_t \rho \left(\frac{\partial u_\alpha}{\partial x_\beta^1} + \frac{\partial u_\beta}{\partial x_\alpha^1} \right) \right] - \epsilon^2 \frac{\partial}{\partial x_\beta^2} \left[\left(\tau - \frac{1}{2} \right) c_s^2 \delta_t \rho \left(\frac{\partial u_\alpha}{\partial x_\beta^2} + \frac{\partial u_\beta}{\partial x_\alpha^2} \right) \right] + O(\epsilon^3) = 0. \end{aligned} \quad (2-43)$$

According to Eqs. (2-25) – (2-26) and Eqs. (2-42) – (2-43), we can have the following hydrodynamic equations

$$\frac{\partial \rho}{\partial t} + \nabla \cdot (\rho \mathbf{u}) = 0. \quad (2-44)$$

$$\frac{\partial \rho \mathbf{u}}{\partial t} + \nabla \cdot (\rho \mathbf{u} \mathbf{u}) = -\nabla p + \nabla \cdot [\rho \nu (\nabla \mathbf{u} + (\nabla \mathbf{u})^T)]. \quad (2-45)$$

Here, ν is the kinematic viscosity given by

$$\nu = (\tau - 0.5) c_s^2 \delta_t, \quad (2-46)$$

It should be noted that Eqs. (2-44) and (2-45) are the form for compressible fluid, with the artificial sound speed c_s in $p = \rho c_s^2$. However, for the equivalence of LBE and NS equations, the Mach number M_a has to be assumed to be small and the order of accuracy is $O(M_a^2)$. In such a case, Eqs. (2-44) and (2-45) can be seen as an approximation for the NS equations of incompressible fluid below.

$$\nabla \cdot \mathbf{u} = 0, \quad (2-47)$$

$$\frac{\partial \mathbf{u}}{\partial t} + (\mathbf{u} \cdot \nabla) \mathbf{u} = -\frac{\nabla p}{\rho} + \nu \nabla^2 \mathbf{u}. \quad (2-48)$$

2.3 Immersed Boundary Method

In general, for simulation of fluid flows, the solution of governing equations is strongly coupled with the implementation of boundary conditions. Due to this feature, when the flow past a moving body, such as in free or forced vibrations, is considered, the computation often involves tedious grid generation and complicated solution process. To ease the computational process, it is desirable to develop an approach which can decouple the solution of governing equations and the implementation of boundary conditions. The IBM is such an approach. It was initially proposed by [Peskin \(1977\)](#) for simulation of blood flows in the heart. This scheme uses fixed Eulerian grids for the flow field and a set of Lagrangian points to represent the solid

boundary, shown in Fig. 2-3. Feng and Michaelides (2004) combined LBM with IBM first and then verified its accuracy by simulating the motion of bodies immersed in the fluid. This section will describe the procedure of immersed boundary method for satisfying no-slip condition, or

$$\mathbf{u} = \mathbf{U}^d, \quad (2-49)$$

where \mathbf{U}^d is the velocity of the body surface.

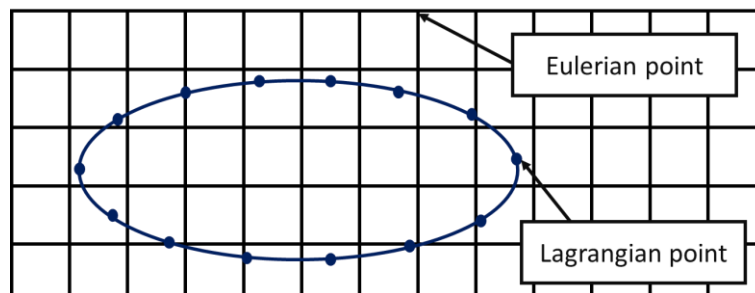


Fig. 2-3 Immersed boundary illustration.

The idea of IBM is to replace the body surface with a layer of distributed force \mathbf{g} whose value is determined by the no-slip condition. Based on this principle, Eq. (2-48) can be rewritten as

$$\frac{\partial \mathbf{u}}{\partial t} + (\mathbf{u} \cdot \nabla) \mathbf{u} = -\frac{\nabla p}{\rho} + \nu \nabla^2 \mathbf{u} + \mathbf{g}. \quad (2-50)$$

From Eq. (2-48), the updated velocity \mathbf{u}^* without the forcing term can be obtained from

$$\frac{\partial \mathbf{u}}{\partial t} = \frac{\mathbf{u}^*(x, t + \delta_t) - \mathbf{u}(x, t)}{\delta_t} = -(\mathbf{u} \cdot \nabla) \mathbf{u} - \frac{\nabla p}{\rho} + \nu \nabla^2 \mathbf{u} = RS. \quad (2-51)$$

Likewise, from Eq. (2-50), we have

$$\frac{\mathbf{u}^d(x, t + \delta_t) - \mathbf{u}(x, t)}{\delta_t} = RS + \mathbf{g}(x, t), \quad (2-52)$$

where \mathbf{u}^d is the desired fluid velocity. According to Eqs. (2-51) – (2-52), the external force should be obtained from

$$\mathbf{g}(x, t) = \frac{\mathbf{u}^d(x, t + \delta_t) - \mathbf{u}^*(x, t + \delta_t)}{\delta_t}. \quad (2-53)$$

Obviously, \mathbf{g} cannot be applied in Eq. (2-50) everywhere as the equation has to be equivalent to Eq. (2-48) in the fluid domain. The forcing term should be applied only to a strip along the body surface $\mathbf{X}(s, t)$, including the pressure and shear force. As velocity is given on each lattice node, the velocity $\mathbf{U}^*(s, t)$ on the boundary without the forcing term can be obtained by the delta function δ_l

$$\mathbf{U}^*(s, t) = \sum_x \mathbf{u}^*(\mathbf{x}, t) \delta_l(\mathbf{x} - \mathbf{X}(s, t)) \delta_x \delta_y, \quad (2-54)$$

which is the discretized form of the integration involving Dirac delta function. Based on [Peskin \(2002\)](#), the delta function $\delta_l(\mathbf{x})$ can be written as follow

$$\delta_l(\mathbf{x}) = \delta_l(x) \delta_l(y), \quad (2-55)$$

and

$$\delta_l(r) = \begin{cases} \frac{1}{4l} \left[1 + \cos\left(\frac{\pi|r|}{2}\right) \right] & |r| \leq 2l \\ 0 & \text{otherwise} \end{cases}. \quad (2-56)$$

The desired velocity \mathbf{u}^d on the body surface should be body surface velocity \mathbf{U}^d . Thus, the required body force on the solid boundary should be

$$\mathbf{G}(s, t) = \frac{\mathbf{U}^d(s, t) - \mathbf{U}^*(s, t)}{\delta_t}, \quad (2-57)$$

Corresponding to that the external force in the strip next to the body surface should be obtained from

$$\mathbf{g}(\mathbf{x}, t) = \sum_s \mathbf{G}(s, t) \delta_l(\mathbf{x} - \mathbf{X}(s, t)) \delta_s, \quad (2-58)$$

where δ_s is the arc length of the boundary element.

The body force \mathbf{g} can be straightforwardly as a forcing term g_i to add into LBE in Eq. (2-15) ([Frisch et al., 1987](#); [Luo, 1997](#)), or

$$f_i(\mathbf{x} + \mathbf{e}_i \delta_t, t + \delta_t) = f_i(\mathbf{x}, t) - \frac{1}{\tau} [f_i(\mathbf{x}, t) - f_i^{eq}(\mathbf{x}, t)] + \delta_t g_i. \quad (2-59)$$

The forcing term g_i in Eq. (2-59) can be written as ([Frisch et al., 1987](#); [Luo, 1997](#))

$$g_i = \frac{\omega_i \rho}{c_s^2} \mathbf{e}_i \cdot \mathbf{g}, \quad (2-60)$$

which is constructed to enforce mass and momentum conversations, or

$$\sum_i g_i = 0, \quad \sum_i \mathbf{e}_i g_i = \rho \mathbf{g}. \quad (2-61)$$

The fluid force on a cylinder can be calculated by integrating the external force $\mathbf{g}(\mathbf{x}, t) = (g_x(\mathbf{x}, t), g_y(\mathbf{x}, t))$ over the whole fluid domain. The drag and lift forces are given by

$$F_D = \iint g_x(\vec{x}, t) dx dy \quad (2-62)$$

and

$$F_L = \iint g_y(\vec{x}, t) dx dy. \quad (2-63)$$

In reality, this integration needs to be performed only over the layer next the body surface because of the delta function in Eq. (2-58). The corresponding coefficients are defined by

$$C_D = F_D / 0.5 \rho u_0^2 D, \quad C_L = F_L / 0.5 \rho u_0^2 D. \quad (2-64)$$

To solve the research questions of this thesis, an in-house code based on D2Q9 model together with immersed boundary method written is developed in *Fortran* and used for the numerical simulations. The main calculation process is summarized as follow.

- (1) Calculate $f_i(\mathbf{x} + \mathbf{e}_i \delta_t, t + \delta_t)$ without forcing term by $f_i(\mathbf{x}, t)$ based on Eq. (2-15).
- (2) Calculate the fluid velocity $\mathbf{u}^*(\mathbf{x}, t + \delta_t)$ without the forcing term based on Eq. (2-14).
- (3) Calculate $\mathbf{U}^*(s, t + \delta_t)$ based on Eq. (2-54).
- (4) Calculate $\mathbf{G}(s, t + \delta_t)$ based on Eq. (2-57).
- (5) Calculate $\mathbf{g}(\mathbf{x}, t + \delta_t)$ based on (2-58).
- (6) Update $f_i(\mathbf{x}, t + \delta_t)$ according to $f_i(\mathbf{x}, t + \delta_t) = f_i(\mathbf{x}, t + \delta_t) + \delta_t g_i(\mathbf{x}, t + \delta_t)$, where $g_i(\mathbf{x}, t + \delta_t)$ can be obtained based on Eq. (2-60).
- (7) Update the fluid density $\rho(\mathbf{x}, t + \delta_t)$ and velocity $\mathbf{u}(\mathbf{x}, t + \delta_t)$ by the updated $f_i(\mathbf{x}, t + \delta_t)$ based on Eq. (2-13) and Eq. (2-14), respectively. And based on Eq. (2-16), update $f_i^{eq}(\mathbf{x}, t + \delta_t)$ for the next time step.
- (8) Return to Step (1) and start next time $(t + \delta_t) + \delta_t$.

It should be noted that in this in-house code, OpenMP, which is a library supporting shared-memory multiprocessing in *Fortran* is called for parallel programming to improve computational efficiency. The maximum of the number of threads is 32. In addition, in order to investigate the turbulent flows in Chapter 5, large eddy simulation regarded as turbulence model, discussed in Section 2.4, is also inserted into IB-LBM code.

2.4 Turbulence Model

Simulation of turbulent flows is one of the most challenging topics in physics and engineering. Direct numerical simulation (DNS) means to solve the NS equations without any turbulence models. However, the computational costs of DNS are prohibitive for high Reynolds number turbulence flows, because the resolution of the computational mesh in DNS must be high enough to capture the whole range of spatial and temporal scales of the turbulence. Unlike DNS, LES solves only the large scale flows by filtering the small scales in the NS equations with a spatial filter, and the unresolved Reynolds stress due to small scales dynamics is modelled using certain sub-grid scale (SGS) model. LBM has been demonstrated as a viable and effective approach for large-eddy simulations of turbulent flows (Hou *et al.*, 1996; Chen *et al.*, 2003; Dong *et al.*, 2008).

The turbulent flow of viscous, incompressible and Newtonian fluid is governed by the following filtered continuity equation and NS equation based on SGS model,

$$\nabla \cdot \bar{\mathbf{u}} = 0, \quad (2-65)$$

$$\frac{\partial \bar{\mathbf{u}}}{\partial t} + (\bar{\mathbf{u}} \cdot \nabla) \bar{\mathbf{u}} = -\frac{\nabla \bar{p}}{\rho} + 2\nu \nabla \cdot \mathbf{S} - \nabla \cdot \mathbf{T}, \quad (2-66)$$

where $\bar{\mathbf{u}}$ and \bar{p} are the filtered fluid velocity \mathbf{u} and pressure p , respectively. $\mathbf{S} = (\nabla \bar{\mathbf{u}} + (\nabla \bar{\mathbf{u}})^T)/2$ is the filtered strain rate tensor and \mathbf{T} is sub-grid-scale stresses due to interaction between the unsolved or SGS eddies defined as $\mathbf{T} = \overline{\mathbf{u}\mathbf{u}} - \bar{\mathbf{u}}\bar{\mathbf{u}}$. In SGS model due to Smagorinsky (1963), it is assumed

$$\mathbf{T} = -2\nu_e \mathbf{S} \quad (2-67)$$

and

$$\nu_e = (C\Delta)^2 \|\mathbf{S}\|, \quad (2-68)$$

where ν_e is the eddy viscosity, $\|\mathbf{S}\| = \sqrt{2|\sum_{\alpha,\beta} S_{\alpha\beta} S_{\alpha\beta}|}$, $S_{\alpha\beta} = \left(\frac{\partial \bar{u}_\alpha}{\partial x_\beta} + \frac{\partial \bar{u}_\beta}{\partial x_\alpha}\right)/2$, with $\alpha = 1,2$ and $\beta = 1,2$ corresponding to the lines and rows of \mathbf{S} , respectively. C is the Smagorinsky constant and Δ the filter width. Using this, Eq. (2-66) can be written as

$$\frac{\partial \bar{\mathbf{u}}}{\partial t} + (\bar{\mathbf{u}} \cdot \nabla) \bar{\mathbf{u}} = -\frac{\nabla \bar{p}}{\rho} + 2\nu_T \nabla \cdot \mathbf{S}, \quad (2-69)$$

where $\nu_T = \nu + \nu_e$ is the total viscosity. The Boltzmann equation to recover Eqs. (2-65) and (2-69) has the same formulation as that in Eq. (2-15). For simulation of turbulent flows, the relaxation time in Eq. (2-15) is modified by the turbulent relaxation time (Hou *et al.*, 1996)

$$\tau = \nu_T c_s^2 \delta_t + 0.5 = (\nu + \nu_e) c_s^2 \delta_t + 0.5. \quad (2-70)$$

To find $S_{\alpha\beta}$ required by the eddy viscosity in LES, there are at least two methods which could be conveniently used. The first one is to compute the velocity gradients using the finite-difference approximation, as square mesh is in the D2Q9 model. Another way is to evaluate it directly from the weighted density distribution function. In the present thesis, we have chosen the second method. In such a case, referring to Eqs. (2-24) and (2-35), the momentum flux tensor $Q_{\alpha\beta}$ can be written as

$$Q_{\alpha\beta} = \sum_i e_{i\alpha} e_{i\beta} (f_i - f_i^{eq}). \quad (2-71)$$

According to Eq. (2-41), we can have

$$Q_{\alpha\beta} = \tau \delta_t \rho c_s^2 \left(\frac{\partial \bar{u}_\alpha}{\partial x_\beta} + \frac{\partial \bar{u}_\beta}{\partial x_\alpha} \right) = -2\tau \delta_t \rho c_s^2 S_{\alpha\beta}, \quad (2-72)$$

and thus

$$\|\mathbf{S}\| = \frac{1}{2\tau \delta_t \rho c_s^2} \|\mathbf{Q}\|, \quad (2-73)$$

where $\|\mathbf{Q}\| = \sqrt{2|\sum_{\alpha,\beta} Q_{\alpha\beta} Q_{\alpha\beta}|}$ ($\alpha = 1,2$ and $\beta = 1,2$ correspond to the lines and rows of \mathbf{Q} , respectively.). Combining Eq. (2-73) with Eqs. (2-68) and (2-70) and eliminating τ , we have

$$\|\mathbf{S}\| = \frac{c_s^2}{2C^2\Delta^2} \left(\sqrt{a^2\delta_t^2 + 2C^2\Delta^2\rho^{-1}c_s^{-4}\|\mathbf{Q}\|} - a^2\delta_t \right) \quad (2-74)$$

and

$$\tau = \frac{1}{2} + \frac{1}{c_s^2\delta_t} \left[\nu + \frac{c_s^2}{2} \left(\sqrt{a^2\delta_t^2 + 2C^2\Delta^2\rho^{-1}c_s^{-4}\|\mathbf{Q}\|} - a^2\delta_t \right) \right], \quad (2-75)$$

where $a = \frac{1}{2} + \frac{1}{c_s^2\delta_t}\nu$. In practical applications, we can calculate $Q_{\alpha\beta}$ based on Eq. (2-71) first, then obtain its magnitude $\|\mathbf{Q}\|$ and finally compute the total relaxation time τ by Eq. (2-75).

2.5 Multi-Block Method in Lattice Boltzmann Method

The complexity level of the flow in different region is different. In order to improve the computational efficiency and accuracy of LES-LBM, the multi-block method (Peng *et al.*, 2006) is used for the simulation of turbulence flow. This allows us to use finer grid in a region where flow changes more rapidly. To illustrate the procedure, a two-block system, with a coarser block and a finer block shown in Fig. 2-4, is considered. δ_x and δ_y are the space steps in x and y directions, respectively, and δ_t is the time step. We have $\delta_x = \delta_y = c\delta_t$, where c is the lattice speed. The subscripts c and f indicate coarser and finer, respectively. The ratio of the space steps between coarser and finer blocks (or the ratio of their time steps) is $m_{cf} = \frac{\delta_{xc}}{\delta_{xf}} = \frac{\delta_{tc}}{\delta_{tf}}$. It should be noted that the kinematic viscosity ν is the same in the two blocks. In this sense, τ_{kc} and τ_{kf} should be linked by the equation $\nu = (\tau_{kc} - 0.5)c_s^2\delta_{tc} = (\tau_{kf} - 0.5)c_s^2\delta_{tf}$.

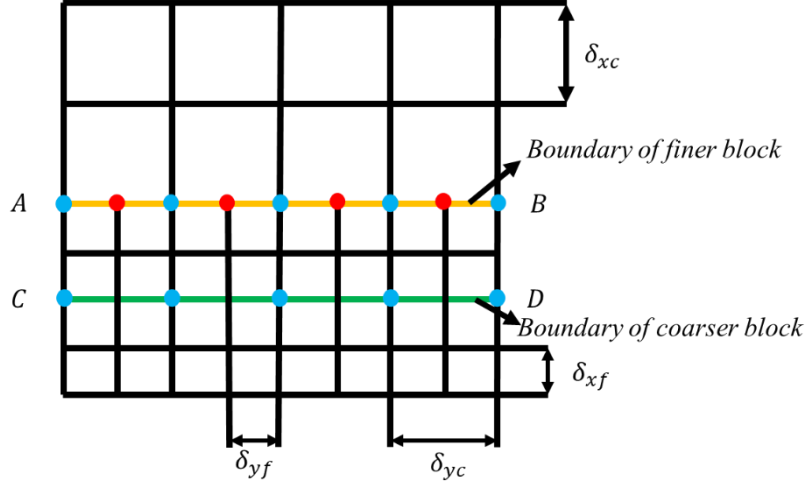


Fig. 2-4 Two blocks of different lattice spacing near their interface.

The information exchange between two blocks on the interface is through interpolation. A cubic spline is used to eliminate the possibility of spatial asymmetry (Yu et al., 2002) caused by interpolation,

$$h(x) = a_i + b_i x + c_i x^2 + d_i x^3, x_{i-1} \leq x \leq x_i \quad (i = 1, \dots, n) \quad (2-76)$$

where x_i are the blue nodes along AB of the coarser block. Here, $h_i = h(x_i)$ is known from the value of f in Eq. (2-15). The procedure to obtain coefficients a_i , b_i , c_i and d_i can be summarized as below.

(1) Approaching x_i within $x_{i-1} \leq x \leq x_i$, we can get the following equations

$$h_i = a_i + b_i x_i + c_i x_i^2 + d_i x_i^3, \quad (2-77)$$

$$h'_i = b_i + 2c_i x_i + 3d_i x_i^2, \quad (2-78)$$

$$h''_i = 2c_i + 6d_i x_i. \quad (2-79)$$

(2) Similarly approaching x_i within $x_i \leq x \leq x_{i+1}$, we can have

$$h_i = a_{i+1} + b_{i+1} x_i + c_{i+1} x_i^2 + d_{i+1} x_i^3, \quad (2-80)$$

$$h'_i = b_{i+1} + 2c_{i+1} x_i + 3d_{i+1} x_i^2, \quad (2-81)$$

$$h''_i = 2c_{i+1} + 6d_{i+1} x_i. \quad (2-82)$$

(3) Enforcing the continuities of the first and second derivatives at $x = x_i$, we can get

$$b_i + 2c_i x_i + 3d_i x_i^2 = b_{i+1} + 2c_{i+1} x_i + 3d_{i+1} x_i^2 \quad (2-83)$$

$$2c_i + 6d_i x_i = 2c_{i+1} + 6d_{i+1} x_i \quad (2-84)$$

Using these, together with Eqs. (2-77) and (2-80), we have four equations at node i ($i = 1, \dots, n - 1$).

(4) At end nodes $i = 0$ and $i = n$, using known h_0 and h_n and also imposing zero second derivatives

$$2c_1 + 6d_1 x_0 = 0 \quad (2-85)$$

$$2c_n + 6d_n x_n = 0 \quad (2-86)$$

This will give 4 additional equations.

In total there are $4(n - 1) + 4 = 4n$ equations and the number is the same as that of the unknowns in Eq. (2-76). Thus, coefficients a_i , b_i , c_i and d_i ($i = 1, \dots, n$) can be obtained. Then, from Eq. (2-76), we can calculate the values of $h(x)$ at the red points along AB of the finer block.

The finer grid also corresponds to smaller time step. Therefore, temporal interpolation is also needed. Let t_1 , t_2 and t_3 be the time instants corresponding to the coarser grid. Based on the above spatial interpolation, the values at the fine grid nodes, or on both blue and red points of AB, at these time instants can be obtained. Let $g(t_1)$, $g(t_2)$ and $g(t_3)$ be at a given finer grid node. As a smaller time step δ_{tf} is used for the fine grid, result at t^* between the two instants is needed. Three-point Lagrangian formulation is then adopted for the temporal interpolation

$$g(t) = \sum_{k=1}^3 g(t_k) \left(\prod_{j=1, j \neq k}^3 \frac{t-t_j}{t_k-t_j} \right) \quad (2-87)$$

For t^* , we take one point t_3 on its right, and two points t_1 and t_2 on the left, as shown in Fig. 2-5, Eq. (2-87) may be expressed as

$$g(t^*) = g(t_1) \frac{(t^*-t_2)(t^*-t_3)}{(t_1-t_2)(t_1-t_3)} + g(t_2) \frac{(t^*-t_1)(t^*-t_3)}{(t_2-t_1)(t_2-t_3)} + g(t_3) \frac{(t^*-t_1)(t^*-t_2)}{(t_3-t_1)(t_3-t_2)} \quad (2-88)$$

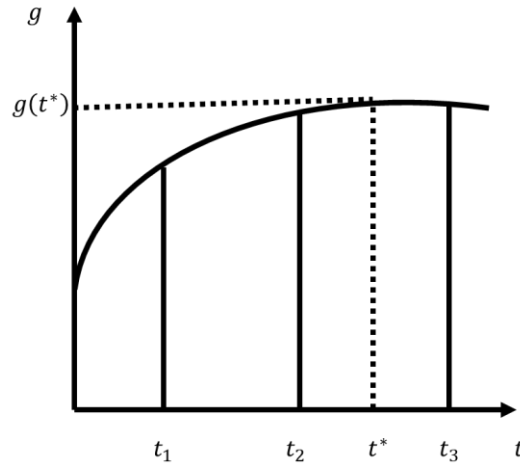


Fig. 2-5 Sketch for three-point Lagrangian interpolation.

The relationship between t^* and t_2 is

$$t^* = t_2 + j\delta_{tf} \quad (j = 1, \dots, m - 1). \quad (2-89)$$

Based on the above equation and $t_3 - t_2 = t_2 - t_1 = \delta_{tc} = m_{cf}\delta_{tf}$, Eq. (2-88) can be rewritten as

$$g(t^*) = \frac{j(j-m_{cf})}{2m^2} g(t_1) + \frac{j^2+m_{cf}^2}{m^2} g(t_2) + \frac{j(j+m_{cf})}{2m^2} g(t_3). \quad (2-90)$$

For $m_{cf} = 2$, we can have only $j = 1$ in Eq. (2-89)

$$t^* = t_2 + \delta_{tf}, \quad (2-91)$$

Eq. (2-90) becomes

$$g(t^*) = -0.125g(t_1) + 0.75g(t_2) + 0.375g(t_3). \quad (2-92)$$

For $m_{cf} = 2$, the detailed exchange between the two blocks is summarized as follow.

- (1) $f_i(\mathbf{x}, t + 2\delta_{tf})$ in the coarser block can be calculated by $f_i(\mathbf{x}, t)$ based on Eqs. (2-15) and (2-75), which provides its values along the blue points of AB.
- (2) $f_i(\mathbf{x}, t + 2\delta_{tf})$ of red points on the AB line for the finer block can be calculated by Eq. (2-76).
- (3) $f_i(\mathbf{x}, t + \delta_{tf})$ in the finer block can be calculated by $f_i(\mathbf{x}, t)$ based on Eqs. (2-15) and (2-75).
- (4) The values of $f_i(\mathbf{x}, t + \delta_{tf})$ at both blue and red points of AB are obtained from Eq. (2-92), which are used as the boundary condition for the finer block.
- (5) $f_i(\mathbf{x}, t + 2\delta_{tf})$ in the finer block can be calculated by $f_i(\mathbf{x}, t + \delta_{tf})$ with the boundary condition along AB.
- (6) $f_i(\mathbf{x}, t + 2\delta_{tf})$ values on the blue points along CD line obtained from the finer mesh is used as boundary condition for the coarser mesh.
- (7) Return to step (1) and start the next time.

Chapter 3

Flow past two cylinders in different arrangements

In this chapter, the force components on two circular cylinders in tandem, side-by-side and staggered arrangements and in a uniform incoming flow are investigated systematically. The cases considered correspond to relatively low Reynolds number. DNS is used and no turbulence mode is adopted. The analysis of this chapter has been published in *Journal of Fluids and Structures*, see [Jiao and Wu \(2018\)](#).

3.1 Convergence and comparison

The flow past a fixed cylinder at $Re = 40$ and $Re = 200$ has been carried out in order to verify the numerical method. The incoming flow is from the left hand side of the body. The cylinder is located in the flow field. The computational domain is taken as $Le = 10D$, $Ls = 10D$ and $Lr = 20D$, as shown in Fig. 3-1(a). A Dirichlet boundary condition ($\mathbf{u} = (u_0, 0)$) is adopted at the inflow and far-field boundaries. The potential flow solution is used in the initial condition. For analyses, the fluctuating force history is collected for a sufficiently long period of time with $T = u_0 t / D > 1200$.

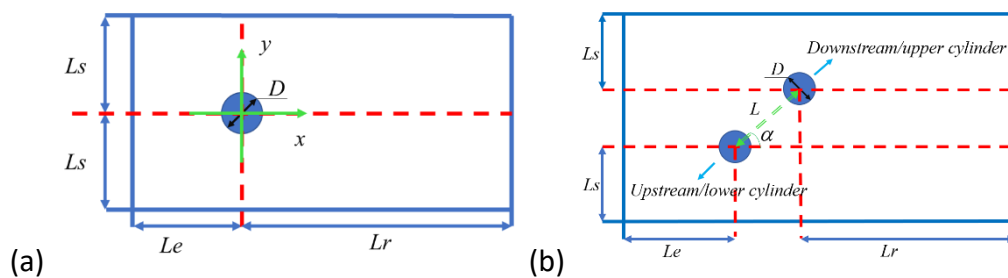


Fig. 3-1 Computational configurations for (a) a single cylinder and (b) two cylinders.

Convergence tests should be undertaken with respect to the grid size l , the artificial compressibility through Mach number M_α and time step δ_t . In the D2Q9 model outlined in

Section 2.1, $\delta_t = l = c = 1$, $M_a = u/c_s$ and $c_s = c/\sqrt{3}$. In such a case, at given Reynolds number, the nondimensionalized time step will be fixed when the grid parameter $s = D/l$ and Mach number have been chosen. Thus, its convergence is reflected in the convergence with s and M_a , respectively. For a cylinder, Mach number is set as $M_a = 0.1$, which is same to that used by [Li et al. \(2004\)](#). The grid convergence is investigated by the $Re = 200$ flow shown in Table 3-1, which indicates that $s = 70$ is sufficient to obtain convergent solution. A good agreement can be found, suggesting that the present numerical method is accurate and resolution is adequate. Vortex contour of this case are given in Fig. 3-2, which shows the oscillatory flow of the wake. The temporal variations of the drag and lift coefficients are shown in Fig. 3-3. Fourier analysis of the periodic drag and lift coefficients is shown in Fig. 3-4. We may observe that the periodic oscillation gives virtually a single frequency. The Strouhal number corresponding to the lift coefficient is 0.207, and that of drag coefficient is 0.414. The latter is the double of the former. In fact when the body is symmetric and the flow pattern shown in Fig. 3-2 is periodic in time, the flow at $y > 0$ and $T + T_v/2$ should be the mirror image of the flow at $y < 0$ and T . Using this, it can be shown that the lift coefficient C_L has frequency components of $(2n + 1)St$ only while the drag coefficient C_D has $2nSt$ ($n = 0, 1, \dots$) ([Wu, 2000](#)).

Table 3-1

Drag and lift coefficients and Strouhal number on a single cylinder at $Re = 200$

	C_D		C_L		St
	Max.	Min.	Max.	Min.	
Present result:					
s=50	1.338	1.252	0.569	-0.569	0.206
s=70	1.333	1.250	0.569	-0.569	0.207
s=98	1.334	1.251	0.569	-0.569	0.207
Wu & Hu (2006)	1.385	1.324	0.563	-0.564	0.190
Chan & Anastasiou (1999)	1.50	1.42	0.70	-0.70	0.23
Braza et al. (1986)	1.35(mean)				0.20
Williamson (1996)					0.198

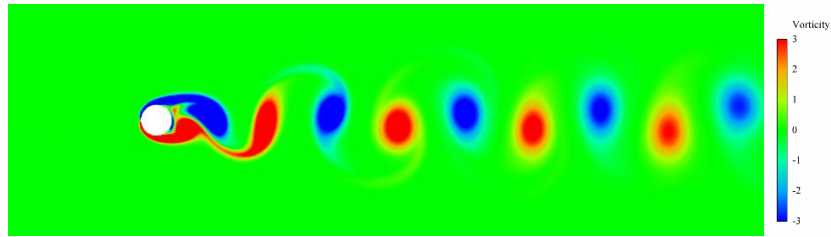


Fig. 3-2 Vortex contours for a single cylinder at $T = 185.7$ with $Re = 200$.

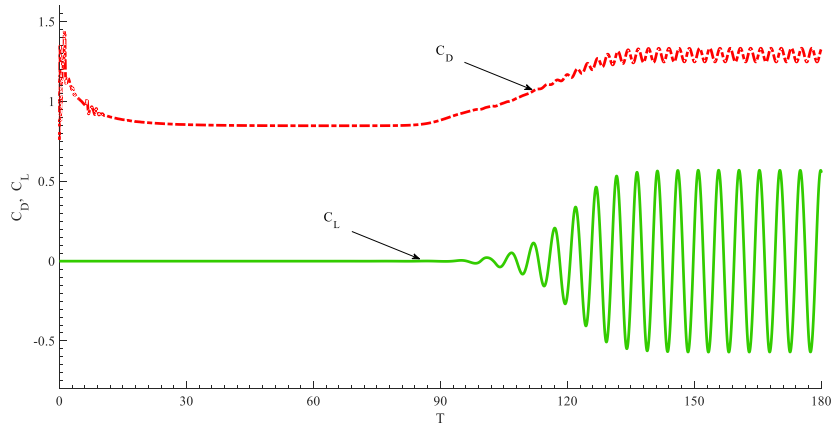


Fig. 3-3 Drag and lift coefficients on a single cylinder at $Re = 200$.

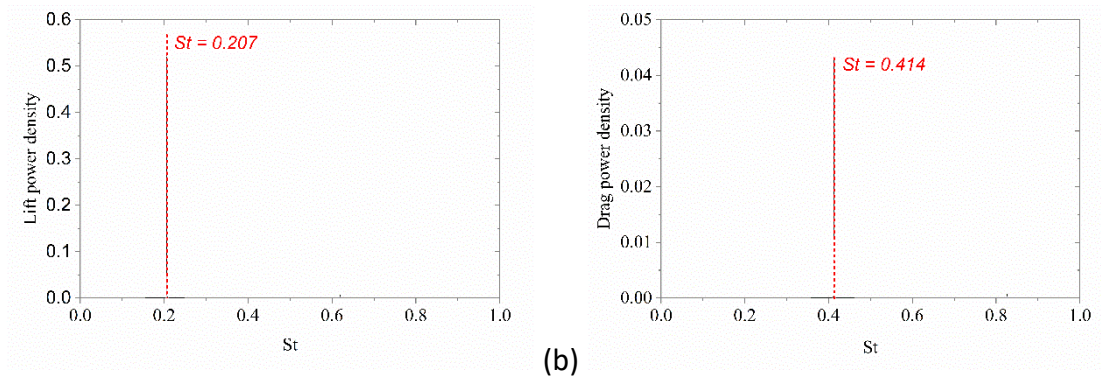


Fig. 3-4 Power spectra of (a) the lift and (b) drag coefficients on a single cylinder with $Re = 200$.

3.2 The flow past two stationary cylinders in various arrangements

In this section, we will analyse the fluctuating force acting on individual cylinders at the fixed centre-to-centre spacing $L^* = L/D = 1.5$ and Reynolds number $Re = 200$. The arrangement of the cylinders will vary with the alignment angle α . The computational configuration for two cylinders is shown in Fig. 3-1(b).

The effect of domain size is first investigated. Two domains with (1) $Le = 10D$, $Ls = 10D$ and $Lr = 20D$; (2) $Le = 14D$, $Ls = 12D$ and $Lr = 28D$, respectively, are used to solve the problem of flow past a pair of cylinders in tandem. Lift and drag coefficients together with Strouhal number obtained with grid parameter $s = 70$ and Mach number $M_a = 0.1$ are given in Table 3-2. Results from two domain sizes are virtually identical, the largest relative error is about 0.47%. This confirms the adequacy of domain size (1) in computing the flow past two stationary cylinders in various arrangements. Moreover, computations are carried out for two different values of grid parameter s whose alternation changes both grid size and the time, to primarily confirm the mesh convergence for the case of two cylinders. The relative difference in mean C_D , maximum C_L and St of both tandem cylinders obtained with $s = 70$ and 98 shown in Table 3-2 is about 0.1%. Convergence with Mach number are also conducted with $M_a = 0.1$ and 0.05 in Table 3-2 and excellent agreement between the two sets of results has been found. In the subsequent calculations, $s = 70$ and $M_a = 0.1$ are used.

Table 3-2

Drag and lift coefficients, and Strouhal number for two tandem cylinders (Indexes 1 and 2 represent downstream and upstream cylinder, respectively.)

Domain	s	M_a	\bar{C}_{D1}	\bar{C}_{D2}	Max. C_{L1}	Max. C_{L2}	St_1	St_2
(1)	70	0.1	-0.1577	1.0209	0.0753	0.0213	0.168	0.168
(2)	70	0.1	-0.1579	1.0206	0.0753	0.0212	0.168	0.168
(1)	98	0.1	-0.1578	1.0209	0.0753	0.0213	0.168	0.168
(1)	70	0.05	-0.1577	1.0208	0.0753	0.0213	0.168	0.168

Fig. 3-5 displays the mean drag and lift coefficients on two cylinders with the alignment angle α . Note that all the length of the time over which the mean is obtained is the same as that used to get corresponding spectra of forces. It can be seen that with the increase of α , mean drag coefficients on both cylinders also increase. Compared with downstream/upper cylinder, the increase of mean drag coefficient on the upstream/lower cylinder is quicker, especially at smaller alignment angle $\alpha \leq 30^\circ$. Furthermore, with the increase of α , the mean lift coefficient on the downstream/upper cylinder increases first and then decreases rapidly, while the upstream/lower cylinder has the opposite trend.

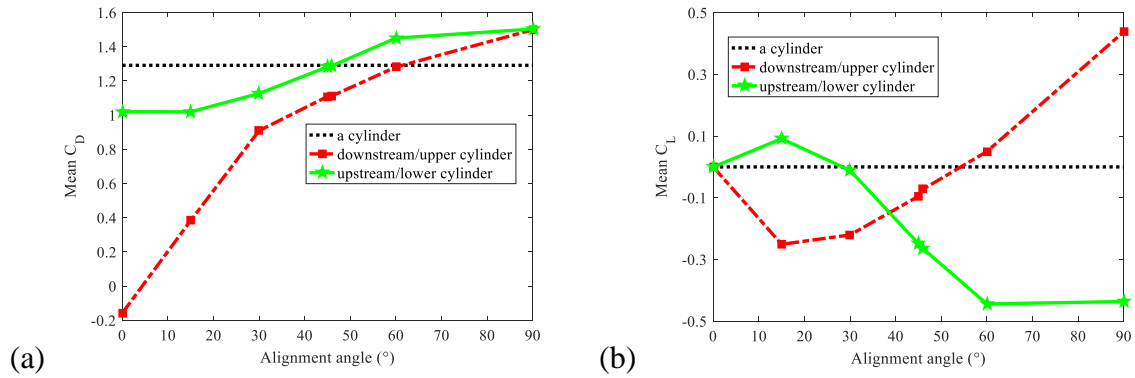


Fig. 3-5 Mean drag and lift coefficients as functions of α .

3.2.1 The flow past two tandem cylinders

Force coefficient time histories in Fig. 3-6 shows that the amplitude of the lift coefficient, and the mean and amplitude of drag coefficient for both cylinders are much smaller than that for an isolated cylinder, as a result of the vortex shedding suppression from the downstream cylinder. The drag coefficient is positive for the upstream cylinder and negative for the downstream cylinder, and thus there is an attractive force between two cylinders. These phenomena are consistent with that observed in the experiment by Zdravkovich (1987). The lift and drag coefficients on both cylinders here are almost in phase. The lift coefficients as well as drag coefficients on both cylinders here are almost in phase. The main reason may be that the vortex shed from the upstream cylinder is suppressed by the downstream cylinder and there is only one main vortex street behind two cylinders, shown in Fig. 3-8. Moreover, the configuration in tandem is symmetric about x axis and two shear layers shed from the upstream cylinder reattach at the downstream cylinder, shown in Fig. 3-8.

Spectrum analysis of the force coefficients is undertaken and the results are given in the Fig. 3-7. The lowest frequency can be defined as $f_{v0} = 1/T_v$, which is the dominant frequency for the lift forces on both cylinders at the corresponding Strouhal number $St_0 = 0.168$, as can be seen in Figs. 3-7(a) and (c). There is also a minor component at $3St_0 = 0.504$ and beyond that there is nothing further visible. The drag coefficients for both cylinders have a dominant component at $2St_0 = 0.336$ together with a much smaller component at $4St_0 = 0.672$. This

follows the pattern that the C_L on both cylinders has components of $(2n + 1)St$ ($n = 0, 1$), while the C_D of both cylinders has $2nSt$ ($n = 1, 2$), in which the steady component of $n = 0$ has been taken out. The force coefficient amplitude in the two tandem cylinder case is smaller than that on an isolated cylinder. This can be partly explained by vorticity contour in Fig. 3-8. The oscillatory behaviour of the flow behind the upstream cylinder is much weaker than that in Fig. 3-2 for the single cylinder. The Karman vortex street is not fully developed behind the upstream cylinder and in front of the downstream cylinder. This leads to a smaller oscillatory force on the upstream cylinder. For the downstream cylinder, there are oscillatory flows on both sides, although it is stronger behind the cylinder and weaker before the cylinder. Also, the incoming velocity to the downstream cylinder is lower than the free stream due to the “blockage” effect of the upstream cylinder. This leads to a smaller oscillatory force.

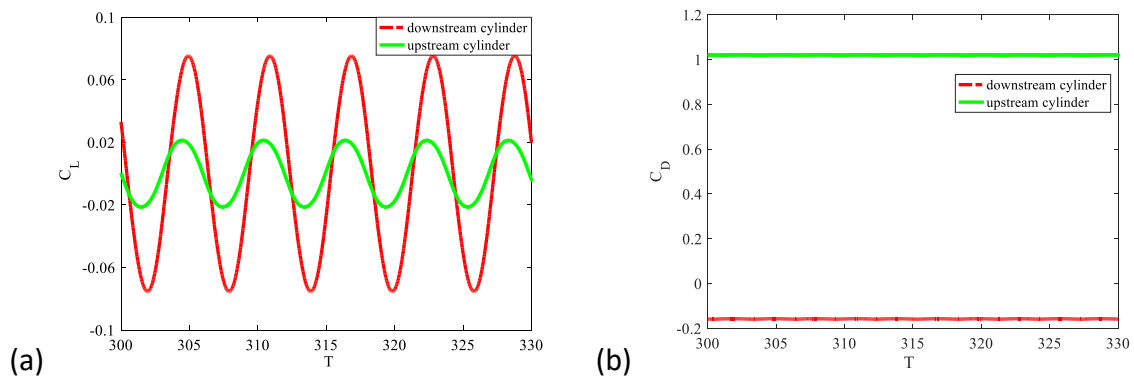
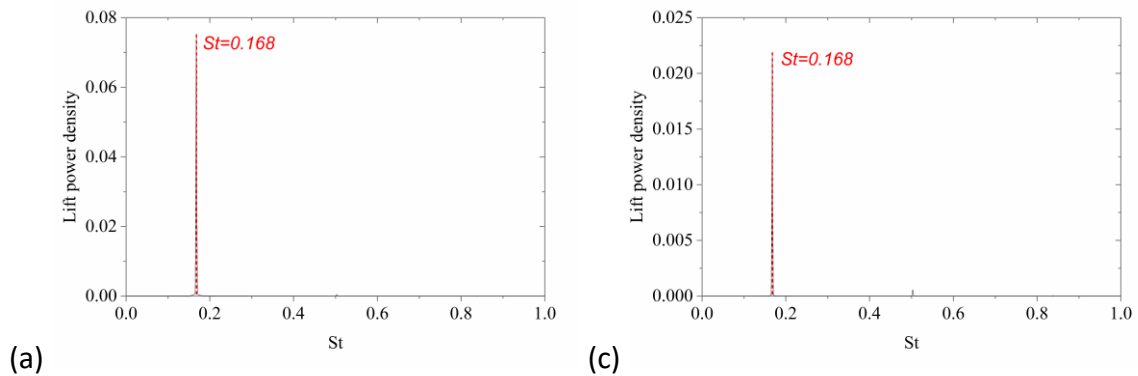


Fig. 3-6 Force coefficient time histories on two cylinders with $\alpha = 0^\circ$.



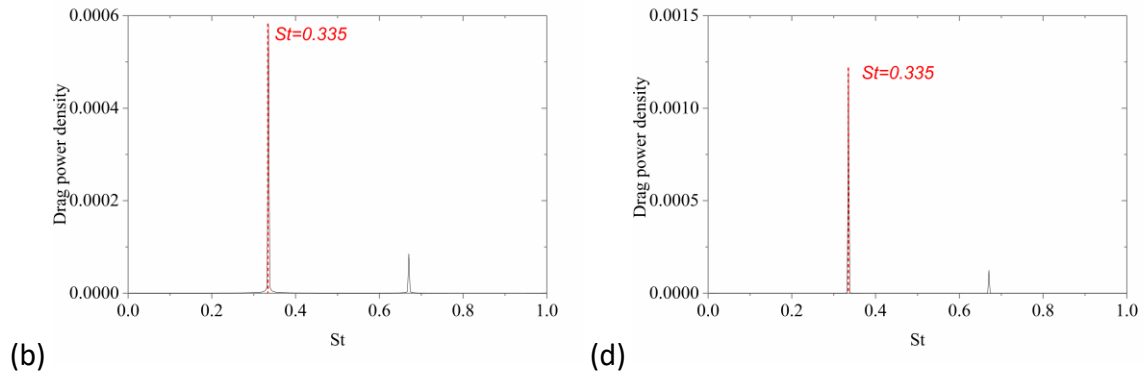


Fig. 3-7 Spectra of force coefficients for (a)-(b) downstream cylinder; (c)-(d) upstream cylinder with $\alpha = 0^\circ$.

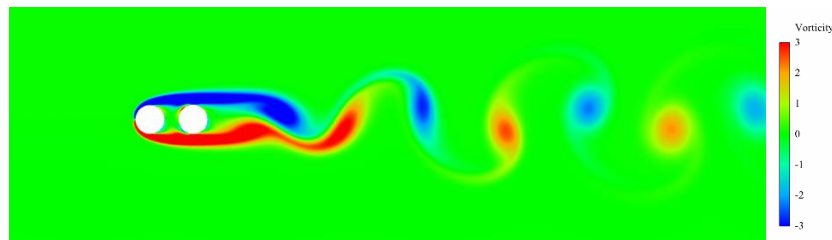


Fig. 3-8 Vortex contours at $T = 273$ with $\alpha = 0^\circ$.

3.2.2 The flow past two staggered cylinders with $\alpha = 15^\circ$

The lift and drag coefficients at $\alpha = 15^\circ$ are shown in Fig. 3-9. The oscillation of the flow here is still periodic as that in the case of $\alpha = 0^\circ$, but the detailed flow characteristics are different between these two cases. As the configuration no longer has a symmetry line as in the tandem case, around which the flow oscillates, the mean value of the lift coefficient is non-zero and both lift and drag will have components nSt_{15} ($n = 0, 1, 2 \dots$). The mean and maximum value of the lift coefficient for the upper cylinder are negative while that of the lower cylinder is positive. Even though the drag coefficient for the lower cylinder is still much higher than that for the upper cylinder, C_D on both cylinders is positive. The lift coefficients on both cylinders here are nearly in phase, which is similar to that in tandem. The main reason may be that there is also only one main vortex street behind two cylinders, shown in Fig. 3-11. However, the drag coefficients at $\alpha = 15^\circ$ are almost anti-phase. Part of the reason may be due to that compared with cylinders in tandem in Fig. 3-8, the configuration at $\alpha = 15^\circ$ is no longer

symmetric about x axis. The downstream cylinder is higher than that of the upstream cylinder, and thus only the inner shear layer from the lower cylinder is deflected into the gap between the two cylinders and attached at the upper cylinder, shown in Fig. 3-11.

Frequency spectra of lift and drag coefficients for both cylinders at $\alpha = 15^\circ$ are displayed in Fig. 3-10. The lowest frequency is $St_{15} = 0.16$, which is also the dominant frequency component. It is interesting to see that this dominant frequency is the same for both lift and drag, while in the $\alpha = 0^\circ$ case, the component of the drag coefficient is at double lowest frequency. There are also two visible components at $2St_{15} = 0.32$ and $3St_{15} = 0.48$, respectively, but their amplitudes are much smaller. The lowest frequency St_{15} here is close to that for $\alpha = 0^\circ$. This can be partly explained by vortex contour in Fig. 3-11. Even though the inner shear layer from the lower cylinder is deflected into the gap between two cylinders, it is constrained by the upper cylinder and thus there is only main Karman vortex street behind two cylinders. This is similar to that in the tandem case. On the other hand, compared with the vortex contour for the tandem case, the mean position of each oscillatory streamline here is moved upwards with the upper cylinder.

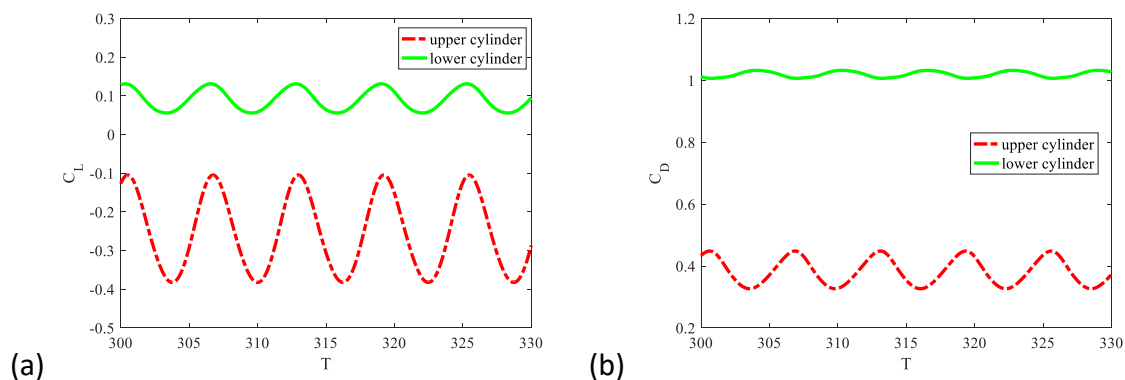


Fig. 3-9 Force coefficient time histories on two cylinders with $\alpha = 15^\circ$.

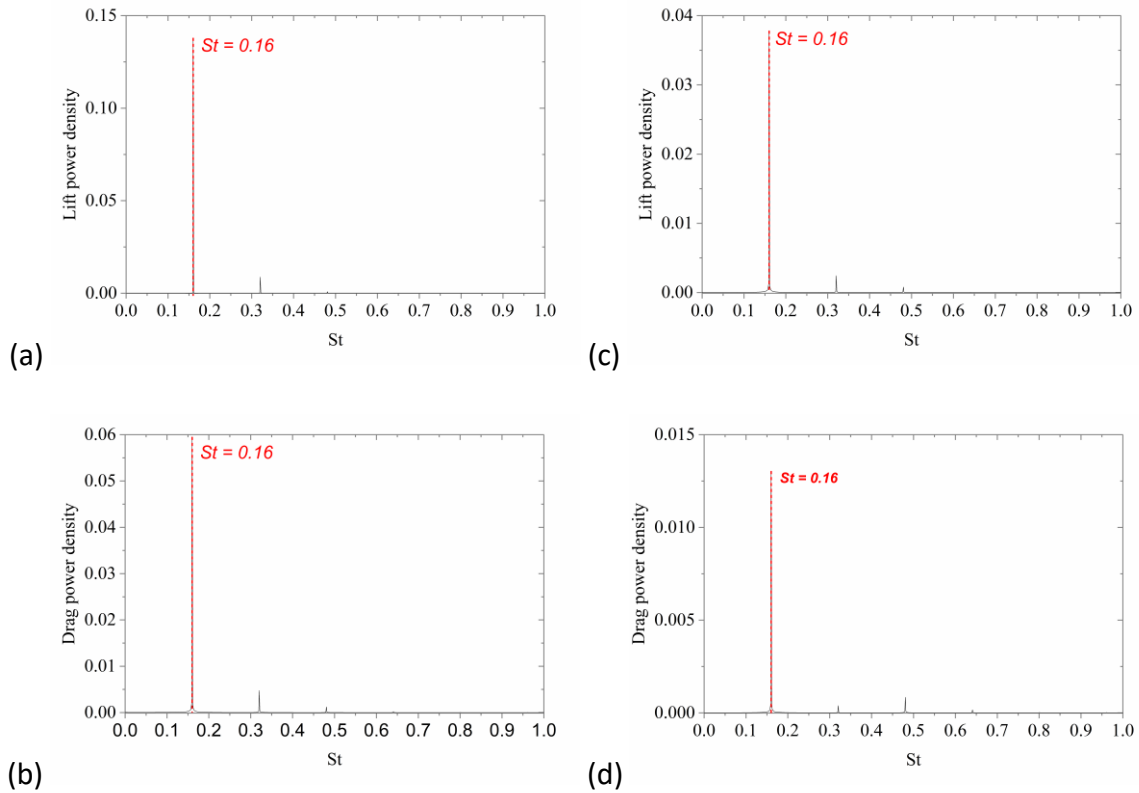


Fig. 3-10 Spectra of force coefficient for (a)-(b) upper cylinder and (c)-(d) lower cylinder with $\alpha = 15^\circ$.

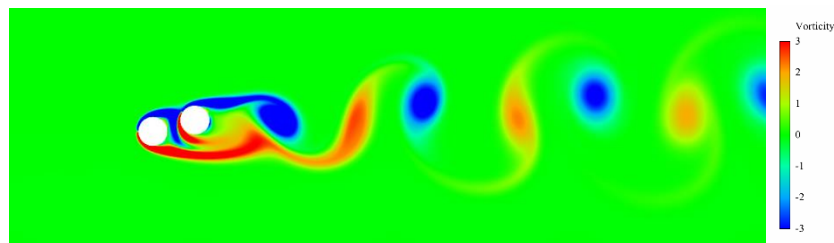


Fig. 3-11 Vortex contours at $T = 273$ with $\alpha = 15^\circ$.

3.2.3 The flow past two staggered cylinders with $\alpha = 30^\circ$

Lift and drag coefficient time histories on both cylinders at $\alpha = 30^\circ$ are shown in Fig. 3-12. Compared with that at $\alpha = 15^\circ$, the oscillation of the lift and drag coefficients on two cylinders is no longer sinusoidal. The mean value for the upper cylinder is negative, same as that in the $\alpha = 15^\circ$ case and the mean result for the lower cylinder is close to zero, which is the result when the configuration is symmetry, including the single cylinder and two cylinders

in tandem arrangements. At the same time, the difference between the mean values of drag forces on the two cylinders here becomes smaller than that at $\alpha = 15^\circ$. The oscillation of lift coefficients of the two cylinders are in phase and those of the drag coefficients are anti-phase, which is similar to that at $\alpha = 15^\circ$.

Spectra of the force coefficients on each individual cylinder are given in Fig. 3-13. The force history is periodic with respect to time, which is the same as that in the previous two cases. The lowest frequency $St_{30} = 0.067$ becomes much smaller and is less than half of $St_0 = 0.168$ at $\alpha = 0^\circ$ and $St_{15} = 0.16$ at $\alpha = 15^\circ$. However, the amplitude at the lowest frequency is no longer dominant. The largest peak here is at $2St_{30} = 0.133$, which is in fact much closer to $St_{15} = 0.16$ at the $\alpha = 15^\circ$ case. More interestingly, at $\alpha = 30^\circ$ here, more frequency components ($n = 1, 2, 3 \dots$) become visible and significant, especially for the drag coefficient on the upper cylinder. Fig. 3-14 shows vortex contour. Compared with those at $\alpha = 0^\circ$ and $\alpha = 15^\circ$, the position of the bottom side of the upper cylinder is higher than that of the lower cylinder axis.

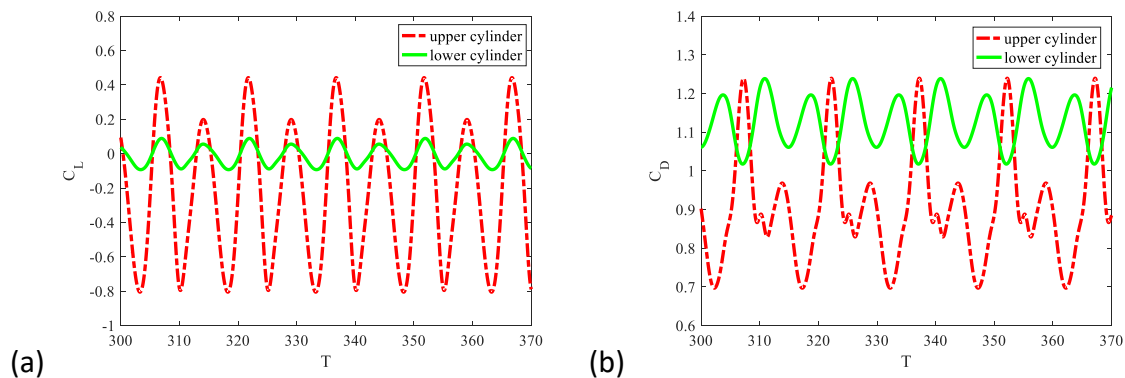


Fig. 3-12 Force coefficient time histories on two cylinders with $\alpha = 30^\circ$.

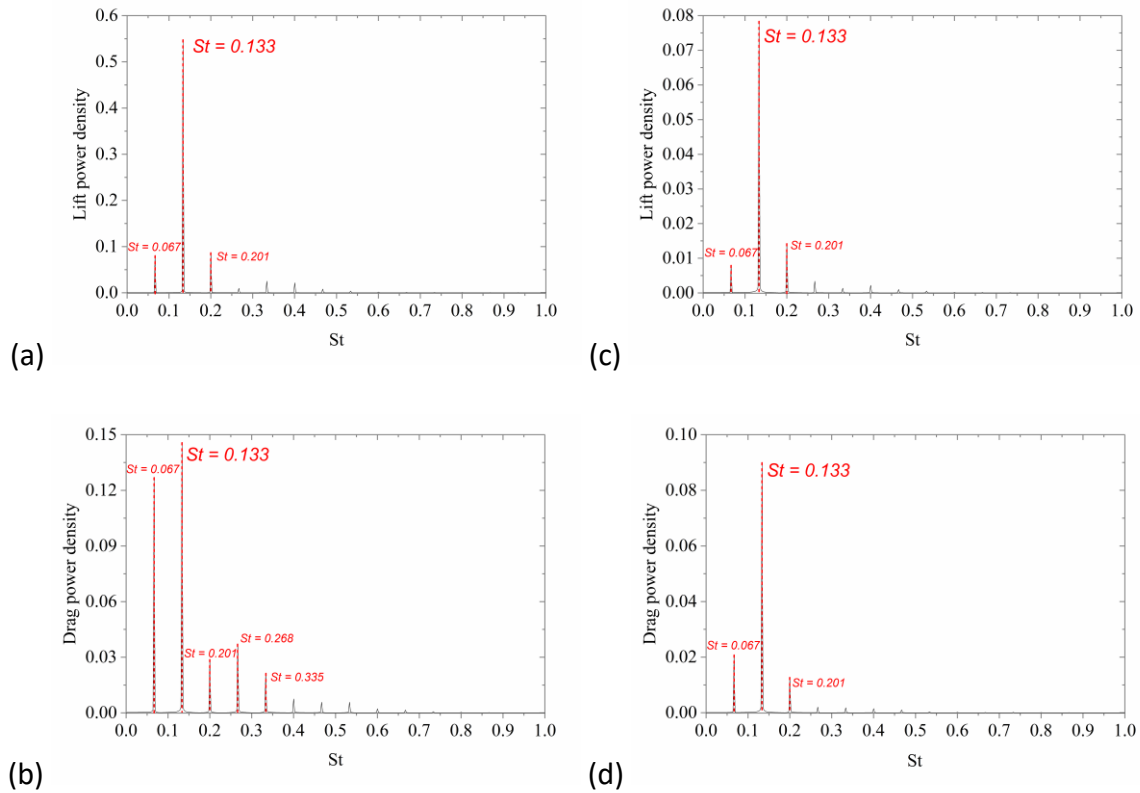


Fig. 3-13 Spectra of force coefficients for (a)-(b) upper cylinder and (c)-(d) lower cylinder with $\alpha = 30^\circ$.

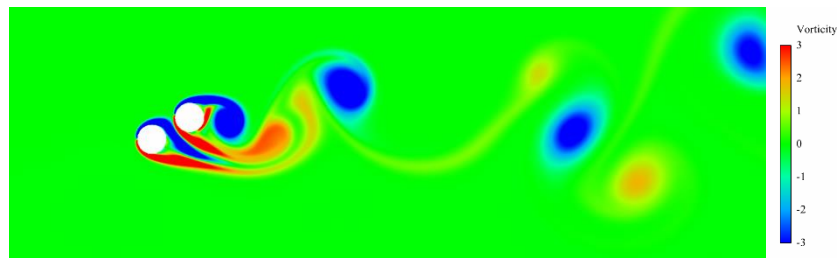


Fig. 3-14 Vortex contours at $T = 273$ with $\alpha = 30^\circ$.

3.2.4 The flow past two stationary staggered cylinders with $\alpha = 45^\circ$

Lift and drag coefficients on both cylinders at $\alpha = 45^\circ$ are shown in Fig. 3-15. The oscillation of the lift and drag coefficients on two cylinders here is far less sinusoidal than that in the $\alpha = 30^\circ$ case. The mean lift coefficient for the lower cylinder becomes once again non-zero, which is different from the case of $\alpha = 30^\circ$. The mean values of both lift coefficients are found to

be negative. The oscillations of two lift coefficients are nearly in phase, the same as what has been observed in the previous three cases. However, the drag coefficients are no longer synchronized and they are neither in-phase nor anti-phase. In addition, together with Figs. 3-6, 3-9 and 3-12, it can be found that with the increasing α , the mean drag of the upper cylinder (the downstream cylinder) changes from the negative value to the positive and increases rapidly, while that of the lower cylinder (the upstream cylinder) increases more slowly. In other words, the alignment angle α has much stronger influence on the mean drag force of the upper cylinder than that of the lower cylinder.

Spectra of force coefficients on each individual cylinder are given in Fig. 3-16. At $\alpha = 45^\circ$, frequency components are much more widely spread and a large number of components become important at frequency spectra. This shows that the force coefficients become far less sinusoidal in time. Furthermore, the lowest frequency $St_{45} = 0.017$ becomes much lower and is less than a quarter of the lowest frequency $St_{30} = 0.067$ at $\alpha = 30^\circ$. The lowest frequency is no longer the dominant component, which is similar to that in the $\alpha = 30^\circ$ case. The amplitude peak of both drag coefficients is at $4St_{45} = 0.068$. Different from two previous staggered cases, the dominant frequencies of the lift coefficients of two cylinders are no longer the same. It is at $8St_{45} = 0.136$ for the lift coefficient on the upper cylinder, which is close to $2St_{30} = 0.133$ at $\alpha = 30^\circ$, while it is at $4St_{45} = 0.068$ for the lower cylinder, which is the same as that of the drag coefficients of the two cylinders. To have some insights into the reason for different dominant frequencies of the two lift forces, the velocity component in the y -direction at four points $(7.5D, 12.0D)$, $(7.0D, 10.2D)$, $(6.2D, 9.8D)$ and $(6.2D, 9.3D)$ are investigated. Fig. 3-17 gives their time histories and the corresponding frequency spectra. For two points at lower and upper shear layers of the lower cylinder, the dominant frequency is the same and at $4St_{45} = 0.068$. For the upper cylinder, the dominant frequency of the velocity at the upper free shear layer is at $8St_{45} = 0.136$, while the dominant frequency at the lower free shear layer is at $4St_{45} = 0.068$, which is the same as that of two free shear layers from the lower cylinder. Thus, the dominant frequency of the lift coefficient of the upper cylinder is related to that of its upper shear layer, while the dominant frequency of all other force coefficients is related to that of the other three shear layers. This

is in fact consistent with what was observed in the experiment by Sumner *et al.* (2000). Fig. 3-18 shows vortex contour.

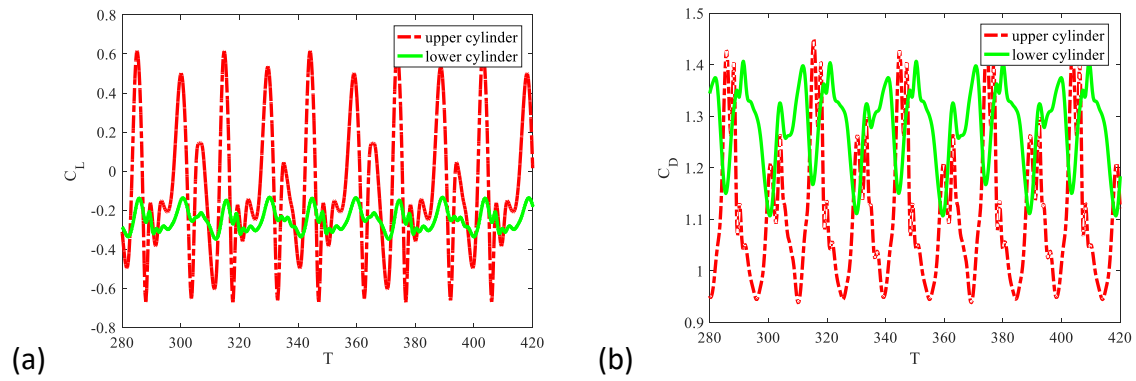


Fig. 3-15 Force coefficient time histories on two cylinders with $\alpha = 45^\circ$.

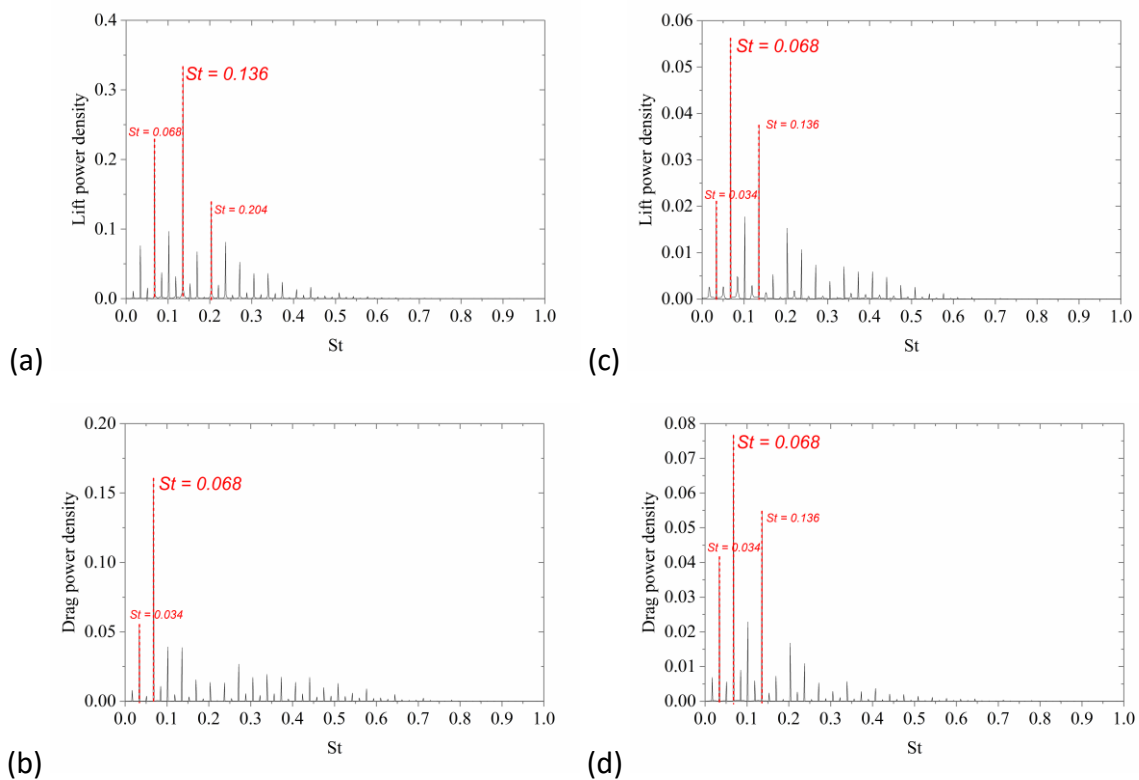


Fig. 3-16 Spectra of force coefficients for (a)-(b) upper cylinder and (c)-(d) lower cylinder with $\alpha = 45^\circ$.

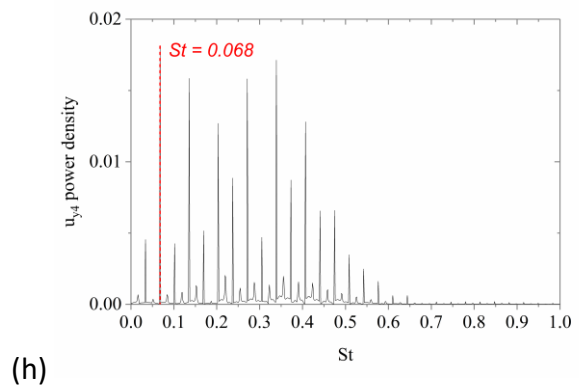
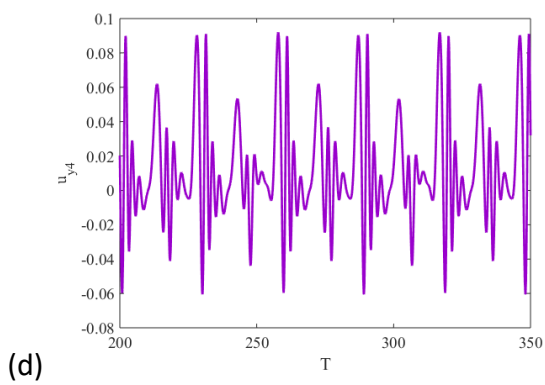
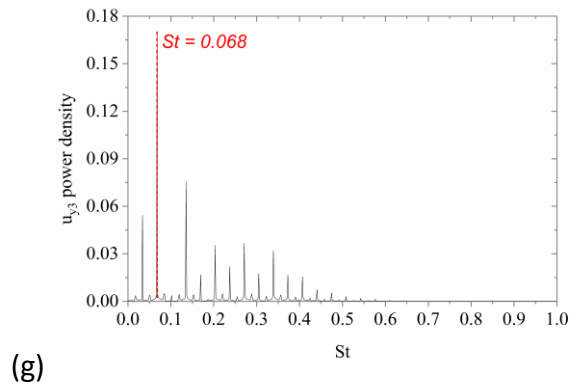
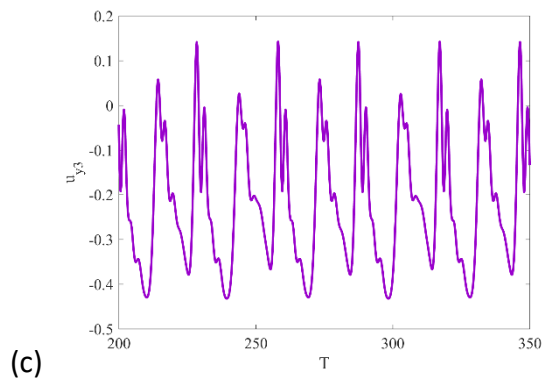
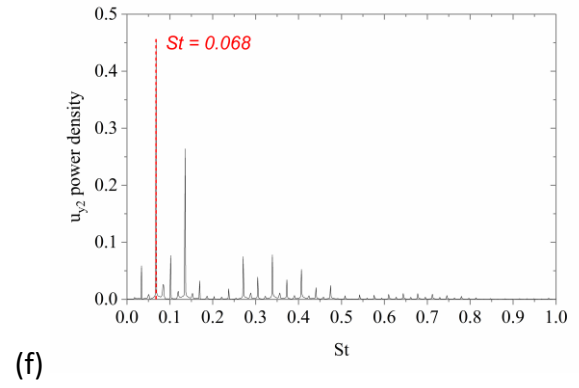
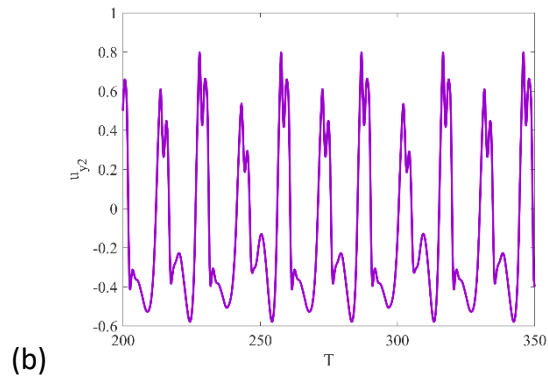
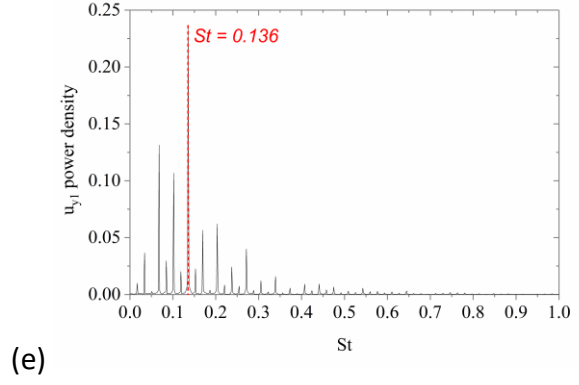
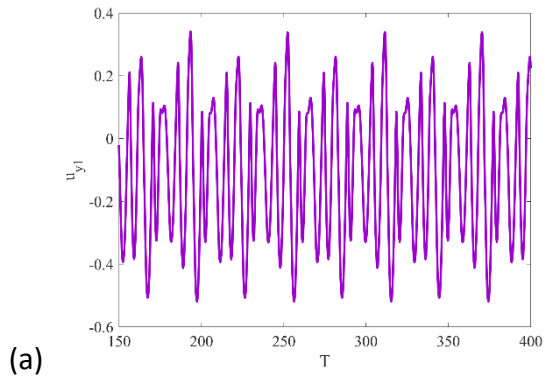


Fig. 3-17 Y-direction velocity of four points (left) and their spectra (right) with $\alpha = 45^\circ$ (Indexes 1-4 represent points at $(7.5D, 12.0D)$, $(7.0D, 10.2D)$, $(6.2D, 9.8D)$ and $(6.2D, 9.3D)$, respectively.).

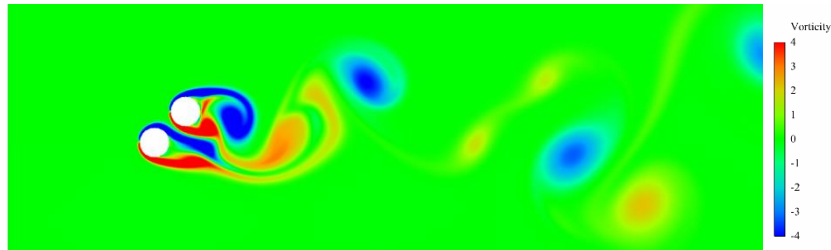


Fig. 3-18 Vortex contours at $T = 217$ with $\alpha = 45^\circ$.

3.2.5 The flow past two staggered cylinders with $\alpha = 46^\circ$

Lift and drag coefficients on both cylinders at $\alpha = 46^\circ$ are shown in Fig. 3-19. The mean lift and drag coefficients for both cylinders are similar to those in the $\alpha = 45^\circ$ case. However, what is significant here is that although there is only one-degree change in α from the previous case, the lift and drag coefficients for both cylinders are no longer periodic, which suggests that the oscillation of the flow may become unstable.

We can see from the case of $\alpha = 45^\circ$, the period of the oscillation becomes very long, although the force history can be still decomposed into Fourier series with discrete frequency components. It could be expected that when the period further increases, the Fourier series will become Fourier transform and the discrete frequency components will become a continuous distribution. This is reflected by the spectra of force coefficients in Fig. 3-20. The dominant frequency of the lift coefficient for the upper cylinder is $St = 0.133$, and that for the lower cylinder is $St = 0.066$. These two dominant frequencies are reversed for the drag coefficients of two cylinders. The local peaks at $\alpha = 46^\circ$ resemble those at $\alpha = 45^\circ$. However, the major difference is that the spectrum at $\alpha = 46^\circ$ is highly oscillatory between the local peaks, while between two neighbour peaks the amplitudes in the spectrum are virtually zero at $\alpha = 45^\circ$. Fig. 3-21 shows vortex contour. The vortices are shed from each individual

cylinder and then the vortices shed from different cylinders emerge together to form a single wake, which is similar to that in the $\alpha = 45^\circ$ case. However, based on the detailed analysis the vortex contour over a long period of time it has been found that the oscillatory flow here is no longer periodic and becomes unstable. Thus, unlike that at $\alpha = 45^\circ$, the Fourier series in time becomes the Fourier transform here.

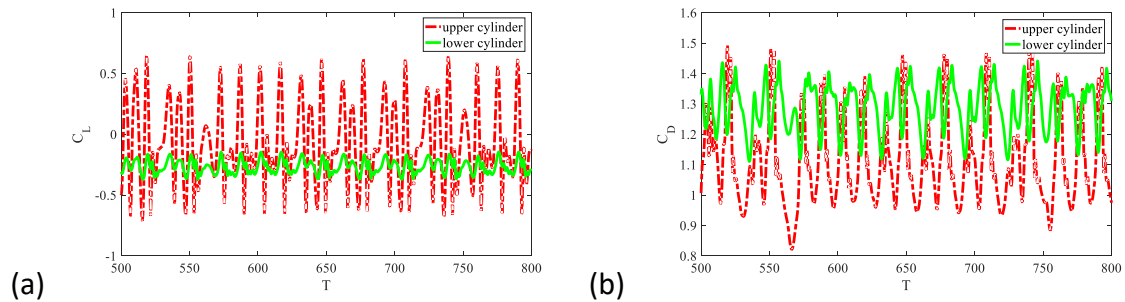


Fig. 3-19 Force coefficient time histories on two cylinders with $\alpha = 46^\circ$.

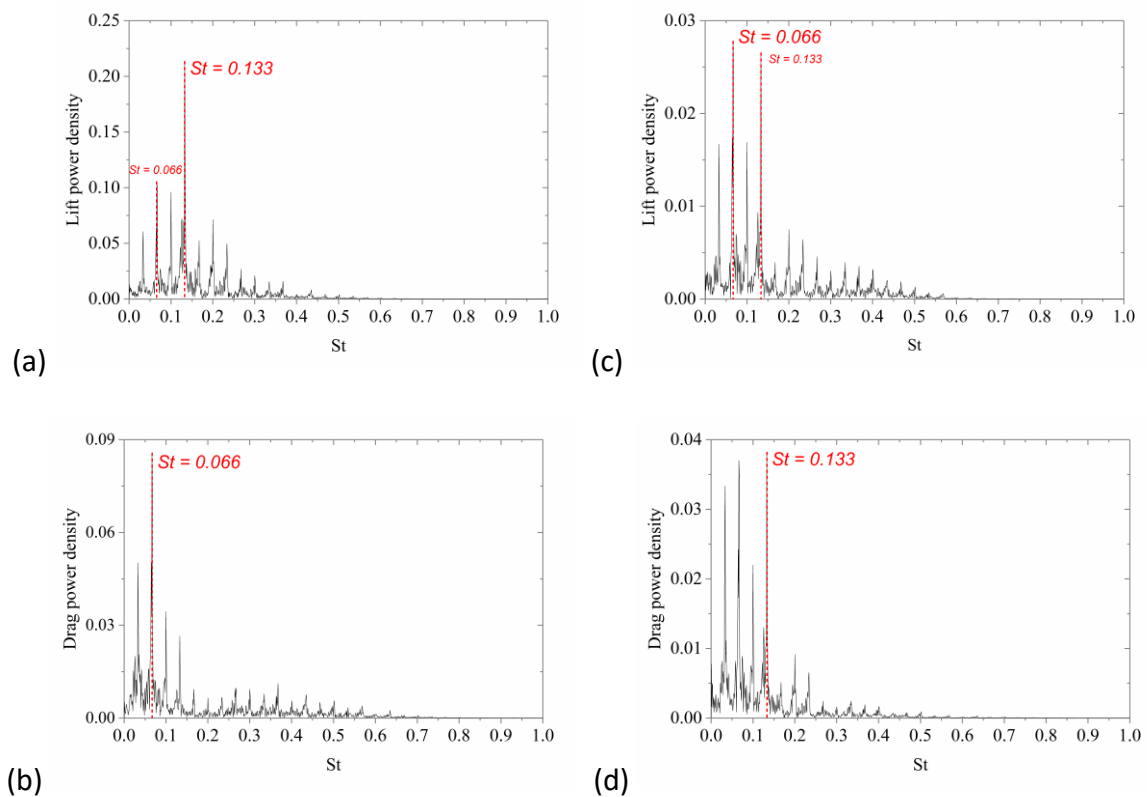


Fig. 3-20 Spectra of force coefficients for (a)-(b) upper cylinder and (c)-(d) lower cylinder with $\alpha = 46^\circ$.

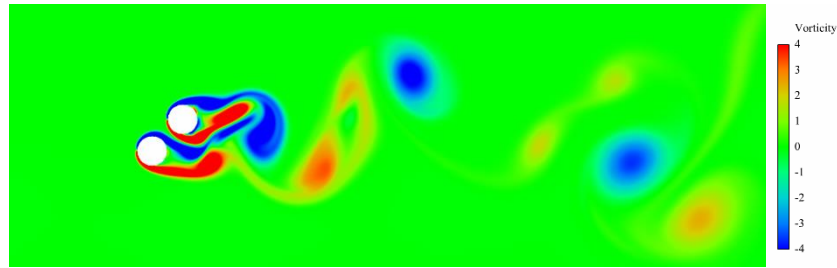


Fig. 3-21 Vortex contours at $T = 637$ with $\alpha = 46^\circ$.

3.2.6 The flow past two staggered cylinders with $\alpha = 60^\circ$

Lift and drag coefficients on both cylinders at $\alpha = 60^\circ$ are shown in Fig. 3-22. As in cases of $\alpha = 45^\circ$ and $\alpha = 46^\circ$, the mean lift coefficient for the lower cylinder is negative. However, for the upper cylinder, the mean lift coefficient becomes positive, which is opposite to that at $\alpha = 45^\circ$ and $\alpha = 46^\circ$. From the analysis of the drag coefficients for two cylinders, it can be found that the mean value for the lower cylinder is higher than that for a single cylinder while for the upper cylinder, it is close to that for a single cylinder.

Frequency spectra of the force coefficients on two cylinders are given in Fig. 3-23. As in cases of $\alpha = 45^\circ$ and $\alpha = 46^\circ$, the locations of spectrum peaks of the lift coefficients for upper and lower cylinders are different, and are at $St = 0.107$ and $St = 0.08$, respectively. The peaks for drag forces on two cylinders are both at $St = 0.08$. It is interesting to see that the amplitude of the drag coefficient at a much smaller frequency $St = 0.027$ is also high and it is close to that at the dominant frequency. The importance of much smaller frequency may reflect the slow change of the gap flow bias. It is obvious that the flow past each of the two cylinders at $\alpha = 60^\circ$ takes irregular turns in experiencing narrower or wider wake patterns in Fig. 3-24 or flip-flopping occurs. Moreover, three frequencies for Fourier analyses on the drag coefficients may be distinguished: a low flip-flopping frequency $St = 0.027$, two dominant frequencies $St = 0.08$ and $St = 0.107$. It is worthwhile to notice that the low flip-flopping frequency $St = 0.027$ plus the vortex-shedding frequency $St = 0.08$ equals the third distinctive component $St = 0.107$, which was also discussed in [Carini et al. \(2014\)](#).

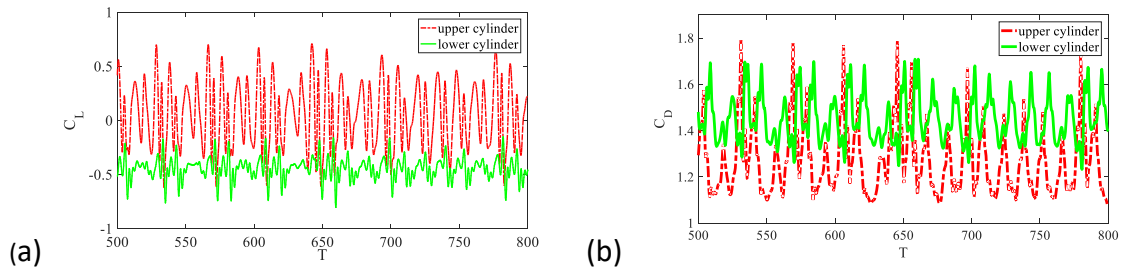


Fig. 3-22 Force coefficient time histories on two cylinders with $\alpha = 60^\circ$.

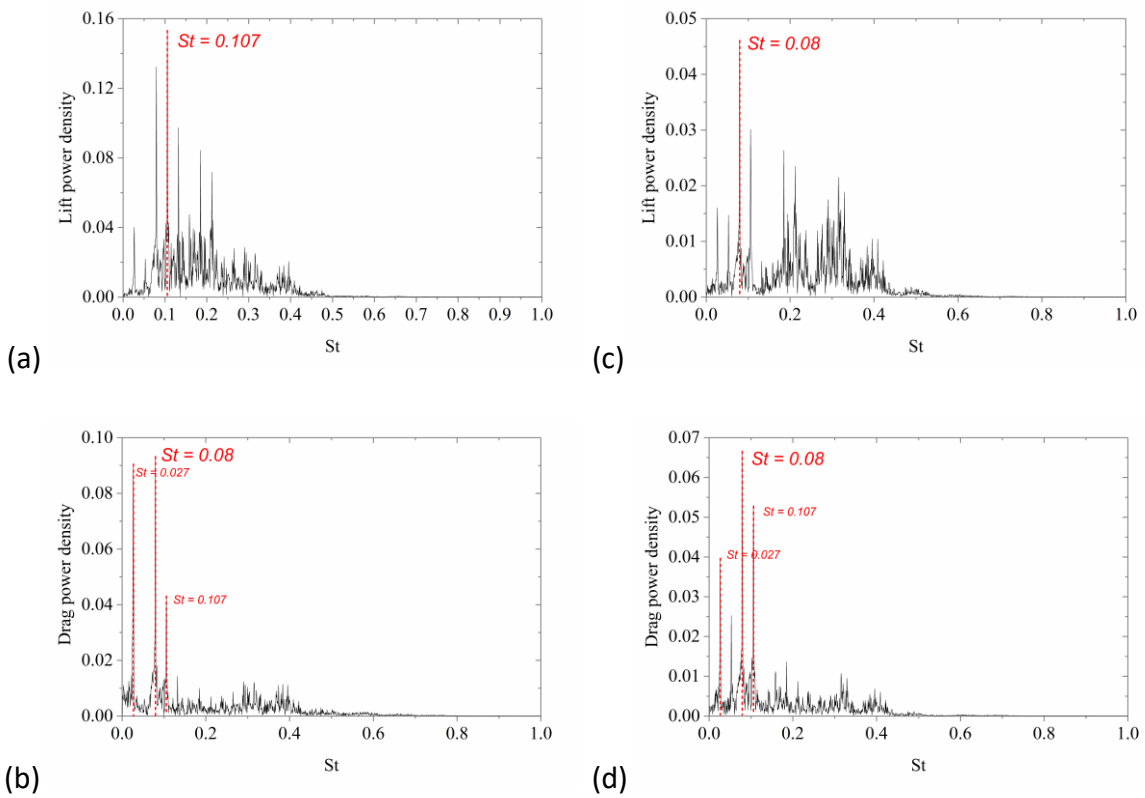


Fig. 3-23 Spectra of force coefficients for (a)-(b) upper cylinder and (c)-(d) lower cylinder with $\alpha = 60^\circ$.

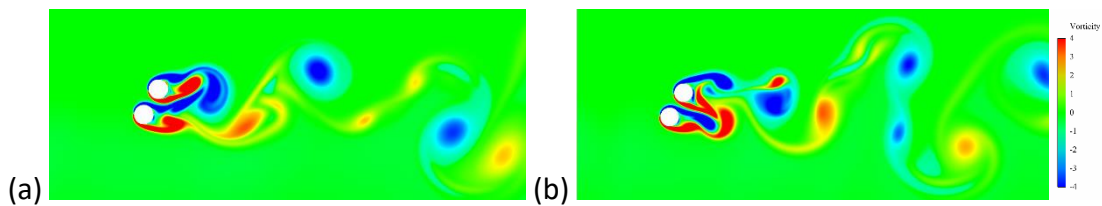


Fig. 3-24 Vortex contours with $\alpha = 60^\circ$: (a) at $T = 1309$; (b) at $T = 1344$.

3.2.7 The flow past two side-by-side cylinders

Lift and drag coefficients on both cylinders at $\alpha = 90^\circ$ are shown in Fig. 3-25. As the configuration is once again symmetric, the mean drag coefficients for two cylinders become similar. Analysis of the data has shown that the mean values for both cylinders are higher than that for a single cylinder. The mean lift coefficient is positive for the upper cylinder and negative for the lower cylinder, and thus there is a repulsive mean force between two cylinders. Furthermore, C_D and C_L on both cylinders yield irregular temporal variations around the mean value.

Spectra of force on each individual cylinder are given in Fig. 3-26. At $\alpha = 90^\circ$, the flow oscillation is at the random flip-flopping state. In fact, this depends on how the centre-to-centre spacing ratio L^* is deliberately chosen, as discussed in the introduction. In this flow, the narrow and wide wakes behind each cylinder alternate irregularly. Fig. 3-27 shows two snapshots as an example. Even though oscillatory forces here are very different between the upper and lower cylinders, their frequency spectra for two cylinders are similar. There are multiple intricate frequencies and a large number of relatively high peaks in spectra. The dominant frequencies for the lift coefficient on each individual cylinder are no longer a single value. They are scattered over a relatively broad range, at approximately $0.13 \leq St \leq 0.22$. The upper limit of this range is similar to the dominant frequency for a single cylinder. The reason for this range to be chosen is that outside this range the peaks in frequency spectra are much smaller. The frequency $St = 0.057$ corresponding to the spectrum peak of drag forces for the two cylinders is much smaller. Two ranges in the frequency spectra can be seen: a lower flip-flopping frequency range at $St < 0.1$ and a higher oscillatory frequency range $0.1 < St < 0.5$. Together with previous two-cylinder cases, it can be found that with the increase of alignment angle α , the oscillatory forces are no longer dominated by a component at a single frequency. As α further increases, frequency spectra of lift and drag coefficients change from the discrete components to the continuous distribution and the dominant frequency components in their spectra become more complex.

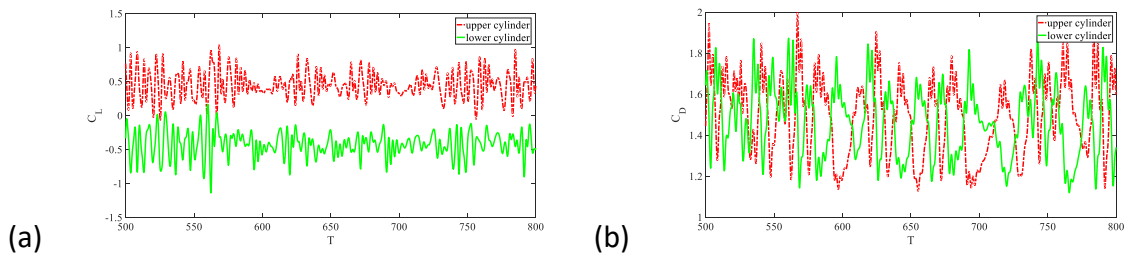


Fig. 3-25 Force coefficient time histories on two cylinders with $\alpha = 90^\circ$.

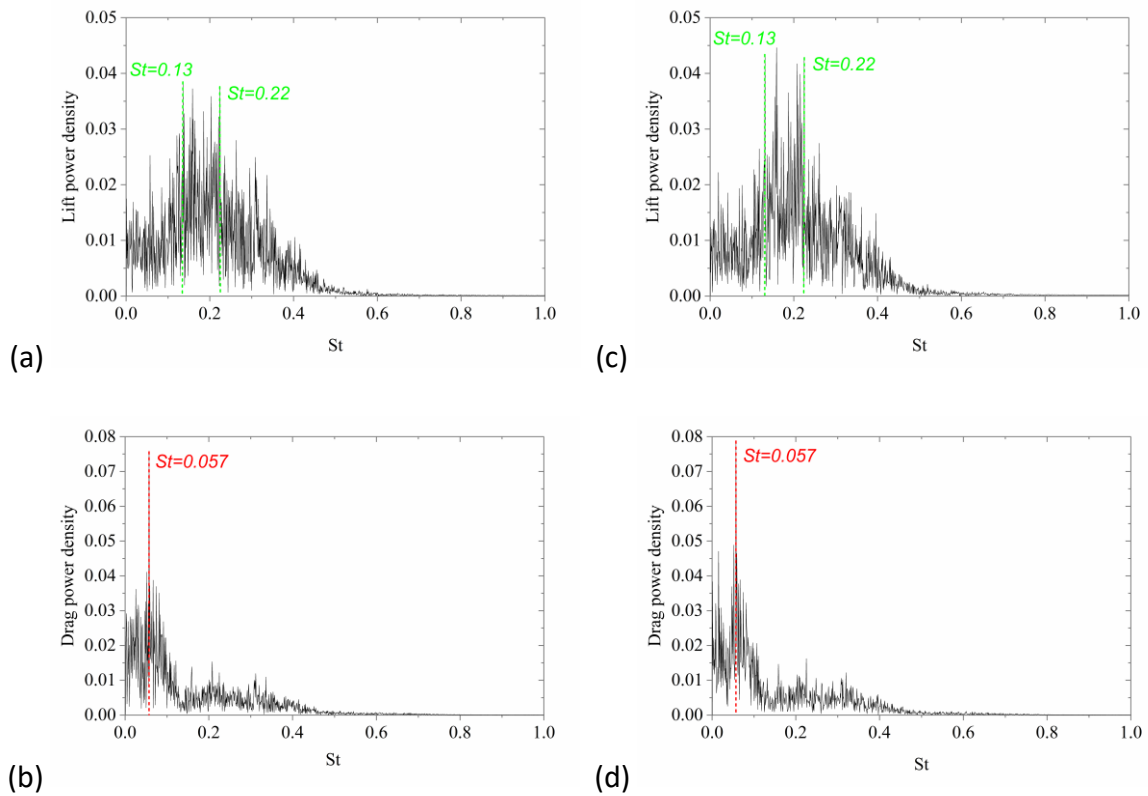


Fig. 3-26 Spectra of force coefficients for (a)-(b) upper cylinder and (c)-(d) lower cylinder with $\alpha = 90^\circ$.

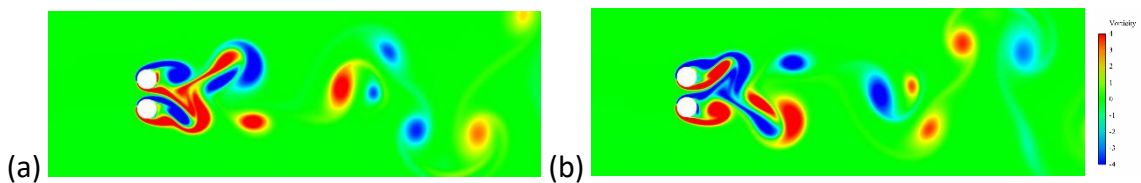


Fig. 3-27 Vortex contours with $\alpha = 90^\circ$ at (a) $T = 693$ and (b) $T = 721$.

3.3 Summary

Flow past two cylinders in different arrangements has been investigated through numerical simulations based on lattice Boltzmann method together with immersed boundary method. The focus has been on how the force on each cylinder varies with alignment angle α , as well as the vortex contour. Simulations have been performed for two cylinders with the intermediate spacing $L^* = 1.5$ at the Reynolds number $Re = 200$ and at different α . From the results, the following conclusions can be drawn.

When $0^\circ \leq \alpha \leq 45^\circ$, flow is always periodic with period T_v , which gives a lowest frequency $f_v = 1/T_v$. The force is also periodic. However, there could be frequency components nf_v ($n = 1, 2, 3 \dots$). At $\alpha = 0^\circ$, the lift coefficients C_L on both cylinders have components of $(2n + 1)f_v$ and drag coefficients C_D have $2nf_v$, although only first couple of components are visible. This is similar to that for a single cylinder. When α is non zero, the flow configuration becomes asymmetric and both C_L and C_D have components nf_v . Moreover, as α increases, the number of frequency components, at which the force is significant, also increases. While the lowest frequency becomes smaller, these frequency components become wider spread. As a result, the force oscillation becomes less sinusoidal even though it remains periodic. For $\alpha \geq 30^\circ$, the lowest frequency is no longer the dominant component. At $\alpha = 45^\circ$, the dominant frequency of the lift force on the upper cylinder is not the same as that of the other three forces. This is very much due to the oscillation of the upper shear layer of the upper cylinder, which has a dominant frequency different from that corresponding to other shear layers. When $\alpha > 45^\circ$, the motion is no longer periodic and becomes unstable. The force spectrum changes from the discrete frequency distribution to a continuous distribution, or the Fourier series becomes the Fourier transform. When α further increases, flip-flopping state with low frequency may start to develop. At $\alpha = 60^\circ$, three distinctive frequencies of force coefficients have been observed. The lowest is the flip-flopping frequency and the second one is the dominant frequency due to wake oscillation, while the summation of these two equals to the third component. At $\alpha = 90^\circ$, a large number of relatively high peaks have been seen in the force spectrum and the dominant force is over a relatively broad range of

frequencies. Interestingly, although two cylinders experience irregular force oscillation at $\alpha = 90^\circ$, their frequency spectra are similar to each other.

Chapter 4

Free vibration predicted using forced oscillation in the lock-in region

In Chapter 3, flow past stationary cylinders has been considered. However, as it is observed that the force becomes oscillatory when the Reynolds number is above a threshold, especially in the transverse direction. This can lead to vibration of a non-fixed cylinder. In this chapter, the motion of a cylinder is further considered. Forced oscillation is a method to investigate the fluid-structure during VIV. The motion in forced oscillation is always prescribed sinusoidal. The response of the wake to the forced motion can be investigated in isolation. In such a case, it is easier to provide forced motion results systematically than those from free motion. In this chapter, we first provide the mathematical analysis for the conditions of the equivalent forced and free motions. Then, it is verified through numerical results obtained from immersed boundary method and lattice Boltzmann method. Also, the effect of the combined mass-damping parameter on the motion amplitude is discussed through mathematical analysis. The content of this chapter has been published in *Physics of Fluids*, see [Jiao and Wu \(2018\)](#), which was chosen as one of the featured papers, or one of the best *PoF* papers chosen by the editors.

4.1 Equivalence between free motion and forced motion at lock-in

In many engineering problems, the transverse motion of the body or the motion in the y direction is the main concern, because the lift (transverse) fluctuation is generally much larger than drag (in-line) fluctuation. If the body mass is m , the structural damping is b and stiffness is k , its governing equation is

$$m\ddot{Y} + b\dot{Y} + kY = F_L, \quad (4-1)$$

where Y is the displacement, and the over dot denotes the temporal derivative.

Kumar *et al.* (2016) reviewed the various criteria for lock-in at forced oscillation and proposed a more stringent criterion to describe lock-in, together with transition and no lock-in regions. The system can be regarded as the state of the lock-in when (a) the dominant frequency in the power spectrum of the lift coefficient is equal to the forced oscillation frequency f_c and (b) other components in its power spectrum, if any, are only at integer multiples of f_c . When only the first condition is satisfied, which means that the other components of the power spectrum can be random, the region is referred to as transition one. All other situations correspond to a no lock-in region. Their criterion is applied to identify the lock-in state at forced oscillation and free vibration in this chapter.

Based on the definition of lock-in above, the oscillation of the lift force $F_L(t)$ should have a series of frequency components, $(n + 1)f_c$ ($n = 0, 1, 2 \dots$), or

$$F_L(t) = \sum_{n=0}^{\infty} F_n \sin[2\pi(n + 1)f_c t + \phi_n]. \quad (4-2)$$

In the forced motion, the external force F_e applied on the body must follow

$$F_e(t) = m\ddot{Y}(t) - F_L(t). \quad (4-3)$$

Here if the mechanic system of the cylinder in free motion could provide this external force, its oscillation would be the same as that of the forced motion. In general, this requirement would not always be practical. However, as the dominant frequency is f_c , which means F_0 is much larger than all other components, it can be assumed that $F_L(t)$ can be approximated by the first term. In such a case, we may have

$$F_L = F_0 \sin(\omega_c t + \phi), \quad (4-4)$$

$$Y = Y_0 \sin(\omega_c t), \quad (4-5)$$

where $\omega_c = 2\pi f_c$ is the angular frequency, $\phi = \phi_0$ is the phase angle between lift force F_L and displacement Y of the cylinder.

The external force F_e in such a case can then be replaced by a constant stiffness k and structural damping b , or

$$F_e(t) = -kY(t) - b\dot{Y}(t), \quad (4-6)$$

where

$$k = m\omega_c^2 + \tilde{k}, \quad (4-7)$$

$$b = \frac{F_0 \sin \phi}{\omega_c Y_0}, \quad (4-8)$$

$$\tilde{k} = \frac{F_0 \cos \phi}{Y_0}. \quad (4-9)$$

The free motion is then expected to be same as the forced motion. Based on this principle, we may use the result in the forced lock-in motion to predict the behaviour of the free motion of the cylinder. It is interesting to see from the above two equations that while the choice of b from Eq. (4-8) is fixed at given ω_c and Y_0 , the choice of k in Eq. (4-7) is not unique and it depends on the mass of the cylinder m . In other words, the masses and stiffnesses of two cylinders may be different. Provided Eq. (4-7) or $m_2 - m_1 = (k_2 - k_1)/\omega_c^2$ is satisfied in these cases, their free motions will be same. Similar result was observed by [Shiels et al. \(2001\)](#) at $b = 0$.

4.2 Convergence and comparison

A sketch of the computational domain for forced and free motions of a circular cylinder with diameter D is shown in Fig. 3-1(a). The incoming flow is from the left hand side of the body. The cylinder is located in the flow field. The computational domain is taken as $Le = 14D$, $Ls = 20D$ and $Lr = 25.5D$, which is chosen similar to that used by [Prasanth and Mittal \(2008\)](#). A Dirichlet boundary condition ($\vec{u} = (u_0, 0)$) is adopted at the inflow and far-field boundaries. The uniform steady flow is used in the initial condition. The equation of free motion can be written as

$$m^*\ddot{Y}^* + b^*\dot{Y}^* + k^*Y^* = C_L/2, \quad (4-10)$$

where $m^* = m/\rho D^2$, $b^* = b/\rho u_0 D$ and $k^* = k/\rho u_0^2$ are nondimensionalized body mass, damping and stiffness, respectively. This is similar to what was adopted by [Shiels et al. \(2001\)](#). The equation can be solved using the Runge-Kutta method once the force coefficient is known from the flow fluid calculation. Here, the force term on the right-hand side of Eq. (4-10) is assumed to be a constant within a time step as long as the time step is small enough, which is similar to that adopted in [Zhou et al. \(1999\)](#). It should be noted that the way to nondimensionalize the equation of free motion is not unique and other forms of equations have also used, some of which have been discussed in Chapter 1.

Forced ($f_c^* = 0.177$, $Y_0^* = 0.6$) and free ($m^* = 1 - 2$, $b^* = 0$ and $k^* = 0 - 10$) oscillations have been carried out to verify the grid convergence and the artificial compressibility of the numerical method. The grid convergence is first investigated by forced and free motions through s . Mach number is taken as $M_a = 0.02$ and Reynolds number $Re = 106$. Table 4-1 shows mean drag coefficient $\overline{C_D}$, maximum lift coefficient C_{L0} and phase angle ϕ obtained from forced oscillation with two different values of grid parameters $s = 70$ and 105. Table 4-2 shows results from free vibration with $s = 70$ and 105. The largest relative error is about 0.5%. Thus, in the subsequent calculations $s = 70$ is used. It should be pointed out that the Eq. (4-10) can be calculated by Euler method, once the lift coefficient is known from the flow field calculated by LBM coupling with IBM. In addition, computations are carried out for two different values of Mach number, $M_a = 0.01$ and 0.02, to study its effect on forced and free motions at $Re = 106$. The results are shown in Tables 4-1 and 4-2. The largest relative error is about 0.6%. Thus, when $M_a \leq 0.02$, the effect of Mach number can be neglected for forced and free motions. Fig. 4-1 provides the comparison between the present results of free vibration and previous computational data from [Ahn and Kallinderis \(2006\)](#) and [Borazjani and Sotiropoulos \(2009\)](#) for the range of $k^* = 0 - 10$ at $m^* = 2$, $b^* = 0$ and $Re = 150$. There is an excellent agreement between present and other results, suggesting that the present numerical method is accurate and resolution is adequate. In the remainder of the chapter, results are computed with $s = 70$, $M_a = 0.02$ and $Re = 106$.

4.3 Simulations of forced motion at lock-in

From the analysis in section 4.1, it can be seen that the free motion of a cylinder may be predicted by the results of its corresponding lock-in forced motions under certain conditions. Here we run simulations of forced motions with different amplitude $Y_0^* = 0.05 - 0.6$ at given oscillation frequency $f_c^* = 0.2 - 0.15$. We notice that both C_{L0} and ϕ change with Y_0^* . Based on our results, it is found that the frequency of lift coefficient on a fixed cylinder is $St = 0.177$ at $Re = 106$.

Table 4-1 Mean drag coefficient, maximum lift coefficient, and phase angle for forced oscillation with $f_c^* = 0.177$ and $Y_0^* = 0.6$ at $Re = 106$

Grid Parameter	Mach Number	$\overline{C_D}$	C_{L0}	ϕ
$s = 70$	$M_a = 0.02$	1.801	1.133	-11.4°
$s = 105$	$M_a = 0.02$	1.810	1.134	-11.4°
$s = 70$	$M_a = 0.01$	1.800	1.140	-11.4°

Table 4-2 Mean drag and maximum lift coefficients, and amplitude for free oscillation with $m^* = 1$, $b^* = 0$ and $k^* = 2.438$ at $Re = 106$

Grid Parameter	Mach Number	$\overline{C_D}$	C_{L0}	f_c^*	Y_0^*
$s = 70$	$M_a = 0.02$	1.686	1.065	0.186	0.515
$s = 105$	$M_a = 0.02$	1.688	1.064	0.186	0.514
$s = 70$	$M_a = 0.01$	1.687	1.070	0.186	0.518

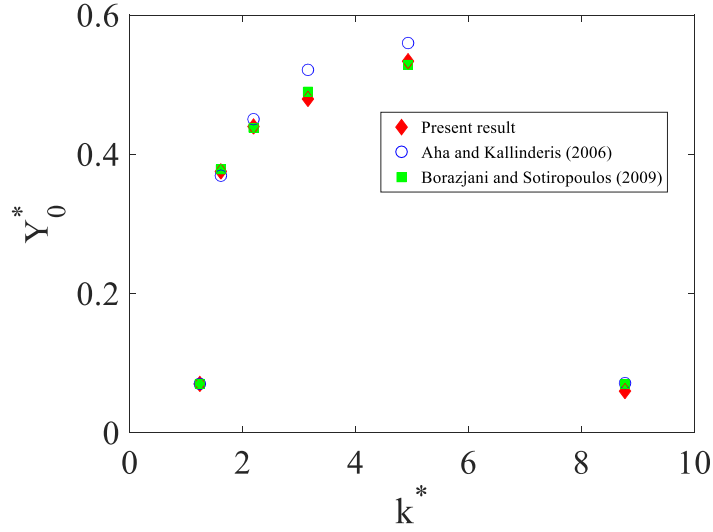


Fig. 4-1 Comparison of motion amplitude against k^* for free vibration at $m^* = 2$, $b^* = 0$, and $Re = 150$ ($s = 70$; $M = 0.02$).

We first choose $f_c^* = 0.2 > St$, and simulations have been undertaken for amplitude in the range of $Y_0^* = (0.2, 0.6)$. It is found that there is no lock-in when $Y_0^* < 0.25$, and in the lock-in region, when $Y_0^* > 0.556$ the energy transfer from the fluid to the cylinder is negative. Fig. 4-2 shows the variation of (a) C_{L0} , (b) ϕ , (c) b^* and (d) \tilde{k}^* with Y_0^* , in which \tilde{k}^* and b^* are related to k and b in Eqs. (4-7) and (4-8), respectively. Within the range of $Y_0^* = (0.25, 0.556)$, the variation of the phase angle ϕ is from 14° to 0° . At this oscillation frequency $f_c^* = 0.2$, $Y_0^* = 0.556$ is the maximum amplitude of cylinder motion, at which the equivalent free motion is possible. Beyond this value the energy transfer from the fluid to the body is negative, which means that the corresponding structural damping would have to be negative. $Y_0^* = 0.25$ is the minimum possible value for lock-in of the forced motion to occur. It is interesting to see that at $Y_0^* = 0.25$ lock-in starts with the phase angle, $\phi \approx 0^\circ$, which is similar to that at $Y_0^* = 0.556$. The values of C_{L0} at these two amplitudes are also very close. In addition, within $Y_0^* = (0.25, 0.556)$, \tilde{k}^* decreases monotonically with the increase of Y_0^* .

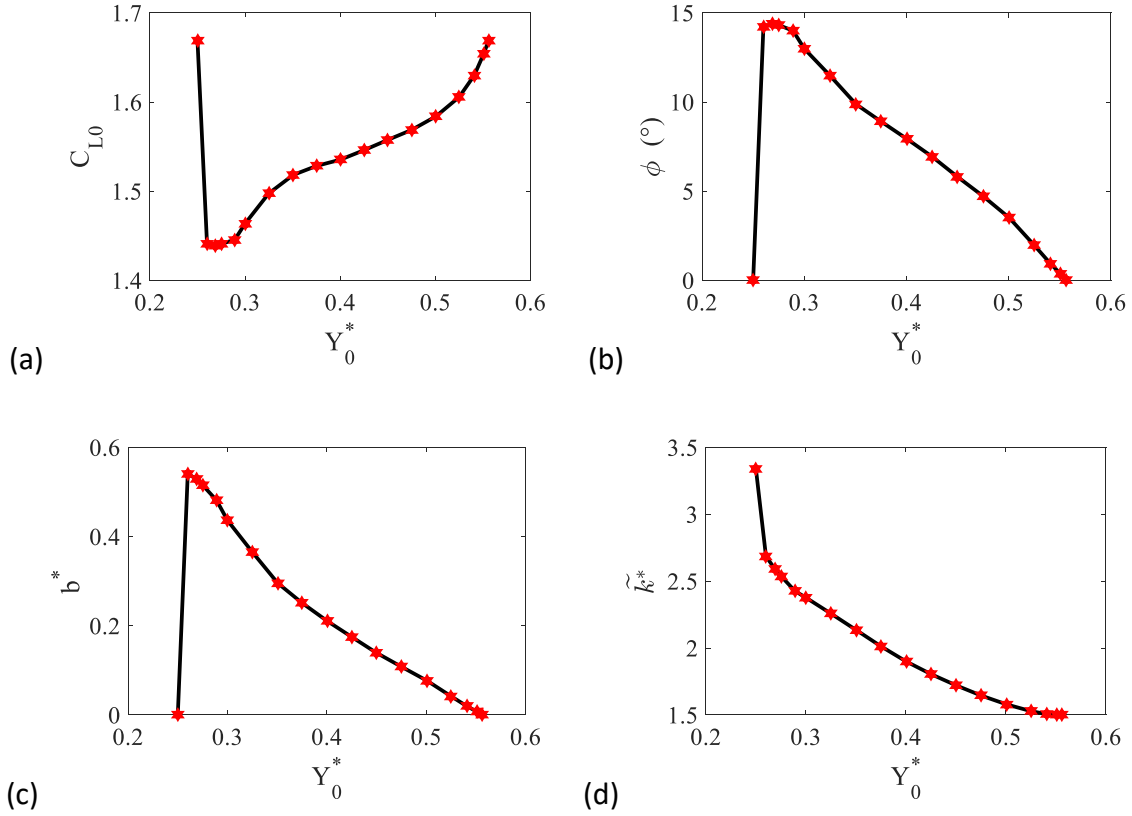


Fig. 4-2 Results of lock-in forced oscillation with different amplitudes at $f_c^* = 0.2$.

When $f_c^* = St = 0.177$, simulations have been made in the range of $Y_0^* = (0.05, 0.6)$. It is found that lock-in with the positive energy transfer from the cylinder to the fluid occurs when $Y_0^* \leq 0.5$. Fig. 4-3 shows variations of (a) C_{L0} , (b) ϕ , (c) b^* and (d) \tilde{k}^* with Y_0^* within the range of $Y_0^* = (0.05, 0.5)$. It can be seen that with the increase of Y_0^* , C_{L0} always increases while phase angle ϕ decreases. This monotonic variation with Y_0^* is different from the that in the previous case of $f_c^* = 0.2$. We notice here that when $Y_0^* \rightarrow 0$ at this frequency $f_c^* = 0.177$, C_L is expected to trend to that of a fixed cylinder and its frequency is $f_c^* = St$. Thus, lock-in can occur at very low Y_0^* . However, as Fig. 4-3(d) shows, \tilde{k}^* is already negative at $Y_0^* = 0.05$, which suggests $\phi > 90^\circ$. When Y_0^* further decreases k in Eq. (4-7) can become negative, which suggests that the equivalent free motion is no longer possible. Of course, when $\phi > 180^\circ$, b^* is also negative, which makes the equivalent free motion even more impossible.

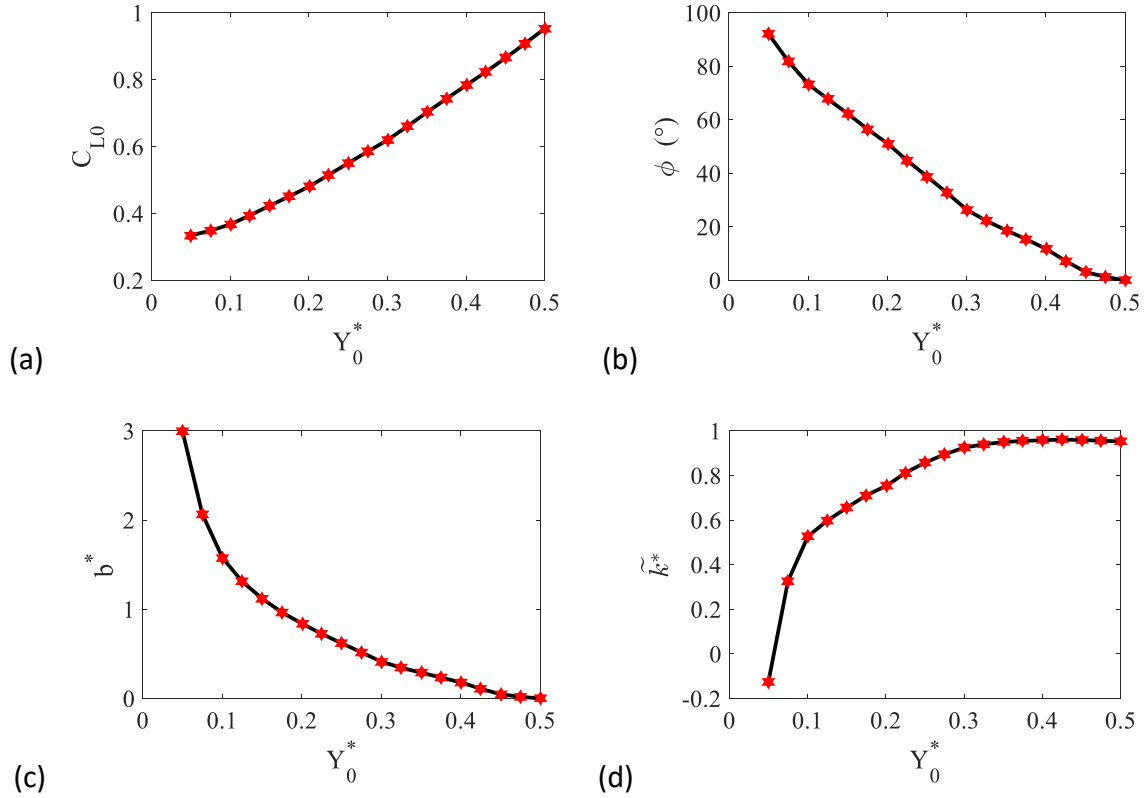


Fig. 4-3 Results of lock-in forced oscillation with different amplitudes at $f_c^* = f_v^* = 0.177$.

We run further simulations at another oscillation frequency $f_c^* = 0.15 < St$. It is found that there is no lock-in when $Y_0^* < 0.15$ approximately. In the lock-in region, when $Y_0^* > 0.4$ approximately the energy transfer from the fluid to the cylinder is negative. Fig. 4-4 shows the variation of (a) C_{L0} , (b) ϕ , (c) b^* and (d) \tilde{k}^* within the lock-in region, $Y_0^* = (0.15, 0.4)$. It can be seen that with the increase of Y_0^* , C_{L0} increases and phase angle ϕ decreases monotonically, which is similar to that at $f_c^* = St = 0.177$. However, with the increase of Y_0^* within $Y_0^* = (0.15, 0.4)$, b^* increases slightly initially before it decreases, while \tilde{k}^* increases continuously, which is also similar to that $f_c^* = St = 0.177$.

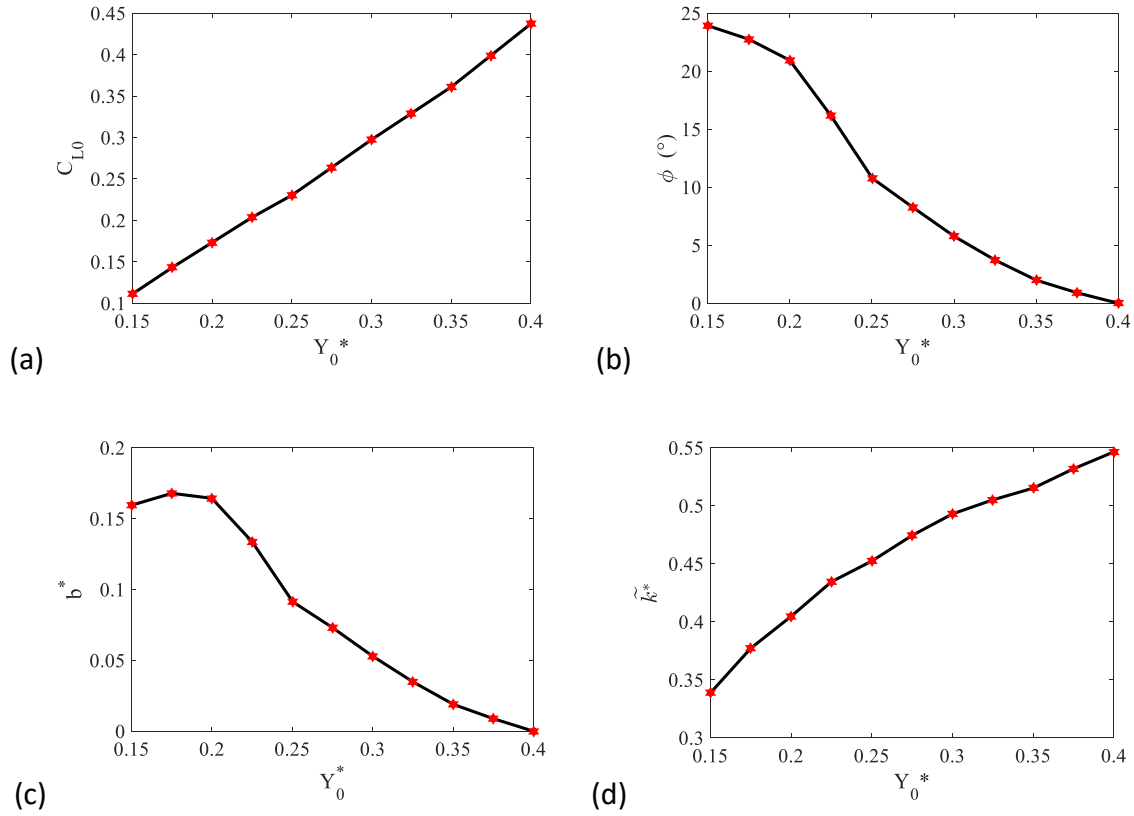


Fig. 4-4 Results of lock-in forced oscillation with different amplitudes at $f_c^* = 0.15$.

4.4 Prediction and simulation of free motion of a body

Form the discussion in section 4.1, when the damping b^* and stiffness k^* of the cylinder are given through Eqs. (4-7) and (4-8), its free motion will be the same as the forced motion. Here free oscillations with $m^* = 1 - 500$, $b^* = 0 - 1.580$ and $k^* = 1 - 800$ have carried out to verify the mathematical analysis in section 4.1. A lock-in case under forced motion at $Y_0^* = 0.556$ and $f_c^* = 0.2$ is chosen as an example. From the results in the above section, we have $\tilde{k}^* = 1.501$ and $b^* = 0$. When $m^* = 1$, the value of k^* is equal to $4\pi^2 m^* f_c^{*2} + \tilde{k}^* = 3.080$ predicted by forced results based on Eq. (4-7), which are used together with $\zeta = 0$. Then, C_{L0} , Y_0^* and f_c^* are obtained by simulation for the free motion ($m^* = 1$, $k^* = 3.080$, $b^* = 0$), shown in Table 4-3. The comparison with the forced motion is also given in Table 4-4. It can be seen that results from the two simulations are virtually the same. This verifies the derivation in section 4.1.

Table 4-3 Comparison of results predicted by forced oscillation ($\phi = 0^\circ$) with that from the real free vibration with $(m^* + M_p^*)\zeta_c = 0$

Case	C_{L0}	Y_0^*	f_c^*	f_n^*
Forced motion ($\phi = 0^\circ$)	1.669	0.556	0.2	-
Free motion ($m^* = 1, k^* = 3.080, b^* = 0$)	1.678	0.556	0.2	0.209
Free motion ($m^* = 5, k^* = 9.397, b^* = 0$)	1.694	0.556	0.2	0.203
Free motion ($m^* = 250, k^* = 396.3, b^* = 0$)	1.687	0.557	0.2	0.200
Free motion ($m^* = 500, k^* = 791.1, b^* = 0$)	1.670	0.556	0.2	0.200

Further from the discussion in section 4.1, in the equivalent free motion at given f_c^* and Y_0^* , the choice of b^* is fixed based on Eq. (4-8). However, the choice of m^* and k^* are not unique. If they vary based on Eq. (4-7), the motion of the body will be the same. Here we propose the definition of the damping ratio $\zeta_c = b/2(m + M_p)\omega_c$, which is based on the motion frequency of the body ω_c , instead of the natural frequency of the body ω_n . The motion may then be same for mechanical systems when (1) $(m^* + M_p^*)\zeta_c$ is same and (2) the relationship between m^* and k^* satisfies $\tilde{k}^* = k^* - 4\pi^2 m^* f_c^{*2}$ from Eq. (4-7) predicted using the forced motion with given f_c^* . This may be verified numerically below.

In practical problems, m^* is of order 1~10 in hydrodynamic engineering, which is often regarded as low mass, while $m^* = O(100)$ in aerodynamic applications, which is usually regarded as high mass. Thus, simulations are made with various body mass $m^* = 1, 5, 250, 500$ and the corresponding stiffness $k^* = 3.080, 9.397, 396.3, 791.1$ obtained from Eq. (4-7). Damping b^* is equal to zero, and thus $(m^* + M_p^*)\zeta_c$ is still equal to zero. In such a case, $\tilde{k}^* = C_{L0}/2Y_0^*$ is the same as \tilde{k}_0^* adopted by [Shiels et al. \(2001\)](#) based on free motion without damping. C_{L0} , Y_0^* , f_c^* and f_n^* from simulations for free oscillations with

various body masses are shown in Table 4-4. For $m^* = O(100)$, the natural frequency of cylinder f_n^* is much closer to f_c^* and can be regarded as $f_n^* = f_c^*$, which is similar to that under lock-in free motion for the high mass given by [Feng \(1968\)](#) and [Williamson and Govardhan \(2004\)](#). For $m^* = O(1\sim 10)$ at small mass, the natural frequency is more likely to be different from that f_c^* . However, in these cases, it can be seen that C_{L0} and Y_0^* from various body masses are virtually same, or the motions have no difference for larger or smaller m^* .

Table 4-4 Maximum lift coefficient, amplitude of the cylinder motion, the oscillation frequency and natural frequency of cylinder under free motion at $(m^* + M_p^*)\zeta_c = 0.639$ with various body masses

Case	C_{L0}	Y_0^*	f_c^*	f_n^*
Free motion ($m^* = 1, k^* = 1.764, b^* = 1.580$)	0.384	0.1	0.177	0.158
Free motion ($m^* = 5, k^* = 6.712, b^* = 1.580$)	0.383	0.1	0.177	0.171
Free motion ($m^* = 250, k^* = 309.7, b^* = 1.580$)	0.384	0.1	0.177	0.177
Free motion ($m^* = 500, k^* = 618.9, b^* = 1.580$)	0.382	0.1	0.177	0.177

We then consider a case with different frequency $f_c^* = St = 0.177$ and non-zero damping. At $Y_0^* = 0.1$, we have $\tilde{k}^* = 1.055$ and $b^* = 1.580$ from results in above section. Simulations are made with various body mass $m^* = 1, 5, 250, 500$, together with the structural stiffness $k^* = 1.764, 6.712, 309.7, 618.9$ based on Eq. (4-7). $(m^* + M_p^*)\zeta_c$ is always constant, equal to 0.639. C_{L0}, Y_0^*, f_c^* and f_n^* from simulations for free oscillations with various body masses are given in Table 4-4. For the high mass $m^* = O(100)$, the natural frequency of cylinder f_n^* is quite close to f_c^* and it can be regarded as $f_n^* = f_c^*$, which is expected and is similar to that in the previous case in Table 4-3. For the low mass $m^* = O(1\sim 10)$, the difference between f_n^* and f_c^* is larger than that with high mass. At $m^* = 1$, the ratio of the oscillation frequency to the natural frequency of the cylinder is $f^* \approx 1.2$. From the table, it can be seen that C_{L0} as

well as Y_0^* from various body masses are virtually same. Together with Table 4-3, it confirms numerically the derivation in section 4.1.

4.5. Predicting the free motion from the $b^* - \tilde{k}^*$ diagram of the forced motion

In order to predict the response of free motion based on forced motion, [Staubli \(1983\)](#) plotted the contours of C_{L0} and ϕ on the $f_c^* - Y_0^*$ plane and [Morse and Williamson \(2009a\)](#) gave the contours of $C_{L0} \sin \phi$ and M_e^* on the $\lambda^* - Y_0^*$ plane, where $\lambda^* = 1/f_c^*$ was regarded as the nondimensionalized wavelength. For a mechanical system with given m^* , k^* and b^* , its free motion results can be found from the $f_c^* - Y_0^*$ or $\lambda^* - Y_0^*$ plane of forced motion. In fact, at different f_c^* (or λ^*) and Y_0^* , $C_{L0} \sin \phi$ and M_e^* can be obtained from the diagram. If the equation of $b^* = \frac{\lambda^{*2} C_{L0} \sin \phi}{8\pi^2 Y_0^*} \sqrt{\frac{k^*}{m^* + M_p^*}}$ is satisfied, the cylinder will then oscillate with the frequency f_c^* and amplitude Y_0^* .

In the present paper, $b^* - \tilde{k}^*$ diagram from the forced motion results at $Y_0^* = 0.05 - 0.55$ and $f_c^* = 0.14 - 0.2$ is developed. Based on Eqs. (4-8) and (4-9), at given frequency, b^* and \tilde{k}^* will vary with amplitude Y_0^* . Their results can be put on the $b^* - \tilde{k}^*$ plane to form a curve. Curves at other frequencies can also be plotted as shown in Fig. 4-5. Similarly, at given amplitude, b^* and \tilde{k}^* will vary with oscillation frequency f_c^* . The contours of Y_0^* on the $b^* - \tilde{k}^*$ plane can also be given in Fig. 4-5. It can be found from the figure that when b^* is small, the horizontal line intersects almost all f_c^* lines. It means that there is a larger range of \tilde{k}^* , in which the lock-in free motion with different frequencies may be possible. When $f_c^* < 0.181$, the value of \tilde{k}^* decreases with the increase of b^* at a given f_c^* . When $f_c^* > 0.181$ except $f_c^* = 0.200$, the value of \tilde{k}^* increases with b^* at a given f_c^* . When $f_c^* = 0.200$, the value of \tilde{k}^* increases first and then decreases with b^* . Thus, at a given b^* , the $f_c^* = 0.200$ line could be intersected twice. This implies that at two different \tilde{k}^* , the motion frequency will be the same. The values of Y_0^* at these two \tilde{k}^* , however, will be different. Y_0^* at the smaller \tilde{k}^* is larger than that at the larger \tilde{k}^* . For instance, when $b^* = 0$, values of the motion frequency

at $\tilde{k}^* = 1.501$ and 3.338 are the same, $f_c^* = 0.200$, while $Y_0^* = 0.556$ at $\tilde{k}^* = 1.501$ and $Y_0^* = 0.250$ at $\tilde{k}^* = 3.338$.

The diagram in Fig. 4-5 can provide an effective means to predict the response of a given mechanical system. For a mechanical system with damping b^* , a horizontal line with the same b^* can be drawn on the $b^* - \tilde{k}^*$ plane. It will intersect the f_c^* curves of different values. At each intersection of f_c^* , \tilde{k}^* can be obtained based on this f_c^* , which is compared with the real one $k^* - 4\pi^2 m^* f_c^{*2}$. If they are not the same, \tilde{k}^* will be obtained at the next f_c^* and this process continues. When, at a certain f_c^* , $\tilde{k}^* = k^* - 4\pi^2 m^* f_c^{*2}$ is satisfied, it means that the mechanical system will oscillate with frequency f_c^* . In such a case, the corresponding Y_0^* at this f_c^* can be obtained at the point with known coordinates (b^*, \tilde{k}^*) on the $b^* - \tilde{k}^*$ plane, from the Y_0^* counter lines. If there is no satisfied \tilde{k}^* in Fig. 4-5, it means that the motion will be no longer in the region of lock-in.

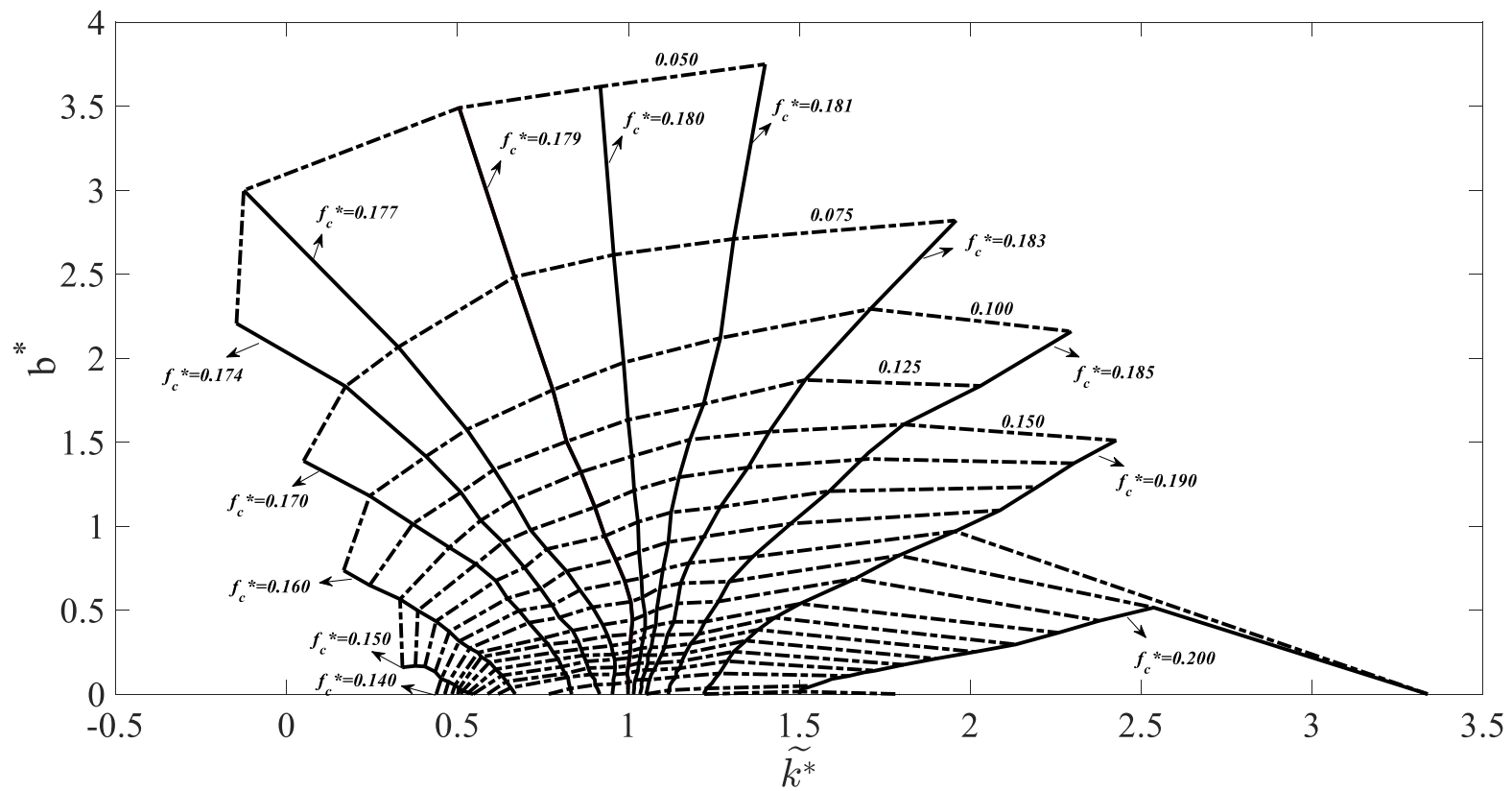


Fig. 4-5 $b^* - \tilde{k}^*$ diagram at various f_c^* and Y_0^* (solid lines denote values of $f_c^* = 0.14 - 0.2$ and dashed-dotted lines $Y_0^* = 0.050 - 0.55$ with 0.025 increment).

We may use the $b^* - \tilde{k}^*$ plane to plot curves to show how motion of a body of mass m^* changes with stiffness \tilde{k}^* at different b^* . It should be noted that Y_0^* and f_c^* will not vary, when m^* changes, if \tilde{k}^* follows its change based on Eq. (4-7), or the free motion will be the same. We may choose $m^* = 10$ and results are provided in Fig. 4-6. In some of the previous studies, the reduced velocity U^* is often used as a horizontal axis instead of k^* , and thus it is also shown in Fig. 4-6. It can be seen in the figure that when k^* increases (U^* decreases), Y_0^* and f_c^* increase first over a large range. For large b^* , they will be rising within the whole lock-in region. For small b^* , they will reach a peak and then decrease. In particular at $b^* = 0$, they reach peak at $k^* \approx 17$ and then drop sharply, which is very close to the end of lock-in region. With a small increase of k^* , the value of Y_0^* can drop from 0.556 to 0.250 and f_c^* from 0.210 to 0.200, which is similar to that under lock-in free motion with zero damping in the laminar flow regime ($60 < Re < 200$) given by [Prasanth and Mittal \(2008\)](#). The main reason for this jump may be because of a change in two different wake patterns. Vortex counters at $Y_0^* = 0.556$ ($f_c^* = 0.210$) and $Y_0^* = 0.250$ ($f_c^* = 0.200$) shown in Fig. 4-7(a) and (b), respectively. Even though these wake patterns both have a single vortex shed from each side of the cylinder during a cycle of vortex shedding, their vertical spacings of the vortices are different. In Fig. 4-7(a), there is a clear gap between rows, while the much smaller gap in Fig. 4-7(b) suggests that the effect of vortices is more like that of a single row. From Fig. 4-6, $Y_0^* = 0.556$ is the largest possible free motion amplitude for the cylinder in the whole ranges of stiffness and damping, with the lock-in region. The corresponding motion frequency $f_c^* = 0.200$, larger than $f_v^* = 0.177$ of the vortex shedding frequency of a fixed cylinder.

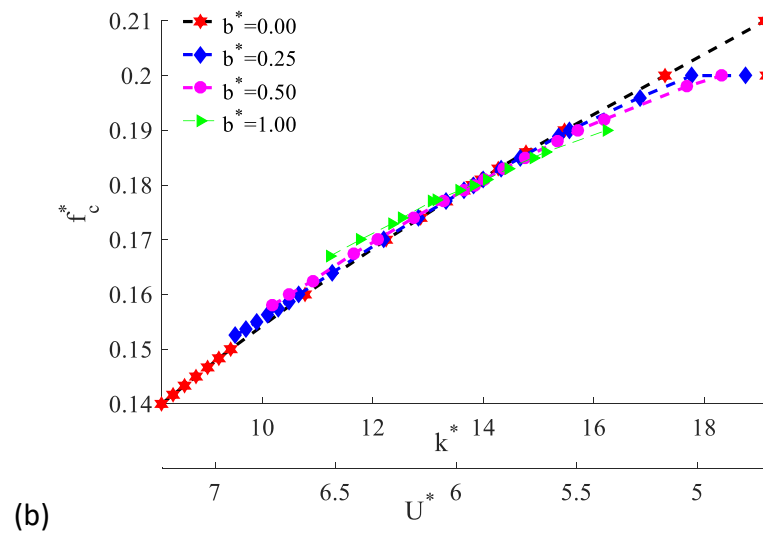
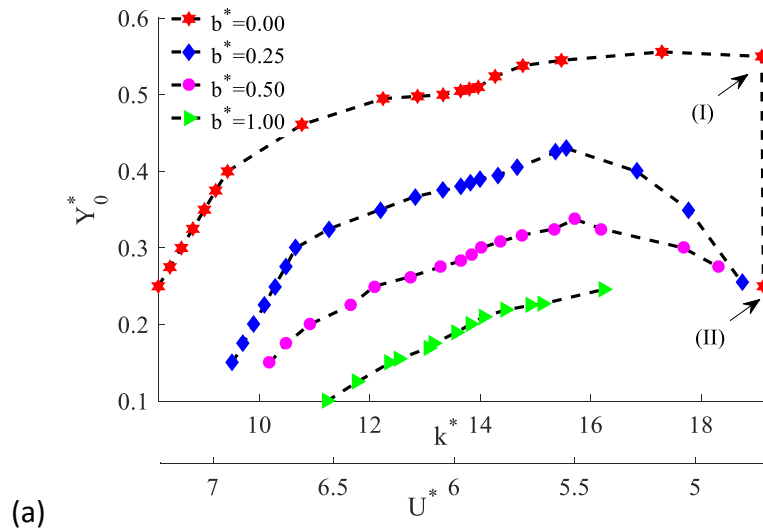
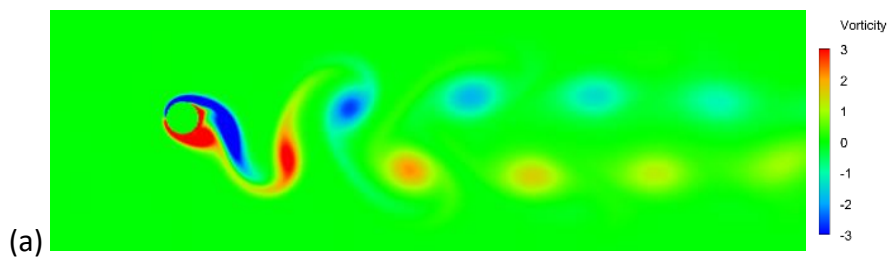


Fig. 4-6 Amplitude and frequency of free motion against k^* in the lock-in region predicted from the forced motion results with $m^* = 10$.



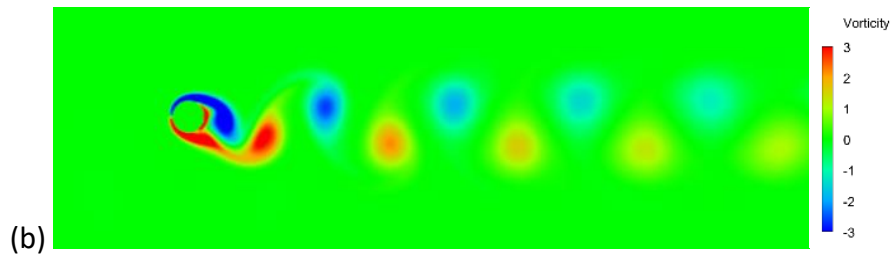


Fig. 4-7 Vortex contour at the maximum value of lift coefficient for (a) the point (I) and (b) the point (II) shown in Fig. 4-6.

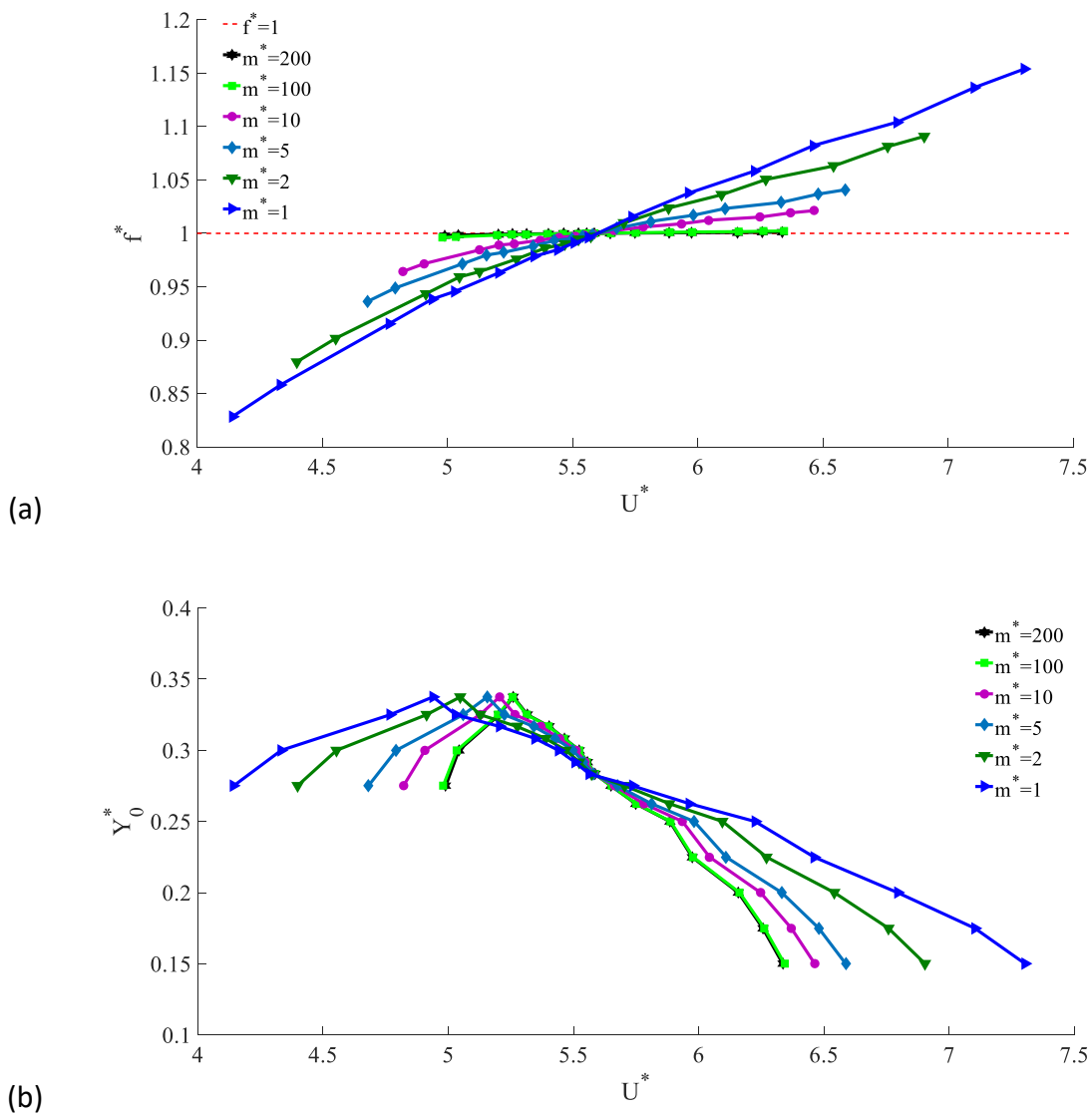


Fig. 4-8 The ratio between body motion frequency and its natural frequency as well as the motion amplitude in the lock-in region predicted from the forced motion results with $b^* = 0.5$.

0.5.

For a mechanical system, it would also be interesting to see how the motion of the cylinder will change with k^* for each given m^* , when b^* is fixed. In such a case, $f_n^* = \frac{1}{2\pi} \sqrt{\frac{k^*}{m^* + M_p^*}}$ will vary, with k^* . We notice that the range of \tilde{k}^* for the lock-in in Fig. 4-5 is the same for different mass. Then, when m^* changes from 1 to 200, the corresponding range of k^* will also change in a similar magnitude based on Eq. (4-7). Thus, instead of using k^* as a horizontal axis, we use the reduced velocity $U^* = 1/f_n^*$ in Fig. 4-8, in which the variation of f^* and that of Y_0^* with m^* are provided. It can be seen that when m^* is fixed, f^* will increase with U^* . In particular, $f^* < 1$ at smaller U^* and $f^* > 1$ at larger U^* . When m^* increases, the slope of f^* becomes milder, f^* is closer to unity and the largest possible free motion amplitude occurs closer to $f^* = 1$. When m^* reaches 100, the slope of f^* is almost zero and $f^* \approx 1$. In this sense, the peak amplitude is also at $f^* \approx 1$. It may be also interesting to see that with the increase of m^* , the range of U^* becomes smaller in the lock-in region, which is similar to that observed by [Govardhan and Williamson \(2000\)](#) in free motion simulations.

Fig. 4-6 has given the results for the whole range of stiffness at different dampings, within which lock-in occurs. This implies that outside the range, the free motion is no longer expected to exhibit the behaviour of lock-in defined in section III. Thus, for $m^* = 10$, we take a higher stiffness $k^* = 26$ at $b^* = 0$, which is beyond the lock-in region in Fig. 4-6. Fig. 4-9 shows lift coefficient and displacement from the free motion simulation. Their frequency spectra are also provided, similar to that in Jiao and Wu³². Similarly, results for $m^* = 10$ and $b^* = 0$ at lower stiffness $k^* = 5$ outside the lock-in region are displayed in Fig. 4-10. We may notice that in both cases, the motion frequency has two discrete components. The one with the larger amplitude is in fact at $f_c^* = St$, and the other with the smaller amplitude is at $f_c^* = f_n^* = \frac{1}{2\pi} \sqrt{\frac{k^*}{m^* + M_p^*}}$. This means that the cylinder is responding with oscillation at the natural frequency and at a vortex shedding frequency when it is fixed. It can be seen that C_L and Y^* have the same frequency components. In fact, in some previous studies on free motion, this was often regarded within the lock-in region, in which the frequencies of the lift force match those of body oscillation ([Sarpkaya, 1995](#); [Williamson and Govardhan, 2004](#)). Here these two cases cannot be captured by using the results in Fig. 4-6, as the cylinder is forced into motion

at a single frequency. It is therefore important to emphasize the $b^* - \tilde{k}^*$ diagram in Fig. 4-6 which covers only the range of lock-in defined in section 4.1.

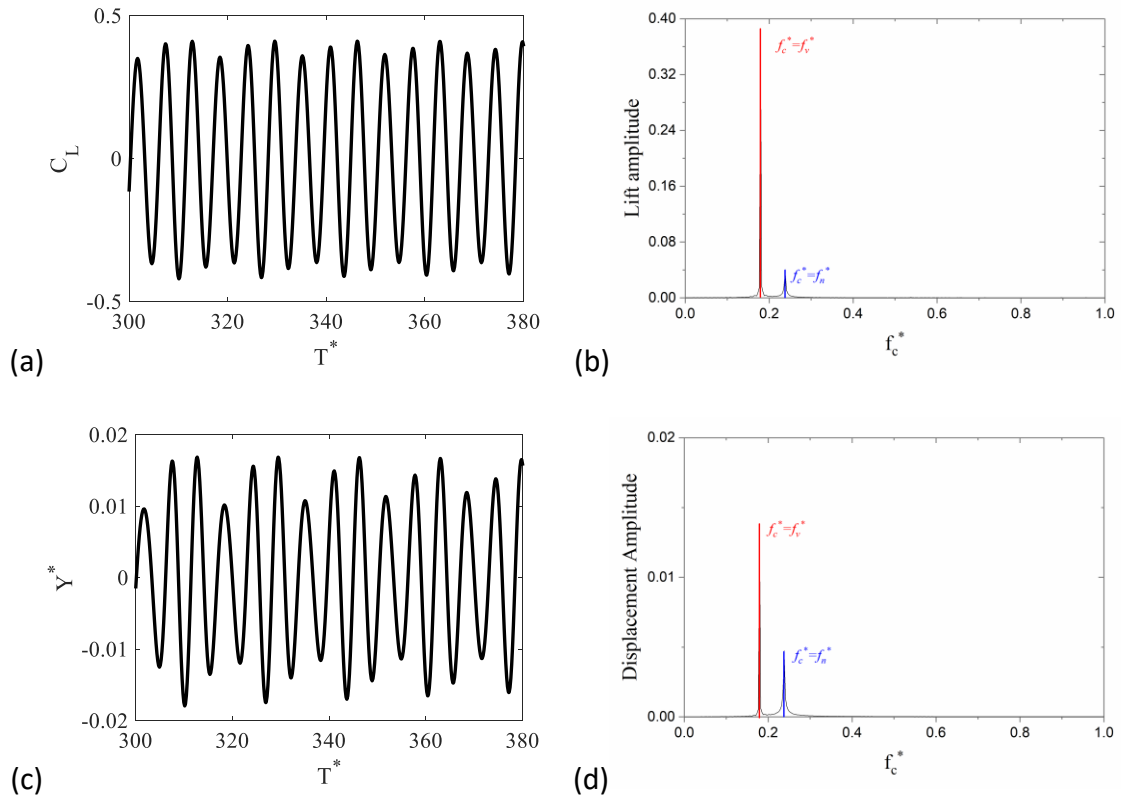
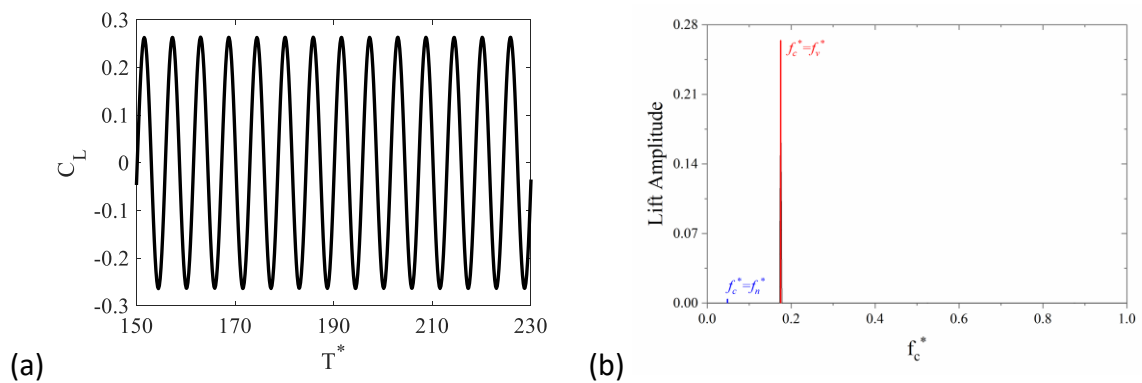


Fig. 4-9 Lift coefficient and displacement as well as their amplitude spectra from the free motion simulations at $m^* = 10$, $b^* = 0$ and $k^* = 26$.



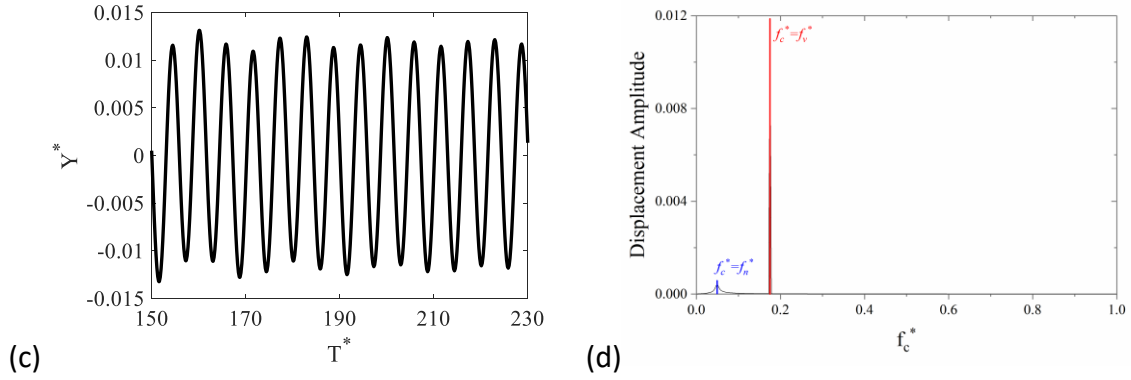


Fig. 4-10 Lift coefficient and displacement as well as their amplitude spectra from the free motion simulations at $m^* = 10$, $b^* = 0$ and $k^* = 5$.

4.6 Summary

The equivalence between the sinusoidal free and forced motions in the lock-in region has been established through the mathematical analysis and confirmed by numerical results. Also, the characteristics of the free motion have been investigated based on the lock-in forced motion. From the results, the following conclusions can be drawn.

1. When a body of mass m_1 , stiffness k_1 and damping b_1 is found to be in sinusoidal motion with frequency ω_c and amplitude Y_0 , its motion will be the same at m_2 , k_2 and b_2 if $m_2 - m_1 = (k_2 - k_1)/\omega_c^2$ and $b_2 = b_1$. This is valid even when ω_c is away from the natural frequency ω_n . When $\omega_c/\omega_n = 1$ this in fact reduces to well known result that at resonance motion amplitude will depend on only mass-damping parameter $(m + M_p)\zeta$.
2. For a body of mass m , added mass M_p and damping b , the damping ratio may be redefined as $\zeta_c = b/2(m + M_p)\omega_c$, using the motion frequency ω_c of the body instead of its natural frequency ω_n . With such a definition, the sinusoidal free motion of the body depends only on the combined mass-damping parameter $(m + M_p)\zeta_c$, not on them separately. It remains to be true at both high and low mass regions provided mass changes follows the pattern in 1 above. When $\omega_n = \omega_c$, this once again becomes the existing well-known result at resonance.
3. A $b^* - \tilde{k}^*$ diagram based on the forced motion results has been established. For a body of mass m , stiffness k and damping b , the diagram can be used to predict whether the body will

undergo sinusoidal free motion, and subsequently predict the motion amplitude and frequency.

Chapter 5

Effect of Reynolds number on VIV amplitude branches with turbulence model

After investigating the effect of mass-damping parameter in Chapter 4, the effect of Reynolds number on curves of the motion amplitude of a low mass cylinder in the turbulent range will be investigated systematically in this chapter. Turbulence model based on large eddy simulation will be used as the Reynolds number up to 13000 will be consider. Multi-block model is also adopted to improve the accuracy and the computational efficiency. The content of this chapter has been accepted by *Journal of Fluids and Structures*.

5.1 Free motion of a body

The nondimensionalized form of the governing equation of free motion based on ρ , u_0 and D can be written as

$$m^* \ddot{Y}^* + \frac{4\pi\zeta(m^* + M_p^*)}{U^*} \dot{Y}^* + \frac{4\pi^2(m^* + M_p^*)}{U^{*2}} Y^* = \frac{C_L}{2}. \quad (5-1)$$

For a fixed cylinder, $Y^* = 0$. C_L will be only a function of Reynolds number including its amplitude C_{L0} and frequency St , or

$$C_L = C_L(Re), \quad (5-2)$$

$$C_{L0} = C_{L0}(Re), \quad (5-3)$$

$$St = St(Re). \quad (5-4)$$

As discussed in section 1.2.3, in the sub-critical range ($Re = 300 - 2 \times 10^5$), St is almost constant with a value of 0.2 (Williamson, 1996; Sumer & Fredsoe, 1997), and so C_{L0} is, which

is around 0.3 (Skop & Griffin, 1973; 1975), apart from the drop around $Re \approx 1600$ (Norberg, 2003).

For a cylinder in oscillation, one can expect that C_L may be affected by the motion amplitude Y_0^* and motion frequency f_c^* . Thus, Eq. (5-1) becomes

$$C_L = C_L(Y_0^*, f_c^*, Re). \quad (5-5)$$

According to Eq. (5-1), Y^* depends on the body mass, damping ratio, reduced velocity and lift coefficient, or

$$Y^* = Y^*(m^*, \zeta, U^*, C_L, T). \quad (5-6)$$

It is then obvious there is some nonlinear interaction between C_L and Y^* . In such a case, unlike that for a fixed cylinder in Eq. (5-2), C_L in Eq. (5-5) for a cylinder in oscillation may be more sensitive to Re . This will be investigated through extensive simulations below.

5.2 Verification through comparison

A sketch of the computational domain for free motions of a circular cylinder with diameter D is shown in Fig. 5-1(a). The same domain is used in the rest of this work. The incoming flow is from the left hand side of the body. The cylinder is located in the flow field. $Le = 22D$, $Ls = 5D$ and $Lr = 40D$, which is similar to that used by Pigazzini *et al.* (2018). A Dirichlet boundary condition ($\vec{u} = (u_0, 0)$) is adopted at the inflow and outlet boundaries. On the upper and lower boundaries, y -velocity and the component of stress vector along these two boundaries are prescribed zero value. Initially, the velocities at all nodes, except inflow and outlet boundaries, are set to zero. There are three levels of grids in the calculation shown in Fig. 5-1(b). The ratio of space steps between Grid 2 and Grid 1 is 2 and the ratio between Grid 3 and Grid 1 is 4. The grid parameter in Grid 1 is $s = D/\delta_x = 400$. The Mach number is taken as $M_a = 0.02$ and the Smagorinsky constant $C = 0.1$.

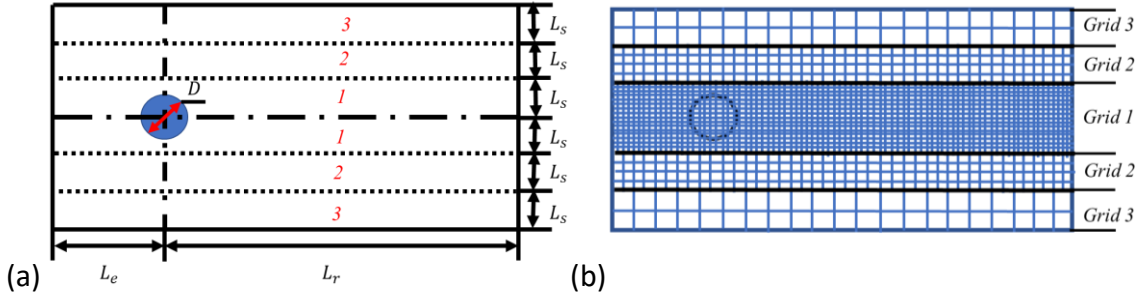
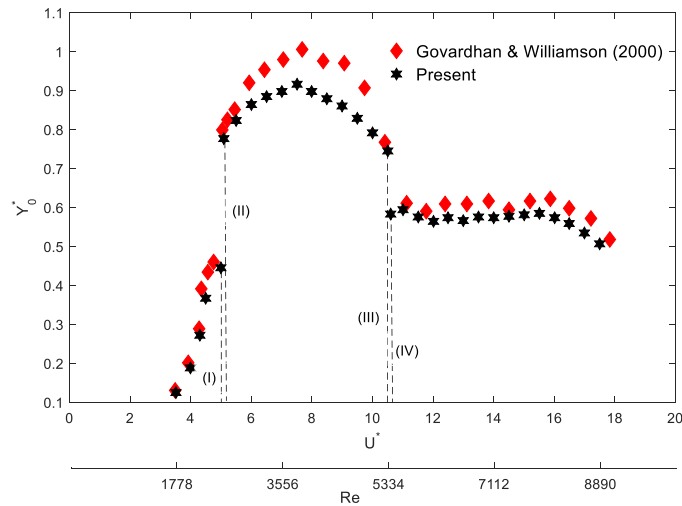


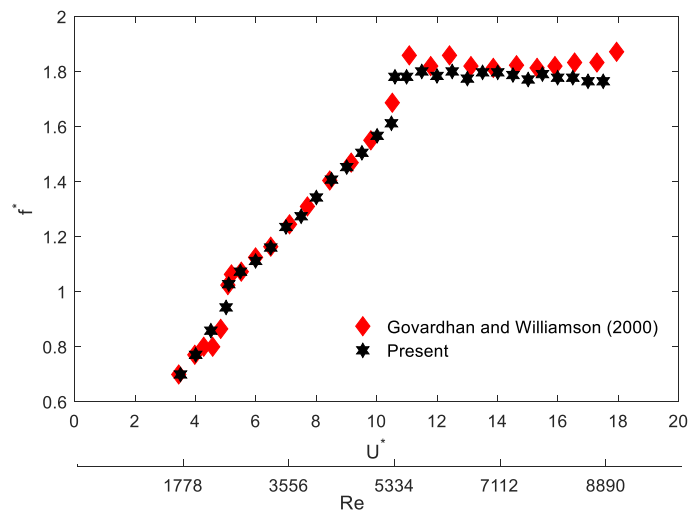
Fig. 5-1 (a) Computational configuration and (b) schematic diagram of grid levels.

To validate our method, we compare our numerical results with the experimental data from [Govardhan and Williamson \(2000\)](#) for a cylinder in free motion, with body mass $m^* = 0.935$ and damping ratio $\zeta = 0.00502$. The reduced velocity U^* varies from 3 to 24 and corresponding Reynolds number from 1524 to 12192. It is found in our simulations that lock-in where the dominant frequency of the lift coefficient is equal to that of cylinder motion occurs in the region of $U^* = 3.5 - 17.5$, which is similar to that in [Govardhan and Williamson \(2000\)](#) shown in Fig. 5-2. Spectra of cylinder motion and lift coefficient in the lock-in region are not purely sinusoidal, but still discrete, which is the same as that in [Pigazzini et al. \(2018\)](#). In addition to the dominant frequency component, there are multiple intricate frequencies in spectra. It should be noted that the definition of lock in from [Govardhan and Williamson \(2000\)](#) is adopted in this Chapter. The system is regarded as the state of lock-in when the dominant frequency of the lift coefficient is equal to that of cylinder motion. Compared with that mentioned in section 4.1, the definition of lock-in here has been extended to account for the turbulent flow effect on the result. Fig. 5-2 shows motion amplitude Y_0^* and frequency ratio $f^* = f_c^*/f_n^*$ in the lock-in region, where f_c^* is the dominant frequency of the cylinder motion. It can be seen that in the Y_0^* curve, there are two jumps and three amplitude branches, including initial ($3.5 \leq U^* \leq U_{IU}^*$), upper ($U_{IU}^* < U^* \leq U_{UL}^*$) and lower branches ($U_{UL}^* < U^* \leq 17.5$), as defined by [Khalak and Williamson \(1997\)](#). In the initial branch, with the increase of U^* , Y_0^* also increases. Further increase of U^* to U_{IU}^* , Y_0^* jumps nearly vertically from initial value to the upper branch within which the peak of the motion amplitude $Y_{0max}^* = 0.91$ is located at $U^* = 8.0$ ($Re = 4064$). As U^* continues to increase to U_{UL}^* , the transition between upper-lower branches occurs, and Y_0^* drops nearly vertically. In the present study with smaller incremental increase of U^* than that from [Govardhan and Williamson \(2000\)](#), U_{IU}^* is found to

be in the range from 5.0 to 5.1, and U_{UL}^* from 10.5 to 10.6. The result in Fig. 5-2 are generally in good agreement with those from Govardhan and Williamson (2000), although the peak of the motion amplitude $Y_{0max}^* = 0.91$ at $U^* = 0.75$ is a bit smaller than $Y_{0max}^* = 1.01$ in Govardhan and Williamson (2000). Fig. 5-3 shows displacement and lift coefficient histories at U_{IU}^* and U_{UL}^* . At the lower end of U_{IU}^* , lift coefficient and displacement are almost in phase, while at the higher end of U_{UL}^* , they become nearly anti-phase. These phenomena are consistent with that observed in the experiment by Govardhan and Williamson (2000). Fig. 5-4 shows the amplitude C_{L0} of lift coefficient in the lock-in region. It can be seen that when $U^* = U_{UL}^*$, there is also a sudden drop in C_{L0} , about from 0.70 to 0.37.



(a)



(b)

Fig. 5-2 Comparison of motion amplitude and frequency ratio between experimental data from Govardhan and Williamson (2000) and present results.

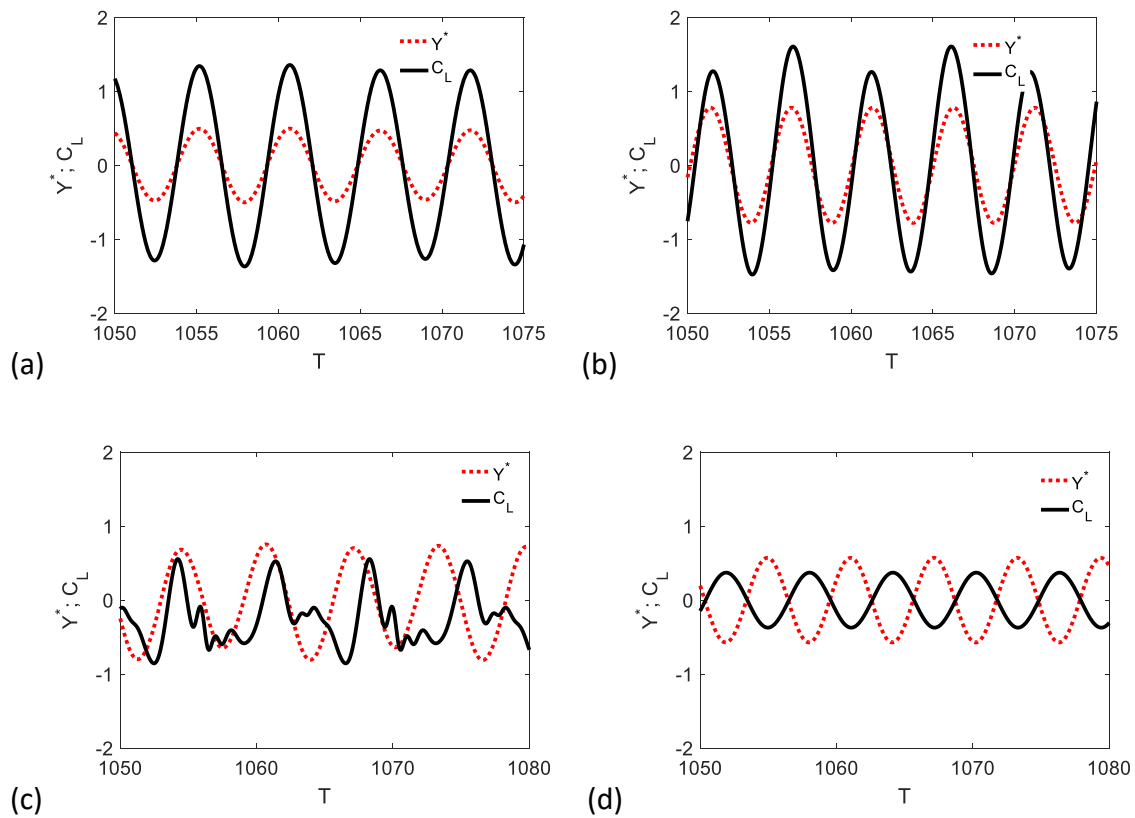


Fig. 5-3 Displacement and lift coefficient near critical reduced velocity between initial and upper branches ((a) corresponding point (I) and (b) corresponding point (II) shown in Fig. 5-2), and near that between upper and lower branches ((c) corresponding point (III) and (d) corresponding point (IV) shown in Fig. 5-2) (a) $U^* = 5.0$ ($Re = 2540$), (b) $U^* = 5.1$ ($Re = 2590$), (c) $U^* = 10.5$ ($Re = 5334$) and (d) $U^* = 10.6$ ($Re = 5385$).

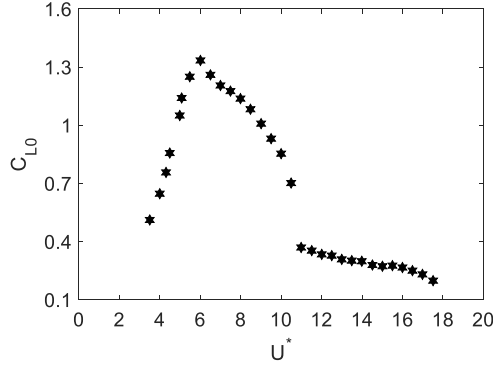


Fig. 5-4 Amplitude of lift coefficient in the region of $U^* = 3.5 - 17.5$.

5.3 Variation of body motion with reduced velocities at different fixed Reynolds numbers

If we write

$$C_L = C_{L0} \sin(2\pi f_c^* T + \phi) \text{ or } C_L = \text{Re}[i C_{L0} e^{-i(2\pi f_c^* T + \phi)}], \quad (5-7)$$

and the motion of the cylinder can then be written as

$$Y^* = Y_0^* \sin(2\pi f_c^* T) \text{ or } Y^* = \text{Re}[i Y_0^* e^{-i(2\pi f_c^* T)}], \quad (5-8)$$

where ϕ is the phase angle between the lift coefficient and cylinder motion, we can have

$$Y_0^* = \frac{U^{*2}}{8\pi^2} \sqrt{\frac{1}{[(m^* + M_p^*) - m^* f^{*2}]^2 + 4\zeta^2 (m^* + M_p^*)^2 f^{*2}}} C_{L0}. \quad (5-9)$$

In the following computations of this section, we may fix m^* and ζ , as well as Re , and vary only U^* . Eq. (5-9) shows that Y_0^* will be directly affected by the term of U^* . It will also be affected implicitly by f^* which will change with U^* . When Y_0^* and f^* change with U^* , C_{L0} will also change, which further affects Y_0^* . Therefore, there is a complex nonlinear interaction. The process of interaction will be different when Re is different. We shall undertake extensive simulations to have a better understanding of the force and motion behaviour. To investigate the effects of Reynolds number Re and reduced velocity U^* individually, Re changes with kinematic viscosity ν and U^* with natural frequency f_n in the following simulations.

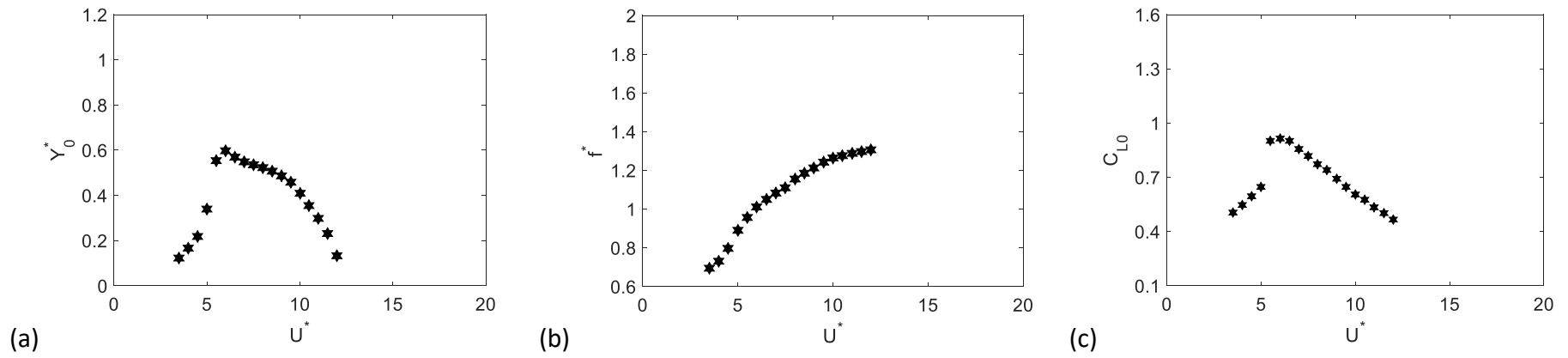


Fig. 5-5 (a) Motion amplitude, (b) frequency ratio and (c) amplitude of lift coefficient at $Re = 1778$.

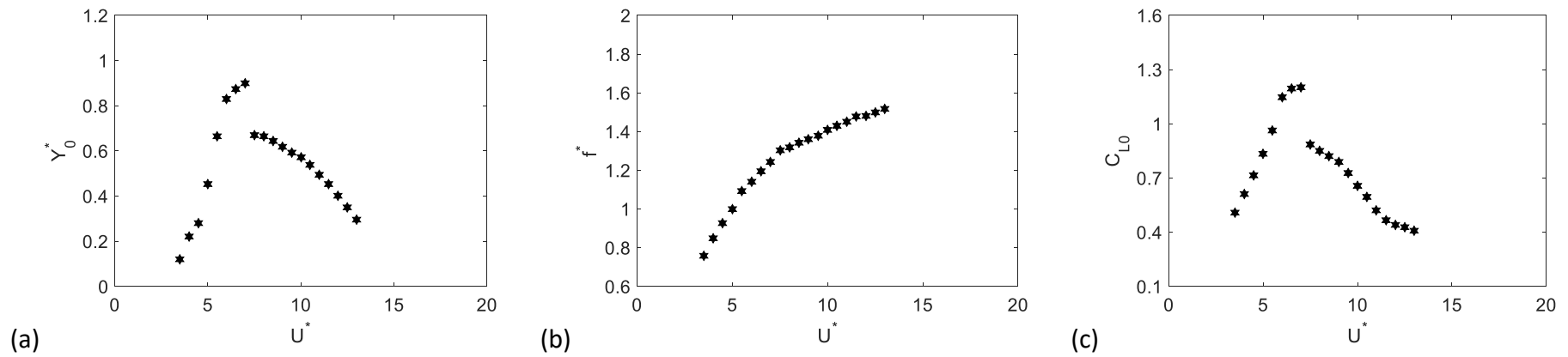


Fig. 5-6 (a) Motion amplitude, (b) frequency ratio and (c) amplitude of lift coefficient at $Re = 3556$.

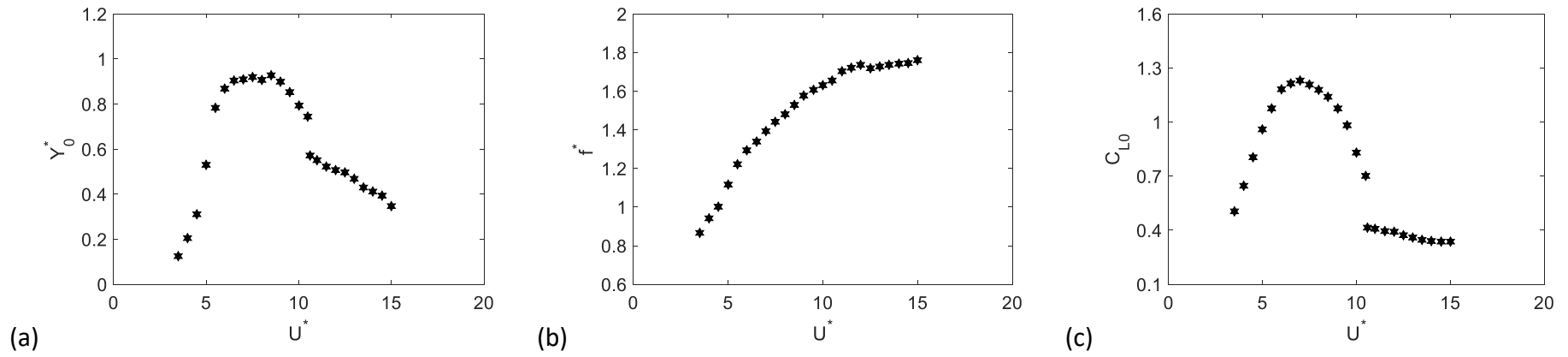


Fig. 5-7 (a) Motion amplitude, (b) frequency ratio and (c) amplitude of lift coefficient at $Re = 5334$.

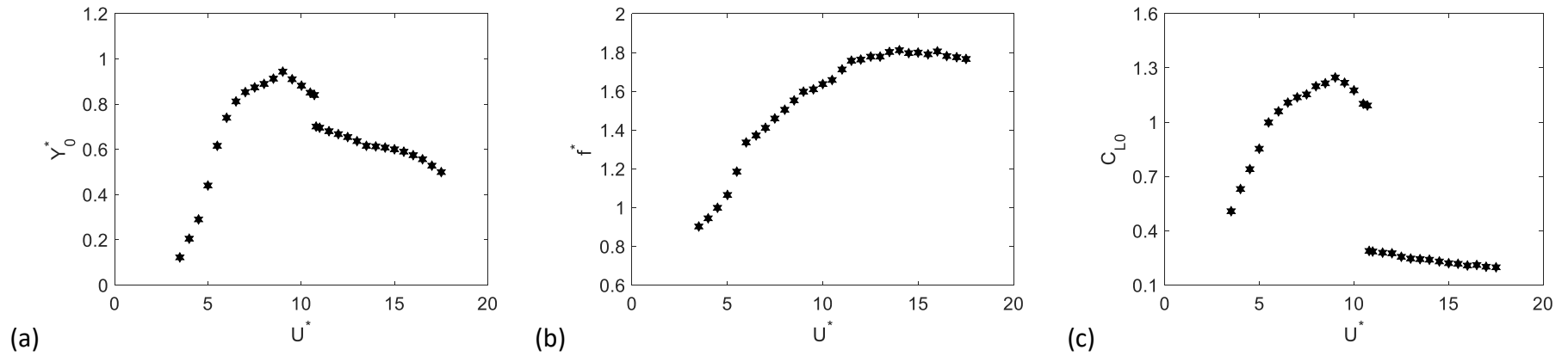


Fig. 5-8 (a) Motion amplitude, (b) frequency ratio and (c) amplitude of lift coefficient at $Re = 8890$.

We first choose $Re = 1778$ which is the low end of lock-in region in the previous case shown in Fig. 5-2, and simulations have been undertaken for reduced velocity in the range of $U^* = 3.5 - 17.5$. It is found that lock-in occurs at $U^* \leq 12.0$. Fig. 5-5 shows (a) the motion amplitude Y_0^* and (b) frequency ratio f^* in the lock-in region. Within the range of $U^* = 3.5 - 12.0$, the variation of the frequency ratio f^* is from 0.70 to 1.31. For this Reynolds number $Re = 1778$, $Y_{0max}^* = 0.59$ at $U^* \approx 6.0$ is the peak of motion amplitude in the lock-in region. It can be seen that the motion amplitude Y_0^* changes rapidly before its peak similar to that from [Wanderley and Soares \(2015\)](#), and two sides of the peak correspond to the initial and upper branches. With the increase of U^* , the motion amplitude Y_0^* in the initial branch also increases while Y_0^* in the upper branch has the opposite trend. This may be partly explained by amplitude C_{L0} of lift coefficient in Fig. 5-5(c). It can be seen that the shape of the Y_0^* curve is the similar to that of C_{L0} . When U^* increases, C_{L0} increases slowly first and then jumps to its peak value at $U^* \approx 6.0$, where Y_{0max}^* occurs. As U^* continues to increase, C_{L0} decreases.

When $Re = 3556$, simulations have been made in the range of $U^* = 3.5 - 17.5$. It is found that here lock-in occurs when $U^* \leq 13.0$, whose range is larger than that in the previous case of $Re = 1778$. Fig. 5-6 shows (a) the motion amplitude Y_0^* and (b) frequency ratio f^* in the lock-in region. The peak $Y_{0max}^* = 0.89$ at $Re = 3556$ is much larger than $Y_{0max}^* = 0.59$ at $Re = 1778$ in Fig. 5-5. It seems that with the increase of Re , the value of the peak Y_{0max}^* also increases, which was also observed in [Klamo et al. \(2005\)](#) and [Govardhan & Williamson \(2006\)](#), whose work focused only on the effect of Re on Y_{0max}^* . In addition, for $Re = 3556$, the free motions against reduced velocity are very different from that in the previous cases in Fig. 5-5. Here, with the increase of U^* , Y_0^* also increases first. At $U^* \approx 5.0 - 6.0$, it increases rapidly and at $U^* \approx 7.0$, it reaches its peak value in the lock-in region. The motion amplitude Y_0^* drops steeply after its peak, while it drops smoothly at $Re = 1778$. As U^* further increases, Y_0^* still decreases. It means that there is a critical value U_{UL}^* which connects the upper and lower branches, instead of U_{IU}^* in the previous case. At $Re = 3556$, the sudden drop at U_{UL}^* is similar to that in Fig. 5-2. But here the drop occurs at the peak, while it in Fig. 5-2 is away from the peak location. There is a rapid variation of Y_0^* before its peak. However, this is not like the almost vertical jump in Figs. 5-2 and 5-5 before Y_0^* arrives to its peak. Fig. 5-6(c) shows the amplitude of lift coefficient in the lock-in region. It can be seen that the shape of the Y_0^* curve

may be similar to that of C_{L0} in the lock-in region, which is also found at $Re = 1778$ in Fig. 5-5(c).

Simulations at $Re = 5334$ have been carried out in the range of $U^* = 3.5 - 17.5$. It is found that when Reynolds number is fixed at $Re = 5334$, lock-in occurs when $U^* \leq 15.0$, whose range is larger than that in the previous two cases of $Re = 1778$ and 3556 . Fig. 5-7 shows (a) the motion amplitude Y_0^* and (b) frequency ratio f^* in the lock-in region. At $U^* = 8.0$, $Y_{0max}^* = 0.92$ is the peak of motion amplitude in the lock-in region. Compared with the two previous cases at $Re = 1778$ and 3556 , there is an increase in the value of reduced velocity where the peak Y_{0max}^* occurs. At $Re = 5334$, there is still a critical value, U_{UL}^* where Y_0^* drops nearly vertically from upper branch to lower branch, similar to that in the previous case of $Re = 3556$. The drop at $U_{UL}^* = 10.5 - 10.6$ does not occur at the peak, which is similar to that in Fig. 5-4 and is different from that in Figs. 5-5 and 5-6. Fig. 5-7(c) shows the amplitude of lift coefficient in the lock-in region. Here, the peak of C_{L0} is at $U^* \approx 7.0$ smaller than $U^* = 8.0$ where Y_{0max}^* occurs, which is different from that in $Re = 1778$ and 3556 . It may be because within about the range of $U^* = 7.0 - 8.0$, the amplitudes of C_L at more frequency components become visible and significant, even though the C_L history is still periodic with respect to time.

We also provide the case in the range of $U^* = 3.5 - 17.5$ at $Re = 8890$ which is the high end of lock-in region in the previous case shown in Fig. 5-2. At this Reynolds number, lock-in is found when $U^* \leq 17.5$. Compared with previous cases from Fig. 5-5 to Fig. 5-8, the lock-in range here is larger, or with the increase of Re , the range of lock-in also increases. Fig. 5-8 shows (a) the motion amplitude Y_0^* and (b) frequency ratio f^* in the lock-in region. At $U^* = 9.0$, $Y_{0max}^* = 0.94$ is the peak of motion amplitude in the lock-in region. There is a critical value, $U_{UL}^* = 10.7 - 10.8$, connecting upper and lower branches. Here a sudden drop occurs after the peak of motion amplitude, which is similar to that in the previous case of $Re = 5334$. After the sudden drop, the decrease of Y_0^* at $Re = 8890$ is slower than that at $Re = 5334$. From the analysis of the curves of Y_0^* in Fig. 5-5 – Fig. 5-8, it can be seen that none of them is similar to that in Fig. 5-2. It suggests that the behaviour in Fig. 5-2 is due to both U^* and Re ,

not just U^* as assumed. The effect of Re on free motion should be considered. Fig. 5-8(c) shows the amplitude C_{L0} of lift coefficient in the lock-in region. It is interesting to see that at $Re = 8890$, the value of C_{L0} after the sudden drop is smaller than that with the same U^* at $Re = 5334$.

5.4 Body motion at U_{IU}^* and U_{UL}^* shown in Fig. 5-2

From the discussion on section 5.3, it can be found that none of the Y_0^* curves is similar to that in Fig. 5-2. It means that the behaviour in Fig. 5-2 is due to variations of both U^* and Re , not just U^* only, as assumed. In order to have some insight into the effect of Re on the jump of the Y_0^* curve, we will run further simulations at values of Re corresponding to positions of two jumps in Fig. 5-2. The body mass and the damping ratio are the same as those used in Fig. 5-2, or $m^* = 0.935$ and $\zeta = 0.00502$.

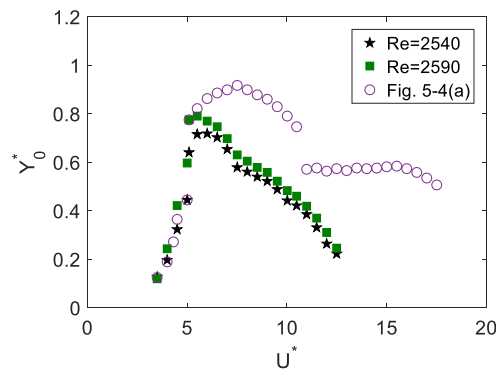


Fig. 5-9 Motion amplitude at $Re = 2540$ and $Re = 2590$ as well as that from Fig. 5-2(a).

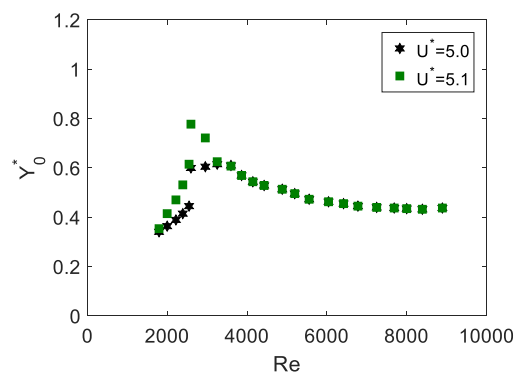


Fig. 5-10 Motion amplitude at $U^* = 5.0$ and $U^* = 5.1$.

The first jump in Fig. 5-2 occurs at $U_{IU}^* = 5.0 - 5.1$ (or $Re = 2540 - 2590$), and thus cases at $Re = 2540$ and $Re = 2590$ are chosen. Fig. 5-9 shows the motion amplitude Y_0^* against U^* at $Re = 2540$ and 2590 . It can be seen that for $Re = 2540$ and 2590 , the curves of Y_0^* against U^* are very close and their shapes similar to that from the case with $Re = 1778$. There is still one critical value U_{IU}^* connecting the initial and upper branches. For $Re = 2540 - 2590$, U_{IU}^* is in the range from 5.0 to 5.1 similar to that of the first jump shown in Fig. 5-2. Fig. 5-10 shows Y_0^* against Re at $U^* = 5.0$ and $U^* = 5.1$. It can be found that the curves of the Y_0^* at $U^* = 5.0$ and $U^* = 5.1$ are generally close. Both have a nearly vertical jump at $Re_{IU} = 2540 - 2590$, where there is an obvious difference between the two curves. It means that when $Re = 2540 - 2590$ and $U^* = 5.0 - 5.1$, the value of Y_0^* is sensitive to both the reduced velocity U^* and Reynolds number Re , or Y_0^* increases sharply with a small change of U^* or Re . Therefore, the first jump in Fig. 5-2 is very much related to variations of both U^* and Re .

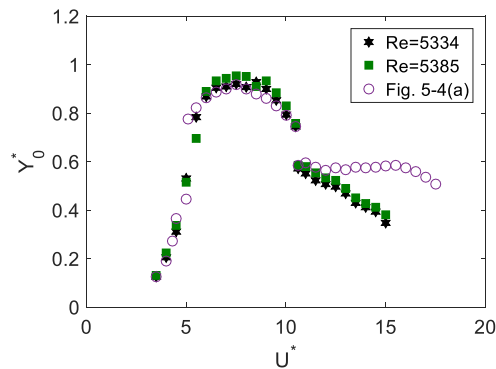


Fig. 5-11 Motion amplitude at $Re = 5334$ and $Re = 5385$.

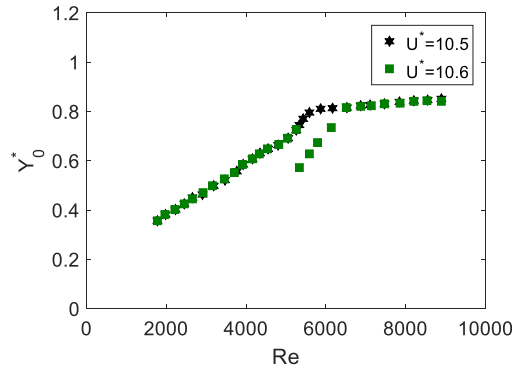


Fig. 5-12 Motion amplitude at $U^* = 10.5$ and $U^* = 10.6$.

Fig. 5-17 shows Y_0^* against U^* at $Re = 5334$ and 5385 where the second jump in Fig. 5-2 occurs. The curve of Y_0^* at $Re = 5385$ is quite close to that at $Re = 5334$. These two curves have two branches, upper and lower branches connected by U_{UL}^* , which is approximately between 10.5 and 10.6. Even though both have only one nearly vertical jump, they are quite close to U_{UL}^* in Fig. 5-2. Fig. 5-12 shows Y_0^* against Re at $U^* = 10.5$ and $U^* = 10.6$. It can be seen that the curve of Y_0^* at $U^* = 10.5$ is quite different from that at $U^* = 10.6$. Based on the step of Reynolds number used in the calculation, there is only one branch of response in the Y_0^* curve at $U^* = 10.5$, while there are two branches, upper and lower branches connected by one nearly vertical drop at $U^* = 10.6$. Before the drop, the curve at $U^* = 10.6$ nearly coincides with that at $U^* = 10.5$ and both increase with Re . Y_0^* at $U^* = 10.6$ drops suddenly at a critical value of $Re = Re_{IL} = 5334$, while at $U^* = 10.5$ it continues to increase although the rate of increase is reduced. After that Y_0^* at $U^* = 10.6$ increases more rapidly and the curve then almost merges with that of $U^* = 10.5$. Thus, the difference between these two cases occurs only in a small region after the drop occurs in the case of $U^* = 10.6$. It suggests that when $Re = 5334 - 5385$ and $U^* = 10.5 - 10.6$, Y_0^* is sensitive to both the reduced velocity U^* and the Reynolds number Re . Therefore, the reason for the second jump shown in Fig. 5-2 is also related to both variations of U^* and Re . In such a case, the effect of Re on Y_0^* is significant and cannot be ignored.

5.5 Summary

The effect of Reynolds number on free motions of a cylinder in the lock-in region has been investigated through numerical simulations based on multi-block LBM together with LES as the turbulence model and IBM for the boundary condition. The focus has been on how the Reynolds number affects the motion amplitude curve against the reduced velocity, including branches and jumps. Simulations have been performed at the different Re in the range of 1524 – 121292, with the body mass $m^* = 0.935$ and the damping ratio $\zeta = 0.00502$. From the results, the following conclusions can be drawn.

When Reynolds number Re is fixed, there are generally two branches in the curve of the motion amplitude Y_0^* against the reduced velocity U^* , instead of the usual three branches (Govardhan and Williamson, 2000) when Re changes with U^* from $Re = 1524$ ($U^* = 3.0$) to $Re = 121292$ ($U^* = 24.0$). The shape of Y_0^* curve varies when Re varies. At $Re = 1778$ there are only initial and upper branches, which are connected by U_{IU}^* . When approaching U_{IU}^* from the initial branch, Y_0^* increases rapidly or nearly vertically. When $Re \geq 3556$, there are only upper and lower branches linked by U_{UL}^* , and there is no U_{IU}^* where a nearly vertical increase of Y_0^* occurs. At $Re = 3556$, the motion amplitude Y_0^* drops steeply just after its peak, which corresponds to the start of the lower branch. At $Re = 5334$, in the upper branch, with the increase of U^* , Y_0^* increases first and then drops, and thus the sudden drop occurs away from the peak of Y_0^* . At $Re = 8890$, after the sudden drop, the decrease of Y_0^* becomes slower.

In the usual motion amplitude curve (Govardhan and Williamson, 2000), Re changes with U^* . When U^* approaches U_{IU}^* from the initial branch at U_{IU1}^* and from the upper branch at U_{IU2}^* , the corresponding Reynolds numbers are Re_{IU1} and Re_{IU2} . It is found that when Re is fixed at either Re_{IU1} or Re_{IU2} , the Y_0^* curves against U^* are very close to each other. While their Y_0^* curves in the initial branches are very similar to that in Govardhan and Williamson (2000) where Re changes with U^* , they are very different when $U^* > U_{IU2}^*$. When U^* is fixed at U_{IU1}^* or U_{IU2}^* , the two Y_0^* curves against Re are very different when Re is around Re_{IU1} to Re_{IU2} . Away from this region, the curves are close. Similarly at U_{UL}^* , corresponding to U_{UL1}^* and U_{UL2}^* ,

we have Re_{UL1} and Re_{UL2} . The two Y_0^* curves against U^* at $Re = Re_{UL1}$ and $Re = Re_{UL2}$ are very close. In the upper branch, they are very close to that in [Govardhan and Williamson \(2000\)](#), where Re changes with U^* , but very different in the lower branch. When U^* is fixed, the Y_0^* curve against Re has a jump around Re_{UL1} to Re_{UL2} at $U^* = U_{UL2}^*$, but is smooth at $U^* = U_{UL1}^*$. All these show that the effect of Re on the Y_0^* curve, including the branches, is far more complex than previously thought.

Chapter 6

Conclusion and future work

The research in this thesis focuses on three aspects of VIV displayed from Chapter 3 to Chapter 5. The detailed findings for each completed work have been summarized at the end of each chapter. In this chapter, some significant conclusions are drawn from the finished studies and some suggestions are provided for the future work.

6.1 Conclusions from the finished studies

In ocean engineering, with the exploration of the marine energy and wind power farther away from land and towards deeper and deeper water, the offshore platforms have been becoming more and more complex. Thus, the understanding of VIV is significant in order to design them safely, economically and environmental friendly. This thesis has focused on the VIV mechanism based on three physical issues using an in-house code developed by D2Q9 LBM together with IBM in Chapter 2. The major contributions and findings made in this study are summarized below.

In Chapter 3, the flow past two stationary circular cylinders with the intermediate spacing $L^* = 1.5$ in different arrangements at the Reynolds number $Re = 200$ has been considered. Although there is a large amount of similar work for two bluff bodies, there has been hardly any work on systematic investigations of the fluid force components varying with alignment angles. Such result is extremely important for vortex-induced vibration, including minimizing some unwanted features of the system. The extensive results have been provided to show the nature of the fluid force at different alignment angle, as well as the vortex contour and the streamlines. When $0^\circ \leq \alpha \leq 45^\circ$, flow is always periodic with a lowest frequency St . At $\alpha = 0^\circ$, amplitudes of force coefficients on both cylinders are smaller than that on a single isolated cylinder. The main reason may be that the vortex shed from the upstream cylinder is

suppressed by the downstream cylinder and the Karman vortex street is not fully developed behind the upstream and in front of the downstream cylinder. It causes a smaller oscillatory force on the upstream cylinder. For the downstream cylinder, the incoming flow is no longer uniform and becomes fluctuating due to the “blockage” effect of the upstream cylinder. In such a case, the incoming velocity to the downstream cylinder is lower than the free stream, and thus a smaller oscillatory force is found. The lift coefficients C_L on both cylinders have components of $(2n + 1)St$ and drag coefficients C_D have $2nSt$, which is similar to that for a single cylinder. When α is non-zero, the flow configuration becomes no longer symmetry about x axis. Only the inner shear layer from the lower cylinder is deflected into the gap between the two cylinders. Thus, the mean value of the lift force is non-zero and both C_L and C_D have components nSt . As α increases, the lowest frequency becomes smaller and more frequency components become visible and significant. As a result, the oscillatory force becomes no longer sinusoidal. When $\alpha \geq 30^\circ$, the lowest frequency is no longer the dominant component. For $\alpha = 45^\circ$, the dominant frequency of the lift force on the upper cylinder is no longer same as that of the other three forces. This can be explained by the dominant frequency of the lift force on the upper cylinder related to the oscillation of the upper shear layer of the upper cylinder, whose dominant frequency is different from that of other shear layers. The dominant frequency of all other forces is related to that of the other three shear layers. The lowest frequency becomes much smaller. As St further decreases, the Fourier series will become Fourier transform. When $\alpha > 45^\circ$, the oscillation of the flow is no longer periodic and becomes unstable. At $\alpha = 60^\circ$, three distinctive frequencies of force coefficients have been observed. The lowest is the flip-flopping frequency and the second one is the dominant frequency due to wake oscillation, while the summation of these two equals to the third component. For $\alpha = 90^\circ$, the mean drag coefficients for two cylinders become similar but higher than that for a single cylinder. The lift coefficient is always positive for the upper cylinder and negative for the lower cylinder, and thus there is a repulsive force between two cylinders. Moreover, a large number of relatively high peaks have been seen in the force spectrum and the dominant force is over a relatively broad range of frequencies.

In engineering issues, such as tension leg platforms for offshore wind turbines and offshore production of oil and gas, the tensioned cables are often so long that their vibration is easy to

be excited. In such a case, large-amplitude vibration of structures may occur, especially in the lock-in region where includes the peak response. Thus, we have extended our work to the transverse motion of a cylinder in the lock-in region in Chapters 4-5. Chapter 4 first focuses on the relationship between forced oscillation and free vibration, which is a central question in the study of VIV ([Morse and Williamson, 2006](#)). The rationale of using the results from the transverse forced oscillation of a body in the lock-in region to predict the corresponding free vibration is provided based on the mathematical analysis and verified through the numerical results at $Re = 106$. It is also shown through mathematical analysis that when a body of mass m_1 , stiffness k_1 and damping b_1 is found to be in sinusoidal motion with frequency ω_c and amplitude Y_0 , its motion will be the same that at m_2, k_2 and b_2 if $m_2 - m_1 = (k_2 - k_1)/\omega_c^2$ and $b_2 = b_1$. This can be linked to the extensive study on the effect of the combined mass-damping parameter $(m + M_p)\zeta$ on the motion amplitude. It has been well known that at resonance the motion amplitude will depend only on $(m + M_p)\zeta$, no matter how m or k changes. In this thesis, this important result has been extended to other frequencies and result at resonance is a special case. When the damping ratio is redefined using the motion frequency ω_c of the body instead of its natural frequency ω_n , the sinusoidal free motion of the body depends only on the combined mass-damping parameter $(m + M_p)\zeta_c$, not on them separately. This is valid even when ω_c is away from ω_n . When $\omega_n = \omega_c$, this in fact reduces to well-known result that at resonance motion amplitude will depend on only mass-damping parameter $(m + M_p)\zeta$. Then, motion amplitude and frequency contours are plotted against the damping and stiffness components based on the results of forced motion. For a body of mass m , stiffness k and damping b , the diagram can be used to predict whether the body will undergo sinusoidal free motion, and subsequently predict the motion amplitude and frequency.

Apart from $(m + M_p)\zeta$, another important parameter influencing the motion amplitude branches is Reynolds number, which has been considered carefully in Chapter 5. The well-known three branches found by [Khalak and Williamson \(1997\)](#) have important practical significance. One of the examples is that the motion amplitude can change rapidly with a small variation of the physical parameters. Potentially large amplitude motion may lead to

structural damage. The present work is to provide a better understanding of the well-known three branches. It can help to avoid the structure to be exposed in such a risk. The turbulent flow at $Re = 1524 - 12192$ is considered, and thus methodology is refined with large eddy simulation as the turbulence model and multi-block grid method for improving the numerical efficiency and accuracy. It is well established that when the variation of Reynolds number changes with the reduced velocity, there are three branches in the motion amplitude curve of a low mass cylinder, including initial, upper and lower branches connected by two jumps. In the early studies, it was always assumed that the effect on the results was attributed to the variation of U^* rather than the Reynolds number, as pointed out by (Bearman, 2011). Thus, far fewer studies have systematically considered the effect of Reynolds number on the motion amplitude branches, which is generally neglected in discussions of motion amplitude. In this study, Reynolds number and reduced velocity are considered as independent parameters. Reynolds number Re changes with kinematic viscosity ν and reduced velocity U^* with natural frequency f_n . Detailed results are provided for the variations of motion amplitude, motion frequency and lift coefficient against the reduced velocity in the lock-in region at different fixed Reynolds numbers. The results show that at a fixed Reynolds number the motion amplitude curve has two branches. At lower range of Reynolds number calculated, there are only initial and upper branches, and at higher range, there are only upper and lower branches. Also, the motion amplitude against the Reynolds number near the jumps is studied when the reduced velocity is fixed. It shows that the values of amplitude near the jumps are very sensitive to Reynolds number.

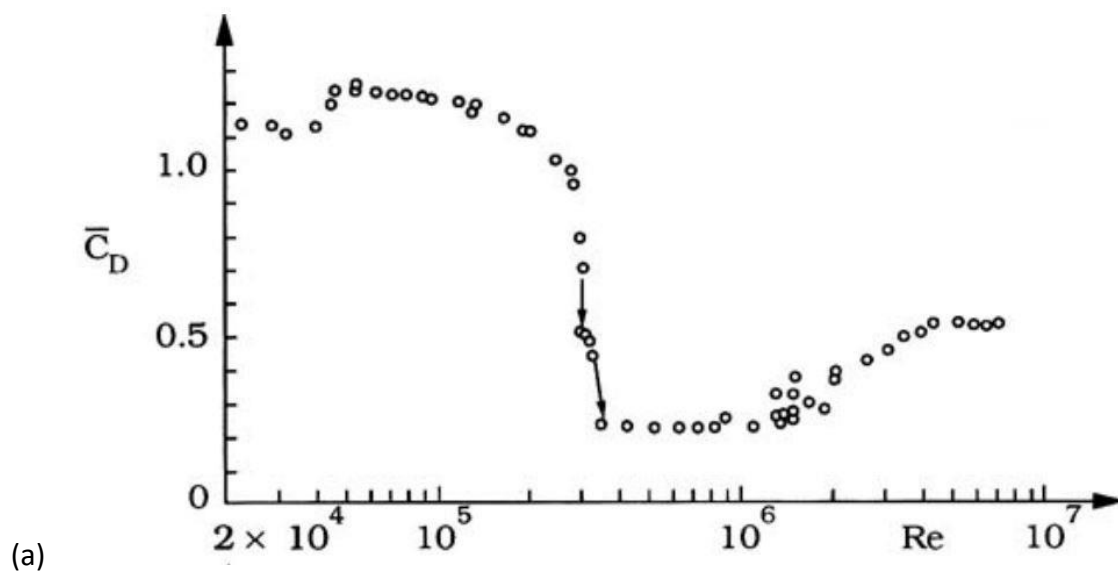
6.2 Suggestions for the future work

A. Free vibration in both in-line and transverse directions

In this thesis, the transverse-only vibration of a cylinder in the lock-in regime has been investigated. However, in practice, most structures may be free to move in both the in-line and transverse directions. In such a case, there are two-direction amplitude and frequency variables as well as a phase angle between in-line and transverse motions. The method to predict the response of such free motion based on results from the corresponding forced motion remains to be investigated in the future study.

B. Free vibration from critical up to transcritical Reynolds numbers

In ocean engineering, Reynolds number is always very high, and it would be interesting to extend simulation work into the critical, supercritical and transcritical turbulent ranges. From the review paper given by [Sumer and Fredsoe \(1997\)](#), for a fixed circular cylinder, in the critical turbulent range where Re is from 3×10^5 to 3.5×10^5 , a non zero mean lift coefficient occurs due to the flow asymmetry, Strouhal number experiences a sudden jump from about 0.2 to a value of about 0.45, and the mean drag coefficient decreases abruptly from about 1.2 to a much lower value, about 0.25, which is called drag crisis, shown in Fig. 6-1. It seems that unexpected behaviour in VIV in this range may be found, when free vibration is investigated in this range. In addition, from critical to transcritical Reynolds numbers, the effect of three-dimensionality which has been ignored in this work should be considered. Correspondingly, the LBM model should be improved, or D2Q9 model used in the thesis should be replaced by D3Q19.



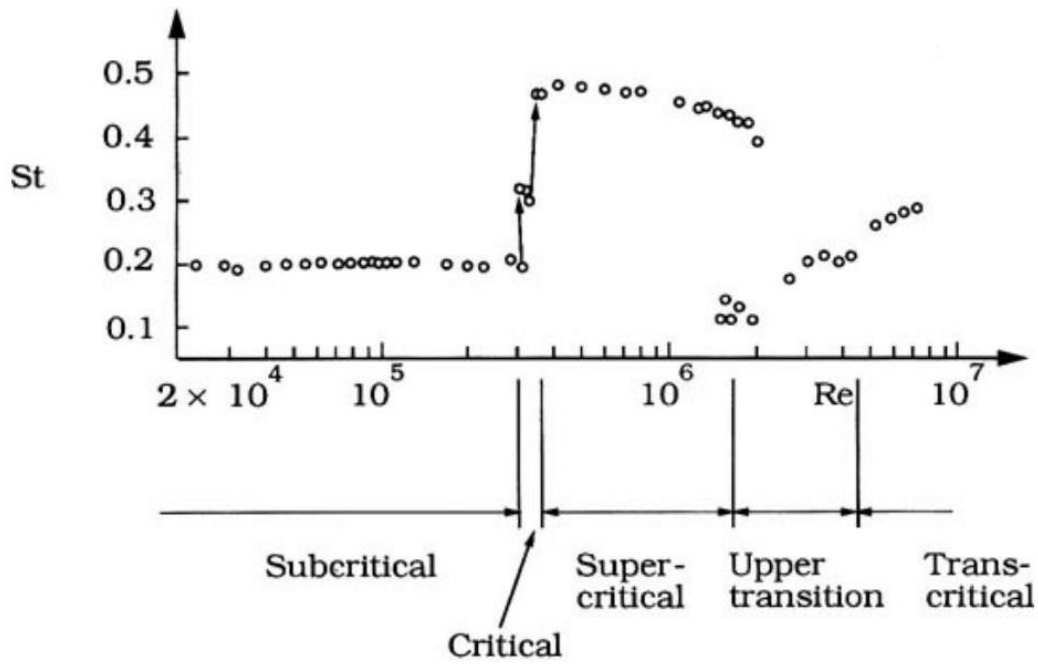


Fig. 6-1 Mean drag coefficient and Strouhal number against Reynolds number for a fixed circular cylinder from [Sumer and Fredsoe \(1997\)](#).

C. Vortex-induced vibration using machine learning

In recent years, Machine learning (ML) and its application have been rapidly advancing in various fields of science and technology. It has been also applied for the research of fluid mechanics due to a rapidly growth of data from experiments and numerical simulations ([Pollard et al., 2016](#); [Brunton et al., 2020](#)). For example, some preliminary studies have been conducted where ML was used in tasks such as reduced-order model, turbulence closure and flow control, and more details can be found in a review paper by [Brunton et al. \(2020\)](#). Specifically, in terms of VIV, [Raissi et al. \(2019\)](#) employed deep neural networks with the sinusoid activation function, one of the most well-known method in machine learning, to investigate transverse-only oscillation of a cylinder with $m^* = 2$, $b^* = 0.084$ and $k^* = 2.2020$ at $Re = 100$ in a two dimensions flow. Their research may demonstrate a potential paradigm shift in VIV research and provide possibilities of systematically investigating the essential characteristics of VIV as a complex function of many input parameters.

Acknowledgements

I would like to express my most sincere gratitude to my supervisor, Professor Guoxiong Wu. Through these years we have worked together, he provided invaluable guidance, support and encouragement. He always discussed research questions with me and gave inspiring comments and suggestions to help me finish my PhD study. Due to his guidance, one of my published papers published in *Physics of Fluids (PoF)* has been chosen as one of the featured papers, or one of the best *PoF* papers chosen by the editors.

I would also like to thank my family. Without them, I would not have gotten to where I am now. Their endless love, unconditional support and continuous encouragement help me overcome problems in my study and life.

Bibliography

T. Abe. Derivation of the lattice Boltzmann method by means of the discrete ordinate method for the Boltzmann equation. *Journal of Computational Physics*, 131:241-46, 1997.

H. T. Ahn and Y. Kallinderis. Strongly coupled flow/structure interactions with a geometrically conservative ale scheme on general hybrid meshes. *Journal of Computational Physics*, 219(2):671–696, 2006.

C. K. Aidun and J. R. Clausen. Lattice-Boltzmann method for complex flows. *Annual Review of Fluid Mechanics*, 42:439-72, 2010.

M. H. Akbari and S. J. Price. Numerical investigation of flow patterns for staggered cylinder pairs in cross-flow. *Journal of Fluids and Structures*, 20:533-554, 2005.

P. Anagnostopoulos and P. W. Bearman. Response characteristics of a vortex-excited cylinder at low Reynolds numbers. *Journal of Fluids and Structures*, 6:39-50, 1992.

P. W. Bearman. Vortex shedding from oscillating bluff bodies. *Annual Review of Fluid Mechanics*, 16:195-222, 1984.

P. W. Bearman. Circular cylinder wakes and vortex-induced vibrations. *Journal of Fluids and Structures*, 27:648-658, 2011.

P. W. Bearman and A. J. Wadcock. The interaction between a pair of circular cylinders normal to a stream. *Journal of Fluid Mechanics*, 61:499-511, 1973.

P. L. Bhatnagar, E. P. Gross and M. Krook. A model for collision processes in gases. I: small amplitude processes in charged and neutral one-component system. *Physical Review*, 94:511-525, 1954.

K. Y. Billah and R. H. Scanlan. Resonance, Tacoma Narrows bridge failure, and undergraduate physics textbooks. *American Journal of Physics*, 59:118, 1991.

R. D. Blevins. *Flow-induced Vibrations*. Van Nostrand Reinhold, New York, 1990.

I. Borazjani and F. Sotiropoulos. Vortex-induced vibrations of two cylinders in tandem arrangement in the proximity-wake interference region. *Journal of Fluid Mechanics*, 621:321–364, 2009.

S. L. Brunton, B. R. Noack and P. Koumoutsakos. Machine learning for fluid mechanics. *Annual Review of Fluid Mechanics*, 52:477-508, 2020.

J. Carberry, R. Govardhan, J. Sheridan, D. Rockwell and C. H. K. Williamson. Wake states and response branches of forced and freely oscillating cylinders. *European Journal of Mechanics B/Fluids*, 23:89-97, 2004.

J. Carberry, J. Sheridan and D. Rockwell. Controlled oscillations of a cylinder: forces and wake modes. *Journal of Fluid Mechanics*, 538:31-69, 2005.

M. Carini, F. Giannetti and F. Auteri. On the origin of the flip-flop instability of two side-by-side cylinder wakes. *Journal of Fluid Mechanics*, 742:552-576, 2014.

B. S. Carmo and J. R. Meneghini. Numerical investigation of the flow around two circular cylinders in tandem. *Journal of Fluids and Structures*, 22:979-988, 2006.

C. Cercignani. *The Boltzmann Equation and its applications*. Springer-Verlag, New York, 1988.

S. Chen. A large-eddy-based lattice Boltzmann model for turbulent flow simulation. *Applied Mathematics and Computation*, 215:591-598, 2009.

S. Chen and G. D. Doolen. Lattice Boltzmann method for fluid flows. *Annual Review of Fluid Mechanics*, 30:329-64, 1998.

H. Chen, S. Kandasamy, S. A. Orszag, R. Shock, S. Succi and V. Yakhot. Extended Boltzmann kinetic equation for turbulent flows. *Science*, 301:633–36, 2003.

Y. Dong, P. Sagaut and S. Marie. Inertial consistent subgrid model for large-eddy simulation based on the lattice Boltzmann method. *Physics of Fluids*, 20:035104, 2008.

C. C. Feng. The measurements of vortex-induced effects in flow past a stationary and oscillating circular and D-section cylinders. Master's thesis, the University of British Columbia, 1968.

Z. G. Feng and E. E. Michaelides. The immersed boundary-lattice Boltzmann method for solving fluid-particles interaction problems. *Journal of Computational Physics*, 195:602-628, 2004.

U. Frisch, D. d'Humieres and B. Hasslacher. Lattice gas hydrodynamics in two and three dimensions. *Complex Systems*, 1:649-707, 1987.

S. Garcia. The lid-driven square cavity flow: from stationary to time periodic and chaotic. *Communications in Computational Physics*, 2:900-932, 2007.

U. Ghia, K. N. Ghia and C. T. Shin. High-Re solutions for incompressible flow using the Navier-Stokes equations and a multigrid method. *Journal of Computational Physics*, 48:387-411, 1982.

R. Govardhan and C. H. K. Williamson. Modes of vortex formation and frequency response of a freely vibrating cylinder. *Journal of Fluid Mechanics*, 420:85-130, 2000.

R. Govardhan and C. H. K. Williamson. Defining the 'modified Griffin plot' in vortex-induced vibration: revealing the effect of Reynolds number using controlled damping. *Journal of Fluid Mechanics*, 561:147-180, 2006.

O. M. Griffin. Vortex-excited cross-flow vibrations of a single cylindrical tube. *ASME Journal of Pressure Vessel Technology*, 102:158-66, 1980.

S. Hou, J. Sterling, S. Chen and G. D. Doolen. A lattice Boltzmann subgrid model for high Reynolds number flows. *Fields Institute Communication*, 6:151-66, 1996.

S. Hou, Q. Zou, S. Chen, G. D. Doolen and A. C. Cogley. Simulation of cavity flow by the lattice Boltzmann method. *Journal of Computational Physics*, 118:329-347, 1995.

F. S. Hover, A. H. Techet and M. S. Triantafyllou. Forces on oscillating uniform and tapered cylinders in crossflow. *Journal of Fluid Mechanics*, 363:97-114, 1998.

J. Hu and Y. Zhou. Flow structure behind two staggered circular cylinders. Part 1. Downstream evolution and classification. *Journal of Fluid Mechanics*, 607:51-80, 2008a.

J. Hu and Y. Zhou. Flow structure behind two staggered circular cylinders. Part 2. Heat and momentum transport. *Journal of Fluid Mechanics*, 607:81-107, 2008b.

K. Huang. *Introduction to statistical physics*. Taylor & Francis Group, London and New York, 1963.

T. Igarashi. Characteristics of the flow around two circular cylinders arranged in tandem (1st report). *Bulletin of the JSME*, 24:323-331, 1981.

W. Jester and Y. Kallinderis. Numerical study of incompressible flow about fixed cylinder pairs. *Journal of Fluids and Structures*, 17:561-577, 2003.

H. Jiao and G. X. Wu. Analysis of fluctuating force acting on two cylinders in different arrangements through Lattice Boltzmann Method. *Journal of Fluids and Structures*, 82:101-120, 2018a.

H. Jiao and G. X. Wu. Free vibration predicted using forced oscillation in the lock-in region. *Physics of Fluids*, 30:113601, 2018b.

S. Kang. Characteristics of flow over two circular cylinders in a side-by-side arrangement at low Reynolds numbers. *Physics of Fluids*, 15:2486-2497, 2003.

A. Khalak and C. H. K. Williamson. Dynamics of a hydroelastic cylinder with very low mass and damping. *Journal of Fluids and Structures*, 10:455-472, 1996.

A. Khalak and C. H. K. Williamson. Fluid forces and dynamics of a hydroelastic structure with very low mass dan damping. *Journal of Fluids and Structures*, 11:973-982, 1997.

A. Khalak and C. H. K. Williamson. Motions, forces and mode transitions in vortex-induced vibrations at low mass-damping. *Journal of Fluids and Structures*, 13:813–51, 1999.

N. B. Khan, Z. Ibrahim, M. I. Khan, T. Hayat and M. F. Javed. VIV study of an elastically mounted cylinder having low mass-damping ratio using RANS model. *International Journal of Heat and Mass Transfer*, 121:309-314, 2018.

H. J. Kim and P. A. Durbin. Investigation of the flow between a pair of circular cylinders in the flopping regime. *Journal of Fluid Mechanics*, 196:431-448, 1988.

M. Kiya, M. Arie, H. Tamura and H. Mori. Vortex shedding from two circular cylinders in staggered arrangement. *ASME Journal of Fluids Engineering*, 102:166-173, 1980.

J. T. Klamo, A. Leonard and A. Roshko. On the maximum amplitude for a freely vibrating cylinder in cross-flow. *Journal of Fluids and Structures*, 21:429-434, 2005.

T. Kruger, H. Kusumaatmaja, A. Kuzmin, O. Shardt, G. Silva and E. M. Vigen. *The lattice Boltzmann method: Principles and Practice*. Springer, New York, 2017.

S. Kumar, Navrose and S. Mittal. Lock-in in forced vibration of a circular cylinder. *Physics of Fluids*, 28:113605, 2016.

J. S. Leonitini, B. E. Stewart, M. C. Thompson and K. Hourigan. Predicting vortex-induced vibration from driven oscillation results. *Applied Mathematical Modelling*, 30:1096-1102, 2006.

Y. Li, R. Shoch, R. Zhang and H. Chen. Numerical study of flow past an impulsively started cylinder by the lattice-Boltzmann method. *Journal of Fluid Mechanics*, 519:273-300, 2004.

L. S. Luo. Analytic solutions of linearized lattice Boltzmann equation for simple flows. *Journal of Statistical Physics*, 88:913-926, 1997.

J. C. Maxwell. On the dynamical theory of gases. *Philosophical Transactions of the Royal Society of London*, 157:49-88, 1867.

G. R. McNamara and G. Zanetti. Use of the Boltzmann equation to simulate lattice-gas automata. *Physical Review Letters*, 61:2332-35, 1988.

J. R. Meneghini, F. Saltara, C. L. R. Siqueira and J. A. Ferrari Jr. Numerical simulation of flow interference between two circular cylinders in tandem and side-by-side arrangements, *Journal of Fluids and Structures*, 15:327-350, 2001.

S. Mittal, V. Kumar and A. Raghuvanshi. Unsteady incompressible flows past two cylinders in tandem and staggered arrangements. *International Journal for Numerical Methods in Fluids*, 25:1315-1344, 1997.

T. L. Morse and C. H. K. Williamson. Prediction of vortex-induced vibration response by employing controlled motion. *Journal of Fluid Mechanics*, 634:5-39, 2009a.

T. L. Morse and C. H. K. Williamson. The effect of Reynolds number on the critical mass phenomenon in vortex-induced vibration. *Physics of Fluids*, 21:045105, 2009b.

D. J. Newman and G. E. Karniadakis. Simulations of flow past a freely vibrating cable. *Journal of Fluid Mechanics*, 344:95-136, 1997.

C. Norberg. Fluctuating lift on a circular cylinder: review and new measurements. *Journal of Fluids and Structures*, 17:57-96, 2003.

Y. Peng, C. Shu, Y. T. Chew, X. D. Niu and X. Y. Lu. Application of multi-block approach in the immersed boundary-lattice Boltzmann method for viscous fluid flows. *Journal of Computational Physics*, 218:460-478, 2006.

C. S. Peskin. Numerical analysis of blood flow in the heart. *Journal of Computational Physics*, 25:220-252, 1977.

C. S. Peskin. The immersed boundary method. *Acta Numerica*, 11:479-517, 2002.

R. Pigazzini, G. Contento, S. Martini, T. Puzzer, M. Morgut and A. Mola. VIV analysis of a single elastically-mounted 2D cylinder: parameter identification of a single-degree-of-freedom multi-frequency model. *Journal of Fluids and Structures*, 78:299-313, 2018.

A. Pollard, L. Castillo, L. Danaila and M. Glauser. *Whither turbulence and big data in the 21st century*. Springer, 2016.

T. K. Prasanth and S. Mittal. Vortex-induced vibrations of a circular cylinder at low Reynolds numbers. *Journal of Fluid Mechanics*, 594:463-491, 2008.

Y. H. Qian, D. d'Humieres and P. Lallemand. Lattice BGK models for Navier-Stokes equation. *Europhysics Letters*, 17:479-84, 1992.

Y. H. Qian and S. A. Orszag. Lattice BGK models for the Navier-Stokes equation: nonlinear deviation in compressible regimes. *Europhysics Letters*, 21:255-59, 1993.

M. Raissi, Z. Wang, M. S. Triantafyllou and G. E. Karniadakis. Deep learning of vortex-induced vibrations. *Journal of Fluid Mechanics*, 861: 119-137, 2019.

T. Sarpkaya. Hydrodynamic damping, flow-induced oscillations, and biharmonic response. *ASME Journal of Offshore Mechanics and Arctic Engineering*, 117:232-238, 1995.

D. Sheils, A. Leonard and A. Roshko. Flow-induced vibration of a circular cylinder at limiting structural parameters. *Journal of Fluids and Structures*, 15:3-21, 2001.

S. Singha, K. K. Nagarajan and K. P. Sinhamahapatra, Numerical study of two-dimensional flow around two side-by-side circular cylinders at low Reynolds numbers, *Physics of Fluids*, 28:053603, 2016.

R. A. Skop. On modelling vortex-excited oscillations. NRL Memorandum Report, 2927, 1974.

R. A. Skop and O. M. Griffin. A model for the vortex-excited resonant response of bluff cylinders. *Journal of Sound and Vibration*, 27(2):225-233, 1973.

R. A. Skop and O. M. Griffin. On a theory for the vortex-excited oscillations of flexible cylindrical structures. *Journal of Sound and Vibration*, 41(3):263-274, 1975.

A. Slaouti and P. K. Stansby. Flow around two circular cylinders by the random-vortex method. *Journal of Fluids and Structures*, 6(6):641-670, 1992.

J. Smagorinsky. General circulation experiments with the primitive equations: I. The basic experiments. *Monthly Weather Review*, 91:99-164, 1963.

T. Staubli. Calculation of the vibration of an elastically mounted cylinder using experimental data from forced oscillation. *Journal of Fluids Engineering*, 105/225, 1983.

B. M. Sumer and J. Fredsoe. *Hydrodynamics around Cylindrical Structures*. World Sci, Singapore, 1997.

D. Sumner. Two circular cylinders in cross-flow: A review. *Journal of Fluids and Structures*, 26:849-899, 2010.

D. Sumner, S. J. Price and M. P. Paidoussis. Flow-pattern identification for two staggered circular cylinders in cross-flow. *Journal of Fluid Mechanics*, 411:263-303, 2000.

D. Sumner, S. S. T. Wong, S. J. Price and M. P. Paidoussis. Fluid behaviour of side-by-side circular cylinders in steady cross-flow. *Journal of Fluids and Structures*, 13:309-338, 1999.

F. Tong, C. Liang and M. Zhao. Numerical simulations of steady flow past two cylinders in staggered arrangements. *Journal of Fluid Mechanics*, 765:114-149, 2015.

B. J. Vickery and R. D. Watkins. Flow-induced vibrations of cylindrical structures. In *Proceedings of the First Australian Conference on Hydraulics and Fluid Mechanics* (ed. R. Silvester), New York: Pergamon Press, 1964.

J. B. V. Wanderley and L. F. N. Soares. Vortex-induced vibration on a two-dimensional circular cylinder with low Reynolds number and low mass-damping parameter. *Ocean Engineering*, 97:156-164, 2015.

C. H. K. Williamson. Evolution of a single wake behind a pair of bluff bodies. *Journal of Fluid Mechanics*, 159:1-18, 1985.

C. H. K. Williamson. Vortex dynamics in the cylinder wake. *Annual Review of Fluid Mechanics*, 28:477-539, 1996.

C. H. K. Williamson and R. Govardhan. Vortex-induced Vibrations. *Annual Review of Fluid Mechanics*, 36:413-455, 2004.

D. A. Wolf-Gladrow. *Lattice-Gas Cellular Automata and Lattice Boltzmann Models: An Introduction*. Springer, New York, 2000.

G. X. Wu. A note on non-linear hydrodynamics force on a floating body. *Applied Ocean Research*, 22:315-316, 2000.

G. Xu and Y. Zhou. Strouhal numbers in the wake of two inline cylinders. *Experiments in Fluids*, 37:248-272, 2004.

D. Yu, R. Mei and W. Shyy. A multi-block lattice Boltzmann method for viscous fluid flows. *International Journal for Numerical Methods in Fluids*, 39:99-120, 2002.

M. M. Zdravkovich. Review of flow interference between two circular cylinders in various arrangements. *ASME Journal of Fluids Engineering*, 99:618-633, 1977.

M. M. Zdravkovich. The effects of interference between circular cylinders in cross flow. *Journal of Fluids and Structures*, 1:239-261, 1987.

M. M. Zdravkovich. *Flow Around Circular Cylinder, vol. 2: Applications*. Oxford University Press, Oxford, UK, 2003.

C. Y. Zhou, R. M.C. So and K. Lam. Vortex-induced vibrations of an elastic circular cylinder. *Journal of Fluids and Structures*, 13:165-189, 1999.

Y. Zhou, H. J. Zhang and M. W. Yiu. The turbulent wake of two side-by-side circular cylinders.
Journal of Fluid Mechanics, 458:303-332, 2002.